

POLITECNICO DI TORINO

**Corso di Laurea Magistrale
in Ingegneria Aerospaziale**

Tesi di Laurea Magistrale

**Full crash simulations material database
development including failure criteria for
coarse shell elements**



Relatore

Prof. Marco Gherlone

Ing. Alessandro Marangon

Candidato

Cesare Patuelli

Ottobre 2019

In collaboration with Italdesign-Giugiaro S.p.A.

Summary

List of Figures	III
List of Tables	VII
Acknowledgements	VIII
Introduction	1
1. Materials characterization	3
1.1 The role of different steels in vehicles	4
1.1.1 Soft steels	6
1.1.2 Low-alloy and micro-alloyed steels (LA or HSLA)	6
1.1.3 High strength Interstitial Free steels (IF)	6
1.1.4 Bake-hardening steels (BH)	6
1.1.5 Dual-phase steels (DP)	7
1.1.6 TRIP steels	7
1.1.7 Martensitic steels (MS)	7
1.2 Premises on material characterization	8
1.3 Hardening laws	11
1.4 Strain Rate Sensitivity	14
1.5 Instability models	16
1.5.1 Forming Limit Diagram (FLD)	17
1.5.2 Hill-Stören-Rice Model	19
1.6 Ductile fracture criteria	20
1.6.1 Modified Mohr-Coulomb model	20
1.7 Explicit solutions	26

1.8	Materials calibration flow chart	29
2.	Calibration of steels	30
2.1	Hardening law calibration	30
2.2	Dynamic flow curve modelling.....	36
2.3	Tensile Test Simulations	41
2.4	Axial crash simulations	44
3.	Martensitic Steel Calibration	49
3.1	Hardening law	50
3.1.1	Tailored Crash Model	51
3.1.2	Model refinement.....	56
3.1.3	Enhanced Tailored Crash Model.....	61
3.2	Diffuse and Localized Necking laws.....	66
3.3	Modified Mohr-Coulomb for Martensitic Steels.....	69
3.3.1	Enhanced Hill-Stören-Rice model parameter	76
4.	Enhanced Tailored Crash Model Validation.....	80
4.1	Hat Test.....	80
4.2	Side Crash	85
4.3	Front Crash.....	89
5.	Conclusions.....	92
	References.....	94

List of Figures

Figure 1: Distribution of the most used steels in automotive with respect to Tensile Strength and Yield Strength [45].....	4
Figure 2: Position of different steels in a body in white [45]	5
Figure 3: Percentages of different class steels used in a body in white [45]	5
Figure 4: Dual Phase Steel (DP600) Engineering Stress-Strain plot with marked characteristic points.....	9
Figure 5: Dual Phase Steel (DP600) True Stress-Strain plot.....	10
Figure 6:Extrapolation results for quasistatic models (fit range between yield stress and Rm). [34]	12
Figure 7: Dual Phase Steel (DP600) hardening curves for different strain rates.....	14
Figure 8: Three-dimensional representation of strain rate curves.....	15
Figure 9:Necking occurring in a fine and a coarse mesh specimen.....	16
Figure 10: Forming Limit Diagram [43].....	17
Figure 11: Forming limit curves for a high and a low strain-hardening sheet [20]	19
Figure 12: Different resolution quality of strain and stress parameters: the stress parameters have good resolutions in the elastic region, and the strain parameters have good resolutions far in the plastic region [24]	21
Figure 13: Three types of coordinate system in the space of principal.....	24
Figure 14: Quasistatic Models: DP600 Results	31
Figure 15: DP600 CSV Hardening Curve.....	33

Figure 16: Scaled hardening curve for DP600 according maximum, minimum and medium tolerance	35
Figure 17: Low, intermediate and high strain rate sensitivity at increasing true plastic strain [34] ..	37
Figure 18:Low strain rate log. strain rate sensitivity m vs. quasistatic $Rp0,2$ -Power fitting of experimental data ($[10 - 3 \cdot 20s - 1]$, $\epsilon = 0,002/0,05/0,10$; 296K) [34]	38
Figure 19:Intermediate strain rate log. strain rate sensitivity m vs. quasistatic $Rp0,2$ -Power fitting of experimental data ($[10 - 3 \cdot 20s - 1]$, $\epsilon=0,002/0,05/0,10$; 296K) [34]	39
Figure 20: Strain Rate Curves, comparison between DP600 strain rate curves from Autosteel database and Larour’s model results	40
Figure 21: Specimen Dimension according to ASTM E8/E8M	41
Figure 22: Specimen mesh.....	42
Figure 23: Localized and diffuse necking captured during the simulation.....	43
Figure 24: Reduced thickness in the localized necking zone.....	43
Figure 25: Simulation results vs Tensile test data from Autosteel	44
Figure 26: Sheet metal crash box FEM model.....	45
Figure 27: Collapsed crash box, calibrated DP 600.....	46
Figure 28: Collapsed crash box, OEM DP600.....	47
Figure 29: Force-Z displacement plot	48
Figure 30:Schematic of a B-pillar with tailored properties shown with a USIBOR 1500P CCT diagram.....	50

Figure 31: (a) Voce material parameters plotted as a function of the Vickers hardness and (b) The measured (symbols) and TCM predicted (curves) flow stress curves for a variety of as-quenched Vickers hardness and strain rate values [35].....	53
Figure 32: Voce law parameters as a function of Vickers hardness	54
Figure 33: Plot of the hardening law for a fully martensitic boron steel calculated with CSV parameters (orange) and with TCM model parameters (blue).....	57
Figure 34: "A" as function of HV	62
Figure 35: "n" as function of HV	62
Figure 36: "Eps0" as function of HV	63
Figure 37: Combined Swift-Voce hardening model for HV 480, 400, 320, 200.....	65
Figure 38: ϵD and ϵL as function of HV	66
Figure 39: EpsD and EpsL position for different HV in the True Plastic Strain-True Stress plane ..	68
Figure 40: CCT for USIBOR® 1500-AS. Three quench conditions overlaid on the CCT correspond to the fully martensitic, intermediate forced air quench, and fully bainitic, denoted by magenta, purple, and blue. The critical cooling rate of 30 °C/s to obtain a fully martensitic microstructure is also shown. [39].....	71
Figure 41: mMC Ductile Failure for HV 232, HV 386, HV 485.....	75
Figure 42: mMC Parameters versus Vickers Hardness	76
Figure 43: c (eHSR) as function of HV	78
Figure 44: eHSR Instability and mMC Ductile Failure plot for HV 232, HV 386 and HV 458	79
Figure 45: Hat test configuration	81

Figure 46: Contact Force vs Time for HV190 OEM and eTCM steel.....	82
Figure 47: Contact Force vs Time for HV320 OEM and eTCM steel.....	82
Figure 48: Contact Force vs Time for HV400 OEM and eTCM steel.....	83
Figure 49: Contact Force vs Time for HV480 OEM and eTCM steel.....	83
Figure 50: Failure Reduced Risk contour for HV480 eTCM and OEM.....	84
Figure 51: Moving deformable barrier alignment with test vehicle [41].....	86
Figure 52: Static side intrusion after IIHS MDB Side Crash. eTCM vs OEM.....	87
Figure 53: Failures in Body in White after IIHS MDB Side Crash. eTCM vs OEM.....	88
Figure 54: Vehicle overlap with deformable barrier [42]	89
Figure 55: Static Intrusion after IIHS ODB Front Crash	90
Figure 56: Failures in Body in White after IIHS ODB Front Crash	91

List of Tables

Table 1: Quasistatic models	13
Table 2: Load states defined by α	18
Table 3: DP600 CSV Parameters	33
Table 4: Mechanical Properties of Dual Phase Steel DP600	34
Table 5: Parameters for hardening curves at maximum, minimum and medium tolerance	35
Table 6: The constant parameters for equations (3.2)-(3.6) [35]	52
Table 7: Constant parameters for equations (3.8) -(3.11)	55
Table 8: Plasticity model parameters for pure isotropic hardening [36]	56
Table 9: εD and εL computed for CSV ad TCM model	60
Table 10: Constant parameters for equations (3.22)-(3.25)	64
Table 11: Diffuse and localized necking plastic strain comparison	65
Table 12: εD and εL parameters for equations (3.27) -(3.30)	67
Table 13: Test results for HV 232 equivalent failure plastic strain versus averaged triaxiality	72
Table 14: Tests results for HV 386, equivalent failure plastic strain versus averaged triaxiality [39]	73
Table 15: Tests results for HV 485, equivalent failure plastic strain versus averaged triaxiality [37]	73
Table 16: mMC material parameters for HV 232, HV 386 and HV 485	74

Acknowledgements

I would like to thank my supervisor Prof. Marco Gherlone for giving me the opportunity to pursue my academic goal of developing my thesis in an automotive company. I wish to thank him not only for his continuous support during these months, but also for the passion he transmits while teaching, which has been a source of inspiration for my career and has served as a reminder of the reason behind my enthusiasm for engineering.

This work would not have been possible without the internship opportunity in Italdesign-Giugiaro SpA. In this company I found a very pleasant environment and a lot of helpful colleagues, who made me feel truly welcome during my time there. A special mention is reserved to my company supervisor Ing. Alessandro Marangon, one of the most experienced, passionate and brilliant engineers that I have ever met.

Last but not least I want to thank my friends and colleagues. They made my years in Turin so great. I wouldn't have made it without them.

I dedicate this thesis to my parents who always tried to give my sister Claudia, my brother Antonio and I all the chances to realize our dreams and ambitions. I always had all the support I needed from my family and I can't imagine a better one.

Introduction

Automotive manufacturer continues to develop more fuel-efficient vehicles, efforts taken to reduce vehicle mass are considerable, the use of lighter material is widely extended. However, is important to produce lighter weight vehicles without sacrificing structural integrity due to occupant safety requirements. Vehicle safety is a very important area in the automotive industry, one of the most important safety aspects of all is how car body performs and deforms during a crash event.

Full scale-controlled crashes are very expensive to execute, which is why the automotive industry relies heavily on computer simulations. One of the most important part of finite element simulations for a company operating in automotive sector is the material database. In order to have a reliable simulation a very detailed materials definition is needed. Accuracy and reliability of simulations are very important, but often another important requirement is time; it is well known that a detailed finite solid elements model simulation can replicate almost exactly a real situation, but computational time and costs are unsustainable. In automotive sector is widely diffused the use of shell elements for vehicle body simulations, the presence of mostly metal sheets justifies the choice, but the use of these elements introduces some approximations and material databases must include additional models for plastic deformations and fracture. Explicit solvers are mostly used for crash test simulation because of their good performances in short duration events. Implicit numerical methods are unconditionally stable, but they couple the equations governing the physical problem. On the other hand, explicit numerical methods can decouple the equations, but their stability is conditional. The second class of numerical methods is particularly suited for crash events.

Automotive industry operates with a very wide range of materials, metals, polymers, glues and composites. Probably the most important concerning safety are metals, mainly steels, because they are responsible for the biggest absorption of energy during crashes. A detailed material database can be very expensive because it needs a very high number of tests on several specimens in order to identify all the mechanical properties for each material. However, in literature there is a great quantity of academic papers involving materials characterization. The results of this work can be used to create a material database with an analytical approach.

The purpose of the present work is to create a mathematical model for steel calibration. The first part presents an overview on material characterization with the definitions of physical quantities and theories used in the models. The second concern the calibration of several classes of steels which are the most used in automotive industry, dual phase steels, mild steels, interstitial free steels, bake hardening steels, high strength steels and transformation induced plasticity steels. Then the last part is dedicated to press hardened martensitic steels and to the development of a new model depending only on Vickers Hardness which is a common parameter to classify this kind of steel.

1. Materials characterization

There is a constant quest for reliable experimental data concerning materials properties to produce accurate structural analysis and crash simulations. Usually to obtain these data, a large number of tests on several specimens are requested, for this reason an experimental characterization can be too expensive. Anyway, some materials, steels for instance, are well known and in literature there is large quantity of data and models that can be used to build a material database avoiding the costs of a measurement campaign.

Material database for full crash simulations must include basic properties of materials like Young modulus, Poisson modulus and density. Strain hardening curve of the material is an important attribute, it contains information related to the plastic region of the deformation. Software used for crash simulations need fracture models to take in account eventual failure of the material, these models are often mesh dependent and vary in case of shell or solid elements discretization.

All the theoretical notions useful for material characterization are briefly discussed in this chapter. After an overview on steels used in automotive industry, each section is dedicated to a physical characteristic of the material that must be modeled in order to build the material card for the solver. The sequence of the sections wants to ideally replicate the chronological order of the steps taken to build the material characterization models.

1.1 The role of different steels in vehicles

According to the International Organization of Motor Vehicle Manufacturers [1], 95.9 million vehicles were produced in 2018, a 1,1% decrease compared to 2017. On average, 900 kg of steel is used per vehicle and is distributed as follows: 34% is used in body structures, 23% is in the drive train, 12% in the suspension and the remainder is found in steering, braking system, tyres and fuel tank. Body structures have a critical importance in crash events, different types of steels are used to match requirements of weight and safety, an example of distribution of steels in a body structure is shown in Fig.1,2 and 3.

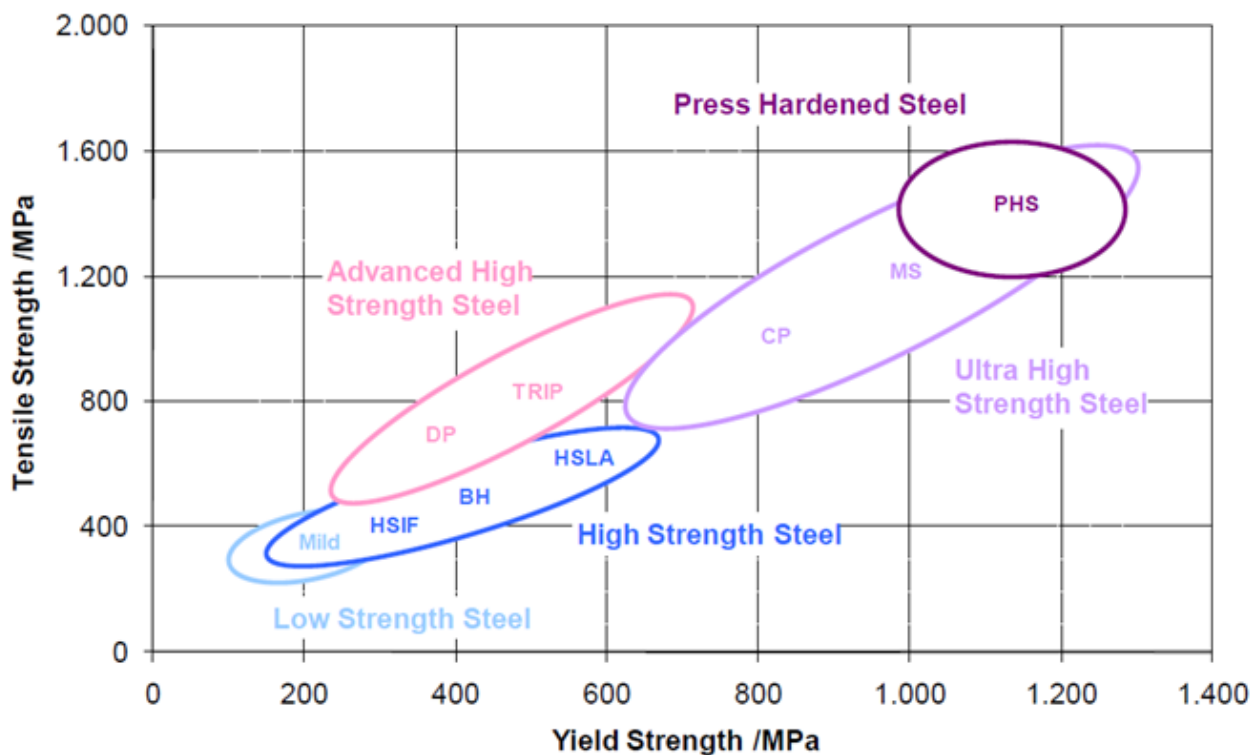


Figure 1: Distribution of the most used steels in automotive with respect to Tensile Strength and Yield Strength [45]

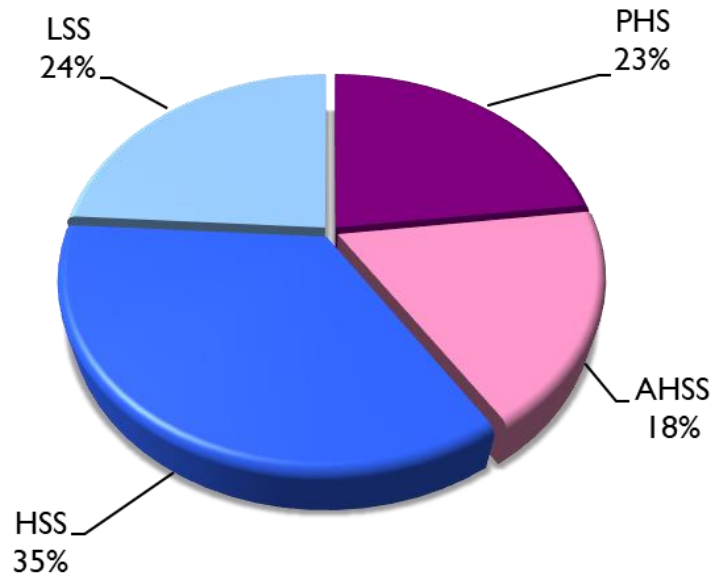


Figure 3: Percentages of different class steels used in a body in white [45]

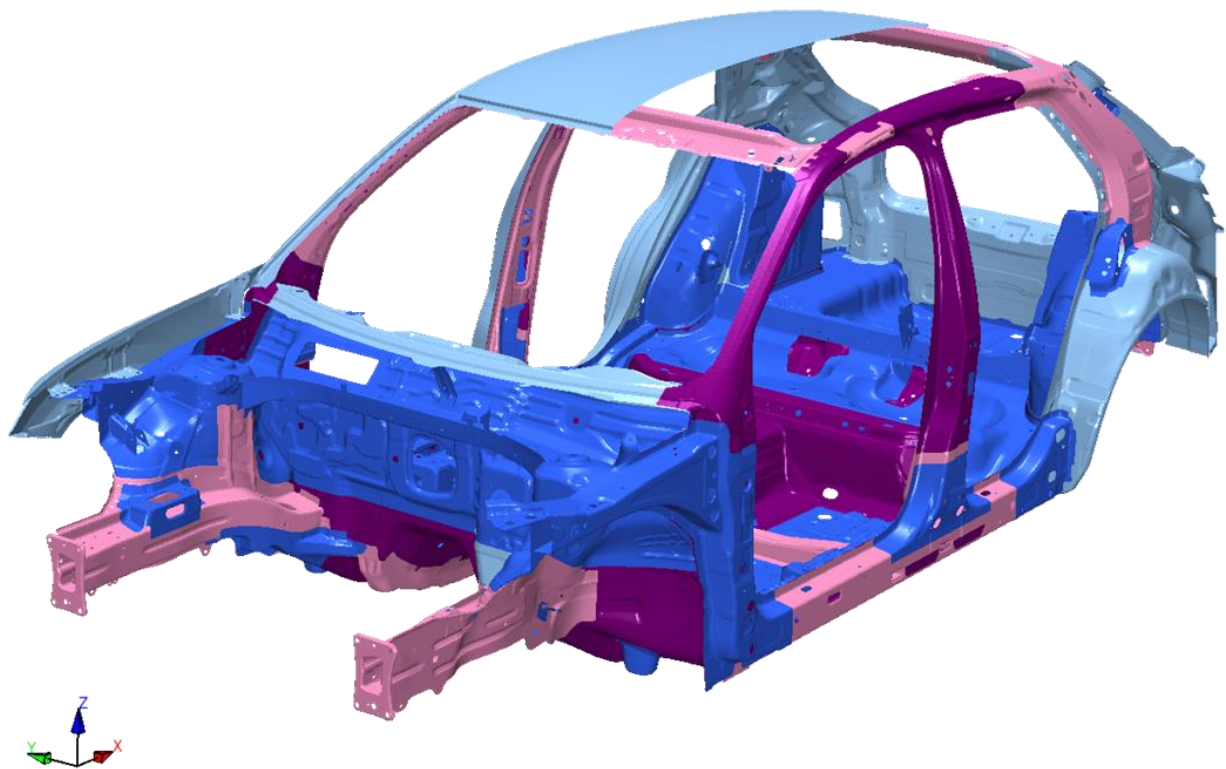


Figure 2: Position of different steels in a body in white [45]

1.1.1 Soft steels

Because of their low yield point and high elongation at break, soft steels for deep drawing are especially suited for producing complex components. Soft Interstitial-Free Steels (IF) have even a better formability and extremely low carbon and nitrogen content and are stabilized by the addition of titanium and niobium.

1.1.2 Low-alloy and micro-alloyed steels (LA or HSLA)

This class of steels have a high strength due to alloying with niobium, titanium and vanadium. Alternatively, carbon manganese systems can be used in combination with grain refinement.

1.1.3 High strength Interstitial Free steels (IF)

Like soft IF steels, high strength IF steels have extremely low carbon contents and are stabilized by titanium and niobium. The higher strength is reached with solid solution hardening by adding manganese, phosphorus, and/or silicon. Very good formability is achieved due to the greater hardness, the lack of a pronounced yield point and high elongation at break.

1.1.4 Bake-hardening steels (BH)

The strength is achieved with solid solution hardening by adding manganese, phosphorus, and silicon. In bake-hardening steels, carbon dissolved in the lattice leads to a defined increase in the yield point when heat treatments are performed. The buckling strength is thereby improved for skin parts. Because the change in the mechanical properties (yield point, elongation at break, tensile strain hardening exponent) occurs even at room temperature, albeit very slowly, the storage life of these steel grades is limited.

1.1.5 Dual-phase steels (DP)

The microstructure of dual-phase steels consists of a ferritic matrix, in which islands of a predominantly martensitic second phase are embedded. With a high tensile strength, dual-phase steels have a low yield point ratio (R_e/R_m) and a high cold work hardening rate. Therefore, they are especially suited for stretch forming processes.

1.1.6 TRIP steels

TRIP (Transformation induced plasticity) or residual-austenite steels have a fine-grained ferritic-bainitic matrix structure, in which residual austenite is embedded. In addition, small fractions of martensite can be present. During deformation, the residual austenite is transformed into martensite and thus causes a high cold work hardening rate. As a result, high tensile strength is achieved together with high elongation before reduction. In conjunction with the bake-hardening effect, high component strength can be achieved. TRIP steels are suitable for stretch forming as well as for deep drawing. However, higher pressing and sheet holder forces are required during forming, and a strong springback must be taken into account.

1.1.7 Martensitic steels (MS)

Martensitic steels have a largely martensitic microstructure with small fractions of ferrite and/or bainite and thus very high strength. Suitability for deep drawing is limited; these steel grades are suitable predominantly for forming methods involving bending, such as roll forming.

1.2 Premises on material characterization

In this section basic relationship and definition of the principal physical quantities involved in material characterization will be discussed. The tensile test is the principal experimental test to determine material properties such as Young Modulus, Poisson ratio, ultimate tensile strength, yield strength, shear modulus and so on. The test proceeds with a specimen fixed with two jaws at the opposite edges, then one of them start to move slowly applying a tensile load to the specimen up to fracture. The result of the tensile test is a chart of the engineering stress versus engineering strain. Engineering stress and strain are defined by:

$$\sigma = \frac{F}{A_0} \quad (1.1)$$

$$\varepsilon = \frac{\Delta l}{L_0} \quad (1.2)$$

Where F is the applied load, A_0 is the initial section of the specimen, Δl is the longitudinal deformation and L_0 is the initial length of the specimen.

True stress and true strain represent the effective stress and strain applied to the specimen, the engineering quantities are normalized with the initial area and the initial length of the specimen. Engineering quantities do not consider the deformations caused by the load, but they can be handily acquired during a test. Engineering and true quantities are related by the following equations:

$$\sigma_{true} = \sigma_{eng}(1 + \varepsilon_{eng}) \quad (1.3)$$

$$\varepsilon_{true} = \ln(1 + \varepsilon_{eng}) \quad (1.4)$$

In Fig.4 and 5, one can appreciate the different shape of the stress-strain plot obtained using engineering and true quantities.

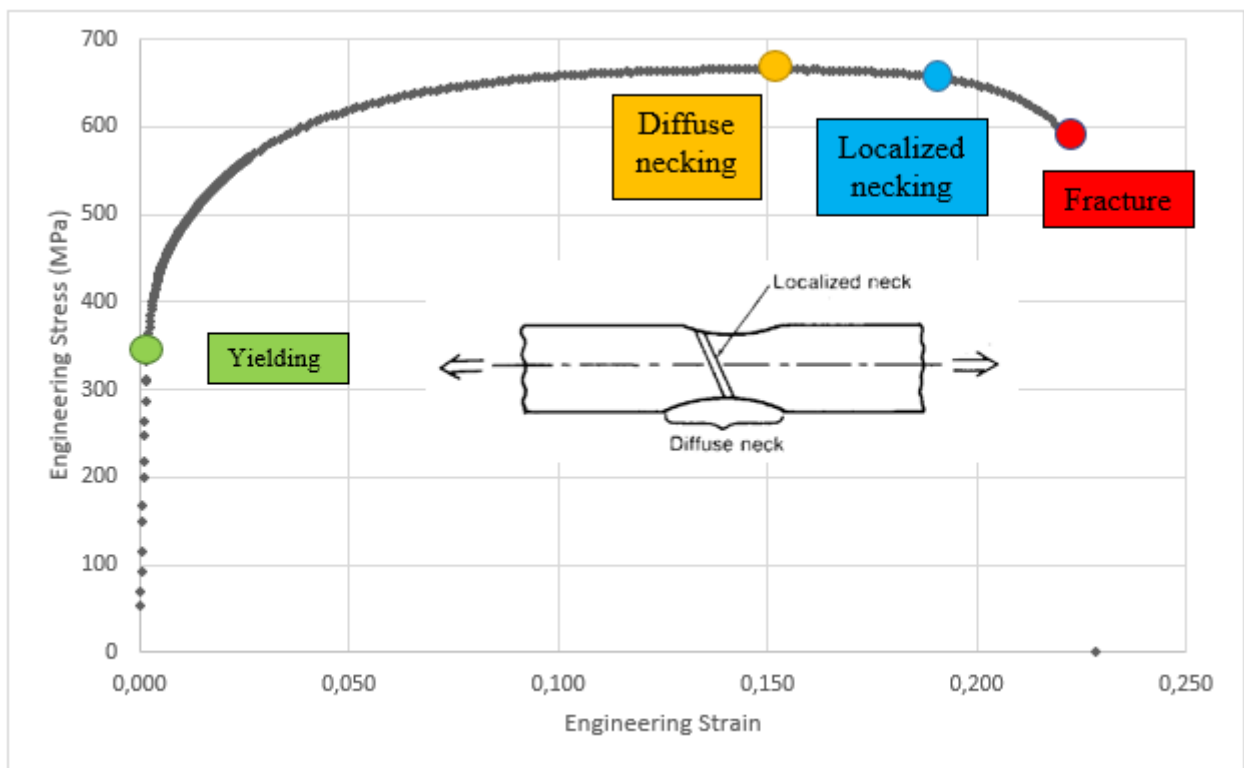


Figure 4: Dual Phase Steel (DP600) Engineering Stress-Strain plot with marked characteristic points

Often can be useful to consider only the plastic component of the deformation using the effective plastic strain or true plastic strain defined as:

$$\varepsilon_{eff}^p = \varepsilon_{true} - \varepsilon_{0,2\%} \quad (1.5)$$

In Fig.4 some characteristic points are highlighted. The first one is the yielding point, for steels yielding conventionally occurs when $\varepsilon = 0,2\%$. After the yielding point the stress is no longer proportional to the strain and the strain hardening begins, at this stage the material increases his hardness due to the cold deformation. The elastic response is fully described by the Young Modulus and the Poisson ratio for what concern the solver. The strain hardening stage can be read by the software as a sequence of points on a true stress-effective plastic strain chart, these points are often the result of an analytical model fitted with experimental data, the hardening law. As soon as the peak load is reached, the section starts to reduce its dimension along the width of the specimen, this stage is called diffuse necking. Then the reduction of the resistant area proceeds up to another stage called

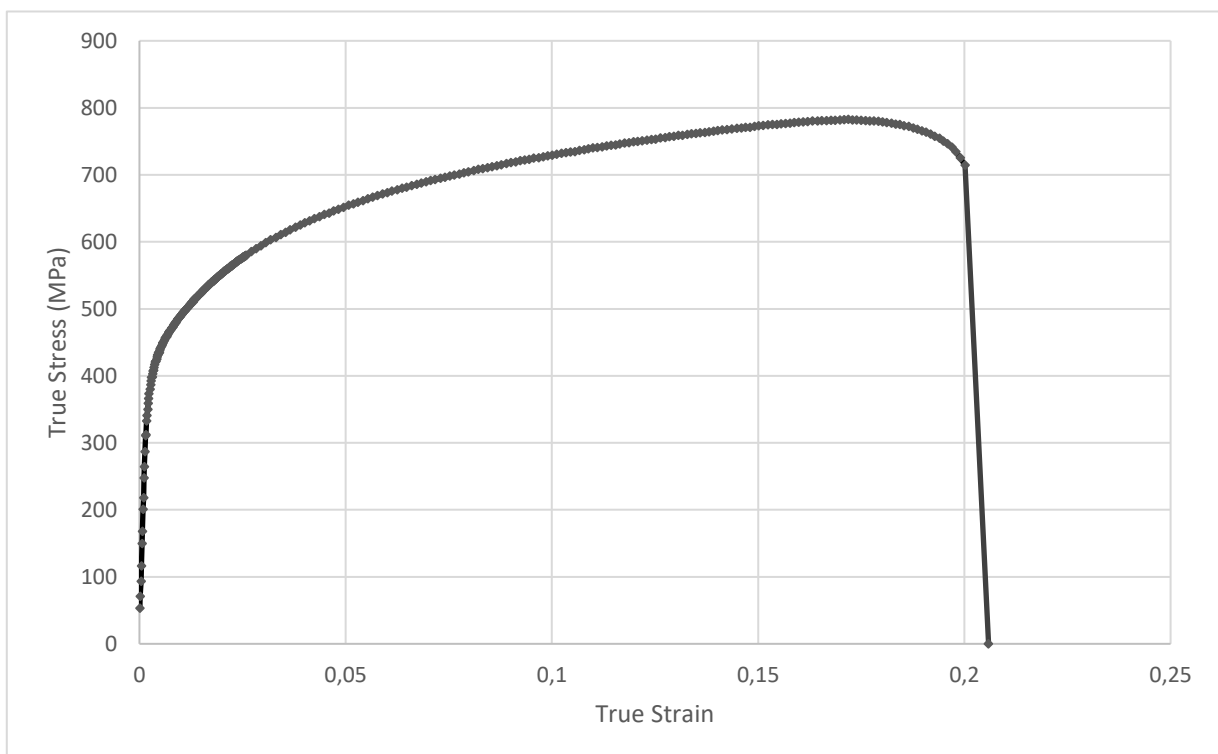


Figure 5: Dual Phase Steel (DP600) True Stress-Strain plot

localized necking. At this stage the deformation take place only in a small band with a degree of 55° with respect to the load direction (Fig.4). During localized necking the deformation develop along the thickness of the specimen. The final stage is the fracture with the separation of the two parts of the specimen.

1.3 Hardening laws

The hardening law is an analytical expression used to fit the plastic region of an experimental true stress - true strain curve; these curves can be very different according to the material. A large number of different hardening laws exist in the literature. While most of them fit well with experimental flow curves up to necking, the extrapolation for large strains can differ quite sensibly depending on the model considered. Several models, summarized in Table 1, can be tested in order to find the best correlation between the analytical model and empirical tests. Most of the parameters used in these models are purely mathematical, but others can be related to materials properties such as yield stress and necking strain. A strategy could be to include all the parameters in the optimization cycle and find the set for the best fit of the curve, a different approach is to consider physical parameters fixed and out of the optimization. Another option is to use material properties as a starting point for the related parameters and then include them in the optimization cycle to find the best set for fitting.

El-Magd and generalised Voce models deliver the highest linear work hardening rate at high strains. The Voce and Hockett/Sherby models give the lowest flow stress at high strains. The other models deliver intermediate flow stress levels, with a variable fitting accuracy. Fig. 6 shows the large

scatter that can be obtained with different models, even for the same initial flow curve and the same fitting strain range. The fitting results depend strongly on the strain range chosen for the fitting, even for the same model chosen. Such discrepancies should be reduced, if the fit range is chosen by avoiding the beginning of the flow curve, for example between 0,10 true plastic strain and true uniform elongation. This scatter in the extrapolation results will be also transferred to the dynamic models. Dynamic models require the same models in order to describe the strain hardening behaviour of the reference quasistatic flow curve.

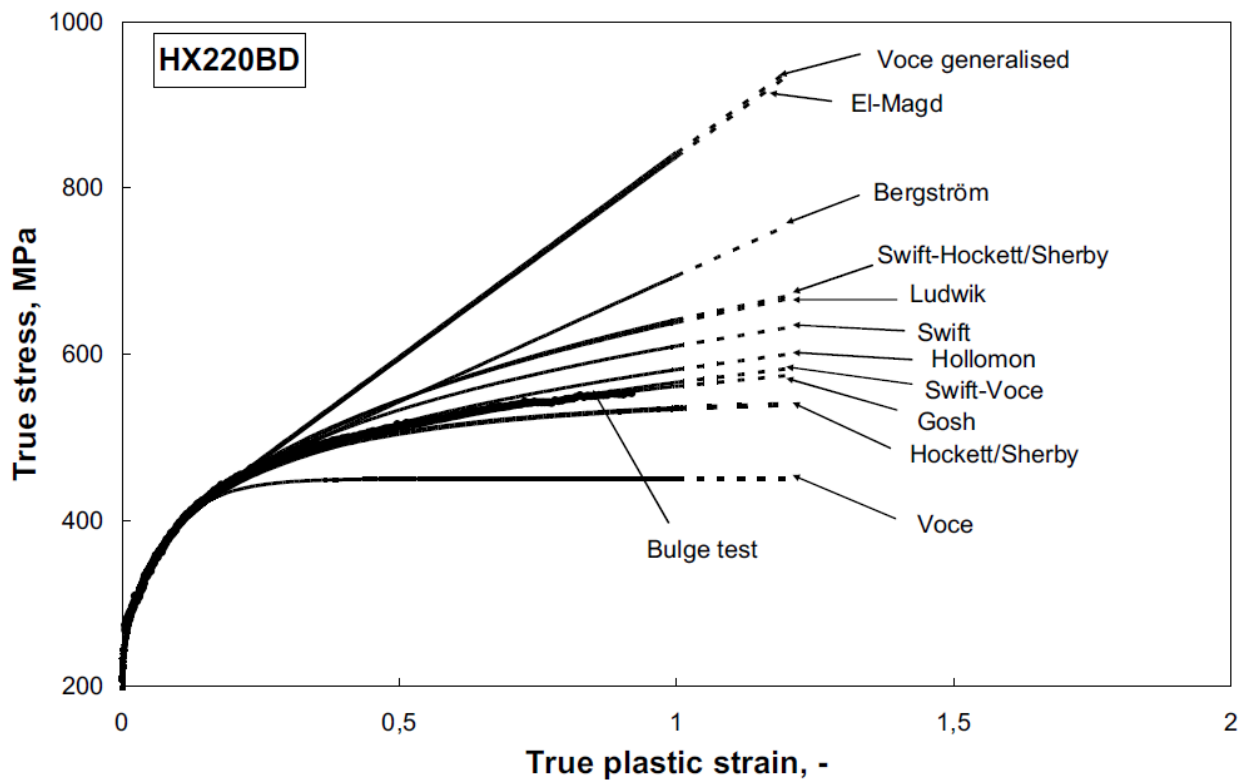


Figure 6: Extrapolation results for quasistatic models (fit range between yield stress and R_m). [34]

<i>Model</i>	<i>Equation</i>
<i>Hollomon [2]</i>	$\sigma(\varepsilon) = C_1 \cdot \varepsilon^{C_2}$ (1.6)
<i>Ludwik [3]</i>	$\sigma(\varepsilon) = C_1 + C_2 \cdot \varepsilon^{C_3}$ (1.7)
<i>Swift [4]</i>	$\sigma(\varepsilon) = C_1 \cdot (C_2 + \varepsilon)^{C_3}$ (1.8)
<i>Voce [5]</i>	$\sigma(\varepsilon) = C_1 + C_2 \cdot [1 - EXP(-C_3 \cdot \varepsilon)]$ (1.9)
<i>Hockett/Sherby [6]</i>	$\sigma(\varepsilon) = C_2 - (C_2 - C_1) \cdot EXP(-C_3 \cdot \varepsilon^{C_4})$ (1.10)
<i>Gosh [7]</i>	$\sigma(\varepsilon) = C_1 + C_2 \cdot (C_3 + \varepsilon)^{C_4}$ (1.11)
<i>Swift-Voce [8]</i>	$\sigma(\varepsilon) = C_1 \cdot \sigma_{Swift}(\varepsilon) + (1 - C_1) \cdot \sigma_{Voce}(\varepsilon)$ (1.12)
<i>Swift-Hockett/Sherby [9]</i>	$\sigma(\varepsilon) = C_1 \cdot (C_2 + \varepsilon)^{C_3} + C_4 \cdot EXP(-C_5 \cdot \varepsilon^{C_6})$ (1.13)
<i>El-Magd [10]</i>	$\sigma(\varepsilon) = C_1 + C_2 \cdot \varepsilon + C_3 \cdot [1 - EXP(-C_4 \cdot \varepsilon)]$ (1.14)
<i>Voce generalised [11]</i>	$\sigma(\varepsilon) = C_1 + C_2 \cdot [1 - EXP(-C_3 \cdot \varepsilon)] + C_4 \cdot \varepsilon$ (1.15)

Table 1: Quasistatic models

1.4 Strain Rate Sensitivity

Another important property of the material is the strain rate sensitivity, it represents the response of the material to different deformation velocities. This is crucial for crash simulations because usually deformations are very fast. Strain rate is defined by:

$$\dot{\varepsilon}(t) = \frac{d\varepsilon}{dt} = \frac{1}{L_0} \frac{dL}{dt}(t) \quad (1.16)$$

Since ε is a non-dimensional quantity, $\dot{\varepsilon}$ is measured with $[s^{-1}]$. Usually only a small number of strain rate curve are required for the description of the material. The interpolation is demanded to the solver, which build a surface between the assigned strain rate flow curves (Fig. 8);

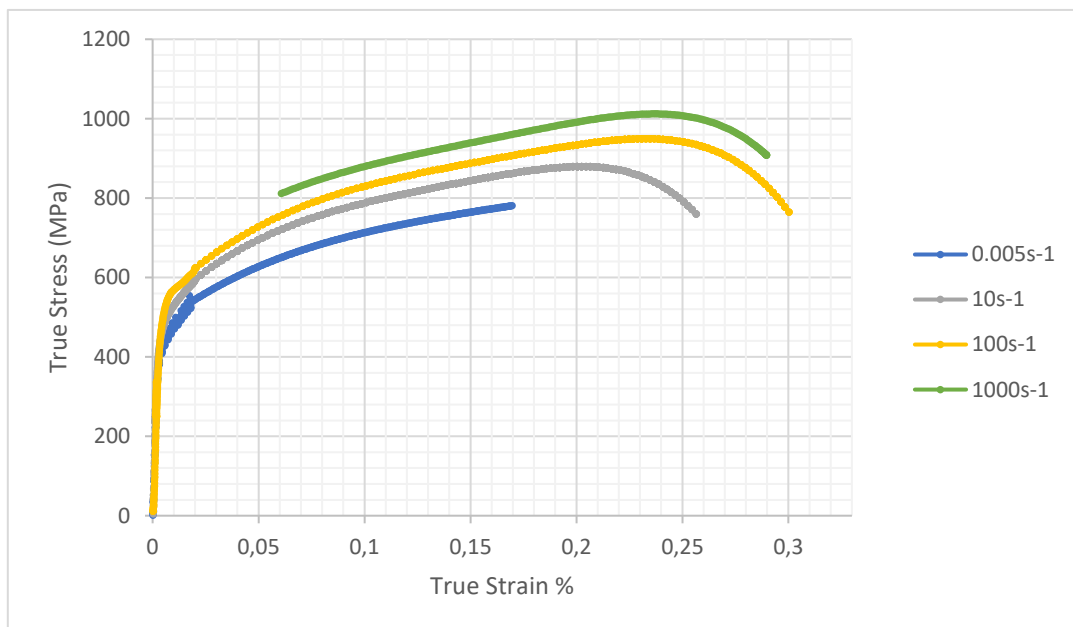


Figure 7: Dual Phase Steel (DP600) hardening curves for different strain rates

The strain rate sensitivity describes the dynamic material behaviour and is therefore an important mechanical property to be determined ([12], [13]). The strain rate sensitivity is defined by its relation to the plastic flow curve and for this reason is based on true stress values and not on engineering stress values. For the same reason, the tensile strength cannot be used as such, since this is an engineering stress value. Only the yield strength $R_{p0,2}$ can be used directly, since it corresponds approximately to the flow stress value $\sigma_{\text{true},0,2\%}$. The strain rate sensitivity is calculated in most publications based on the strain rate dependency flow curves. The logarithmic strain rate sensitivity m is originally defined from the extended Hollomon equation ([14], [15], [16], [17], [18]):

$$\sigma = k \cdot \varepsilon^n \cdot \dot{\varepsilon}^m \quad (1.17)$$

One can also replace the Hollomon equations $\sigma = k \cdot \varepsilon^n$ with another hardening law. The logarithmic strain rate sensitivity m can be determined with tensile tests at different velocities.

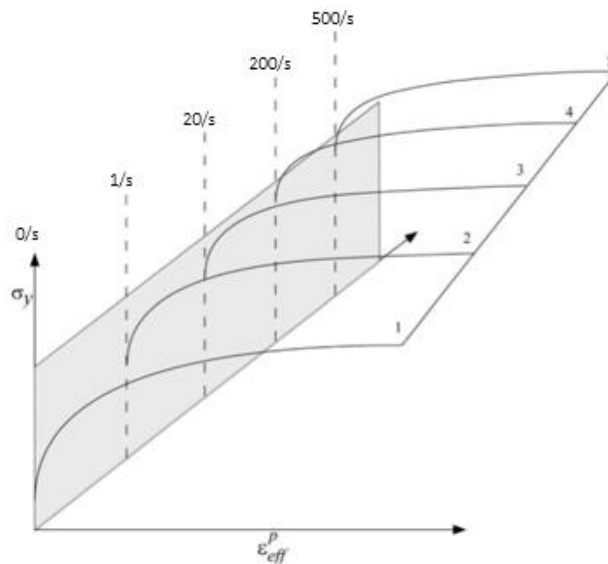


Figure 8: Three-dimensional representation of strain rate curves

1.5 Instability models

Ductile metal sheets deform uniformly up to the point of localized necking where the area reduction begins (maximum load), after this point the deformation enter in the post-necking phase, a slanted groove forms and stresses and strains become non-uniform. The localized necking and the resulting strain to fracture can't be predicted by a coarse mesh. The physical phenomenon is an order of magnitude smaller than the characteristic length of a coarse mesh element (Fig. 9), for this reason an instability criterion is needed to predict necking.

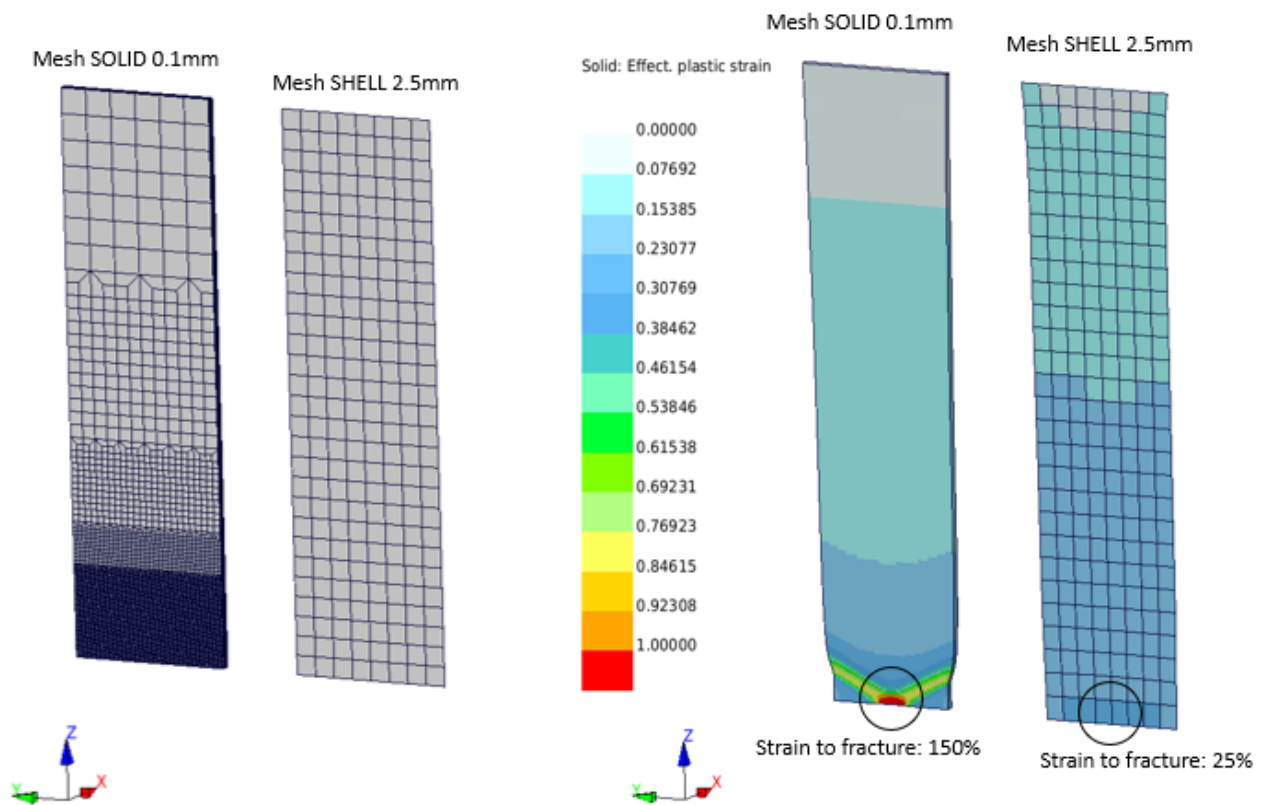


Figure 9: Necking occurring in a fine and a coarse mesh specimen

An instability model for crash simulation can be useful due to its mesh-independency and since localized necking occurs just before the fracture, this can represent a conservative “quasi-failure” criterion for sheet metals.

1.5.1 Forming Limit Diagram (FLD)

The FLD introduced by Keeler and Backofen [19] collect the principal strains (ϵ_1, ϵ_2) at the onset of localized necking for different loading condition of the diagram. The FLD is a valuable material property curve; it is used frequently as instability model and failure criterion in sheet metal forming.

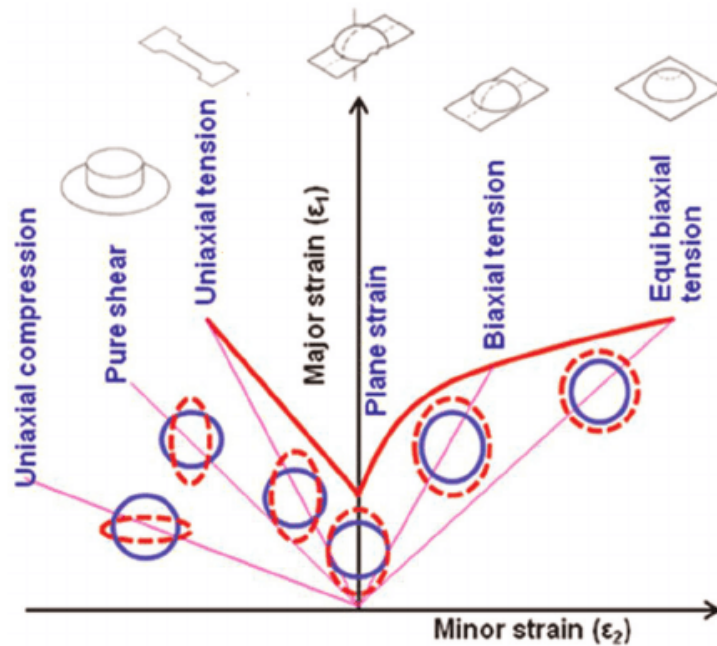


Figure 10: Forming Limit Diagram [43]

The forming limit curve intercepts the major strain axis at approximately the value of the strain-hardening index n . As n decreases, the height of the curve will also decrease [20], Fig. 11. Usually the different load states are defined with the principal in-plane plastic strain increment ratio:

$$\alpha = \frac{d\varepsilon_1}{d\varepsilon_2} \quad (1.18)$$

Each load state is defined by a value of α :

$\alpha = 1$	Equibiaxial Tension
$\alpha = 0$	Plain Strain
$\alpha = -1/2$	Uniaxial Tension
$\alpha = -1$	Pure Shear
$\alpha = -2$	Uniaxial Compression

Table 2: Load states defined by α

The forming limit diagram of a specific material can be determined experimentally, anyway several numerical models can be used to describe the FLD for a given material. In any case FLD can't predict the fracture that occur outside its domain, so this instability model cannot predict shear fracture and bending fracture for instance, these types of failures require ductile fracture criteria.

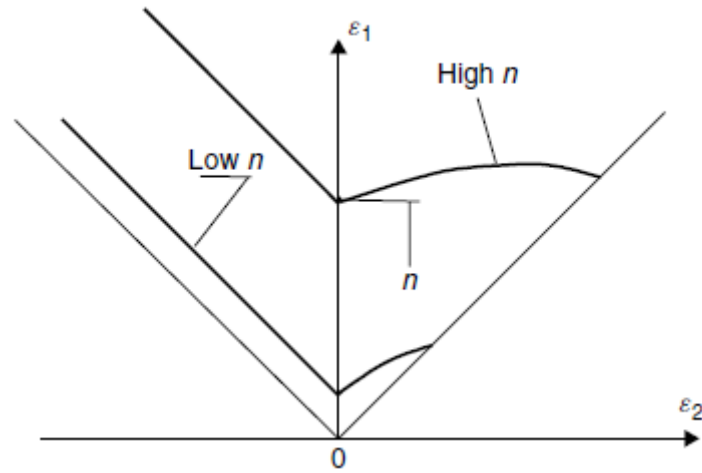


Figure 11: Forming limit curves for a high and a low strain-hardening sheet [20]

1.5.2 Hill-Stören-Rice Model

Hill-Stören-Rice model [21] can predict the forming limit diagram for a given material, it is a quite reliable and simple mono-parametric model that can be implemented in a solver as fracture criterion. The analytical expression of the model results in a ε_{1n} - α plot with ε_{1n} the major strain at necking.

$$\varepsilon_{1n} = \begin{cases} \frac{n}{(1+\alpha)}, & -1 < \alpha \leq 0 & (1.19) \\ \frac{3\alpha^2 + n(2+\alpha)^2}{2(2+\alpha)(1+\alpha+\alpha^2)}, & 0 < \alpha < 1 & (1.20) \end{cases}$$

The Hill-Stören-Rice Model can be used also as element elimination criterion through the parameter “n” which is equal to the equivalent plastic strain associated to a localized necking in plain strain condition.

1.6 Ductile fracture criteria

The forming limit diagram can't predict bending and shear fractures as discussed in the previous section. A ductile fracture criterion is needed to cover all the possible failure conditions. Fracture is the macroscopic result of deformation and failure phenomena that occur at the micro-structural level of the material. Micro-structural fracture models are beyond the possibility of any engineering applications. Currently most calculations proceed through phenomenological failure models instead. That means a macro scale point of view without considering microscopic factors, for example dislocation motion in atomic lattices are not modelled.

1.6.1 Modified Mohr-Coulomb model

The Mohr-Coulomb fracture criterion ([22], [23]) has a good resolution for materials that fail in the elastic range and/or under small strain plasticity, but is demonstrated that this criterion can be applied to ductile fracture of uncracked bodies [24]. This fracture model is based on the physical mechanism of nucleation, growth and coalescence of voids, it was determined that ductile fracture is mostly affected by the hydrostatic pressure. Accordingly, the equivalent strain to fracture, which is a measure of material ductility, was made dependent on the first invariant of the stress tensor. The mixed stress-strain formulation of a fracture criterion is justifiable because, well into the plastic range, the resolution of strains is much larger than stresses, as explained in Fig. 12.

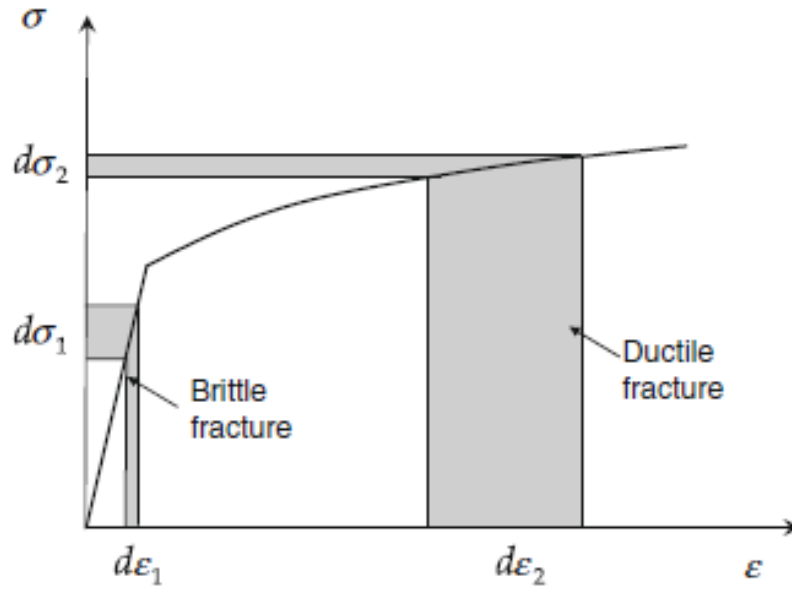


Figure 12: Different resolution quality of strain and stress parameters: the stress parameters have good resolutions in the elastic region, and the strain parameters have good resolutions far in the plastic region [24]

A large quantity of tests ([25], [26], [27], [28], [29]) proved that the material ductility depends on both stress triaxiality and Lode angle parameter, these two effects are actually captured by the M-C model.

The three invariants of a stress tensor $[\sigma]$ are defined respectively by:

$$p = -\sigma_m = -\frac{1}{3}tr([\sigma]) = -\frac{1}{3}(\sigma_1 + \sigma_2 + \sigma_3) \quad (1.21)$$

$$q = \bar{\sigma} = \sqrt{\frac{1}{2}[(\sigma_1 - \sigma_2)^2 + (\sigma_2 - \sigma_3)^2 + (\sigma_3 - \sigma_1)^2]} \quad (1.22)$$

$$r = \left[\frac{27}{2} \det([S]) \right]^{\frac{1}{3}} = \left[\frac{27}{2} (\sigma_1 - \sigma_m)(\sigma_2 - \sigma_m)(\sigma_3 - \sigma_m) \right]^{\frac{1}{3}} \quad (1.23)$$

Where $[S]$ is the deviatoric stress tensor defined by:

$$[S] = [\sigma] + p[I] \quad (1.24)$$

$[I]$ is the identity tensor and σ_1, σ_2 and σ_3 denote principal stresses. It is assumed that $\sigma_1 \geq \sigma_2 \geq \sigma_3$.

It is convenient to work with the dimensionless hydrostatic pressure η , defined by:

$$\eta = -\frac{p}{q} = \frac{\sigma_m}{\bar{\sigma}} \quad (1.25)$$

The parameter η is often referred to as the triaxiality parameter. The second important parameter is the Lode angle θ , which is related to the normalized third invariant ξ through:

$$\xi = \left(\frac{r}{q} \right)^3 = \cos(3\theta) \quad (1.26)$$

The range of the Lode angle is $0 \leq \theta \leq \pi/3$ so the range of ξ is $-1 \leq \xi \leq 1$. The geometrical representation of Lode angle is shown in Fig. 13. As shown in Fig. 13, one can use three types of coordinate systems to describe a stress state. The first is the Cartesian coordinate system $(\sigma_1, \sigma_2, \sigma_3)$,

the second is the cylindrical coordinate system $(\sigma_m, \bar{\sigma}, \theta)$, and the third is the spherical coordinate system $(\bar{\sigma}, \eta, \theta)$. The equivalent stress $\bar{\sigma}$ is related to the equivalent strain $\bar{\varepsilon}$ through the strain hardening function of a material. The coordinate φ is related to the stress triaxiality η by the following equation:

$$\eta = \frac{\sigma_m}{\bar{\sigma}} = \frac{\sqrt{2}}{3} \cotan(\varphi) \quad (1.27)$$

Furthermore, the Lode angle can be normalized:

$$\bar{\theta} = 1 - \frac{6\theta}{\pi} = 1 - \frac{2}{\pi} \arccos(\xi) \quad (1.28)$$

So that the range of $\bar{\theta}$ is $-1 \leq \bar{\theta} \leq 1$. The parameter $\bar{\theta}$ will be called Lode angle parameter hereinafter.

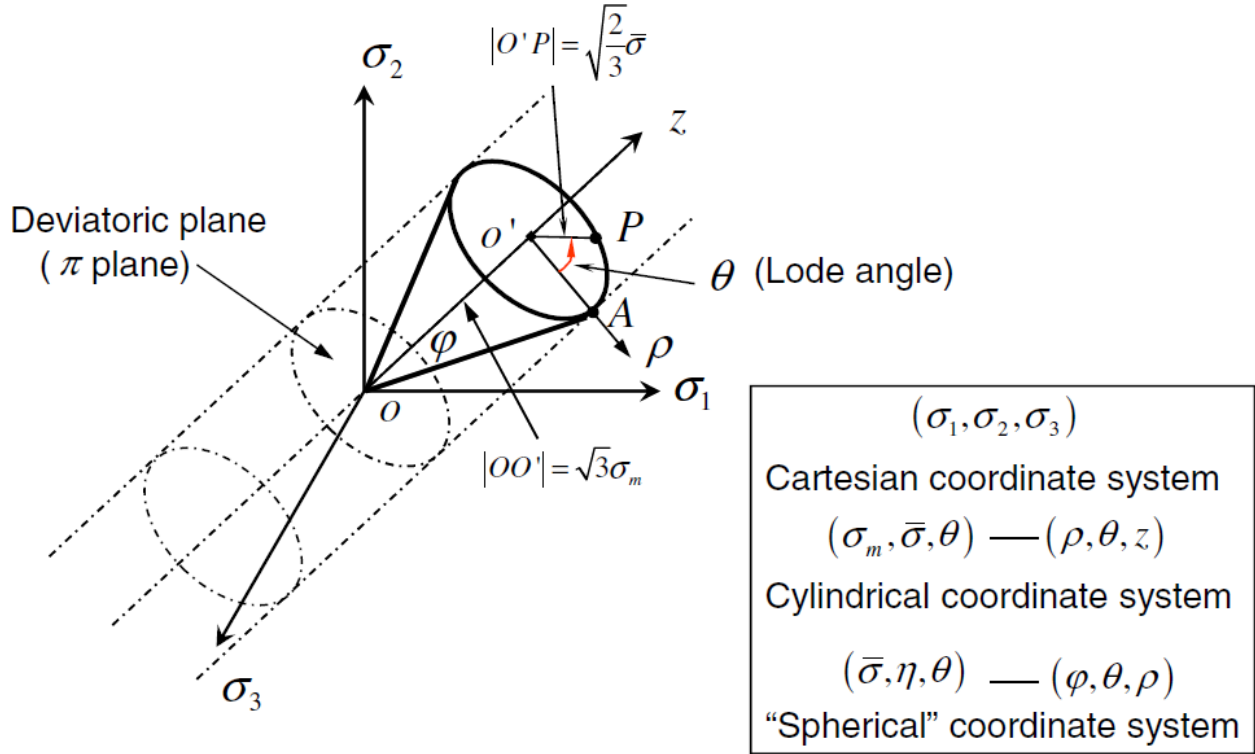


Figure 13: Three types of coordinate system in the space of principal

The direction of every stress vector (or loading condition) in the space of principal stresses can be characterized by the above defined set of parameters $(\eta, \bar{\theta})$. It is easy to show ([30], [31]) that $\bar{\theta} = 1$ corresponds to the axisymmetric tension, $\bar{\theta} = 0$ corresponds to the generalized shear loading condition and $\bar{\theta} = -1$ corresponds to the axisymmetric compression. Special attention is given to the plane stress state, because the plane stress condition, $\sigma_3 = 0$, uniquely relates the parameters η and $\bar{\theta}$ through:

$$\xi = \cos(3\theta) = \cos\left[\frac{\pi}{2}(1 - \bar{\theta})\right] = -\frac{27}{2} \eta \left(\eta^2 - \frac{1}{3}\right) \quad (1.29)$$

The classic Mohr-Coulomb fracture criterion says that fracture occurs when the combination of normal stress and shear stress reach a critical value according to:

$$(\tau + c_1\sigma_n)_f = c_2 \quad (1.30)$$

Where c_1, c_2 are material constants, τ is the shear stress and σ_n is the corresponding normal stress given by:

$$\tau = \sqrt{v_1^2 v_2^2 (\sigma_1 - \sigma_2)^2 + v_2^2 v_3^2 (\sigma_2 - \sigma_3)^2 + v_3^2 v_1^2 (\sigma_3 - \sigma_1)^2} \quad (1.31)$$

$$\sigma_n = v_1^2 \sigma_1 + v_2^2 \sigma_2 + v_3^2 \sigma_3 \quad (1.32)$$

Where $(\sigma_1, \sigma_2, \sigma_3)$ are the three principal stresses and (v_1, v_2, v_3) are the components of the unit vector normal to an arbitrary cutting plane.

The M-C criterion can be shifted from the mixed strain-stress plane to the $\eta, \bar{\theta}$ plane generating the modified M-C criterion:

$$\bar{\varepsilon}_f(\eta, \bar{\theta}) = \left\{ \frac{k}{c_2} \left[c_3 + (c_4 - c_3) \frac{\sqrt{3}}{2 - \sqrt{3}} \left(\sec\left(\frac{\pi}{6} \bar{\theta}\right) - 1 \right) \right] \left[\sqrt{\frac{1 + c_1^2}{3}} \cos\left(\frac{\pi}{6} \bar{\theta}\right) + c_1 \left(\eta + \frac{1}{3} \sin\left(\frac{\pi}{6} \bar{\theta}\right) \right) \right] \right\}^{-\frac{1}{n}} \quad (1.33)$$

Where k, n, c_1, c_2, c_3 and c_4 are material parameter. k and n are related to the hardening law of the material and can be calibrated from curve fitting of the stress-strain curve using power function, while c_1, c_2, c_3 and c_4 need to be determined from material tests carried up to fracture.

1.7 Explicit solutions

Numerical simulations have taken up a substantial part of the increased workload of crashworthiness engineers. Simulation is a valuable instrument during the design process for quick elimination from prototyping those designs which have a high probability of not satisfying the testing criteria. The increasing use of numerical simulation as support for a design team requires the rapid development of full vehicle FE models in the early stages of a design. Numerical simulation is also used for the diagnosis of the cause of a problem that can occur during a safety-related test. The extensive use of numerical simulation consented to introduce increasingly safer cars in less time without a corresponding increase in test facilities.

Ground vehicles are one of the most challenging nonlinear problems in structural mechanics. Vehicles structures are manufactured from many shell parts welded and fastened with various

techniques, and the body-in-white may contain steel of various strength grades, aluminium and composite materials.

Simulations proceed solving numerically a set of non-linear partial differential equations of motions in the space-time domain. The solution requires appropriate initial and boundary conditions. Solution first discretizes the equations in space by formulating the problem in a weak variational form and assuming an admissible displacement field, then the system of equations is solved by discretization in the time domain. Techniques to solve equations are labelled implicit if the selected integration parameters render the equation coupled, in this case the solution is unconditionally stable. If the integration parameters are selected to decouple the equations, then the solution is explicit and it is conditionally stable.

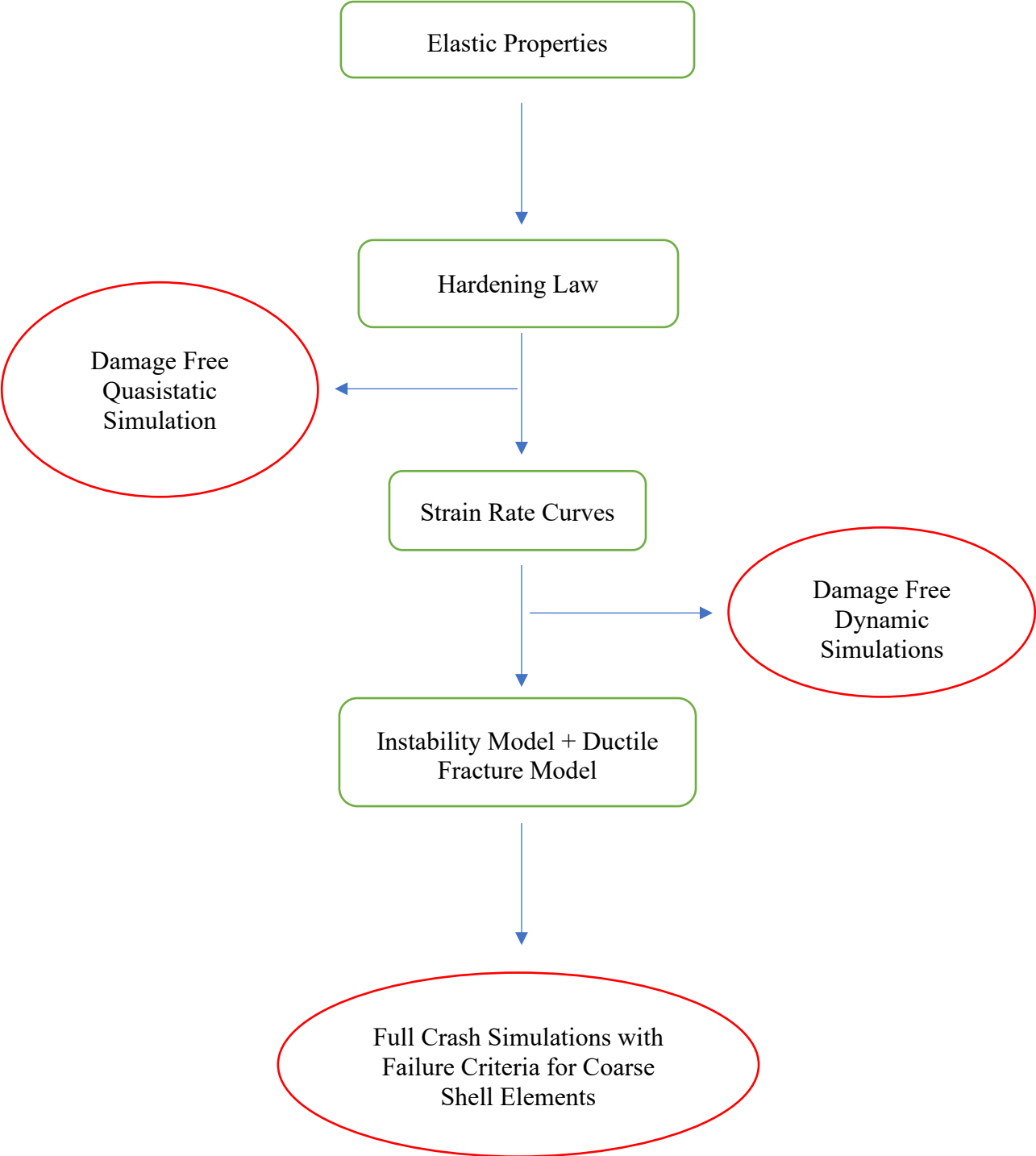
The explicit FE technique solves a set of hyperbolic wave equations in the zone of influence of the wave front, and accordingly does not require coupling of large numbers of equations. On the other hand, the unconditionally stable implicit solvers provide a solution for all coupled equations of motion, which require assembly of a global stiffness matrix. For crash simulations involving extensive use of contact, multiple material models and a combination of non-traditional elements, explicit solvers are more robust and computationally more efficient than implicit solvers.

The stability of explicit solution is conditional as discussed before; it is determined by the Courant's condition:

$$\Delta t \leq \frac{l_c}{c} \quad (1.34)$$

The time step of the discretization in the time domain, Δt , must not exceed the value obtained by dividing the element characteristic length with the acoustic wave speed through the material of the element. This requirement means that the numerical time step must be smaller or equal to the time needed for the physical stress wave to cross the element. For instance, a typical automotive application using mild steel elements ($c=5000$ m/s) with a characteristic length of 5 mm, results in an analysis time step of 1 microsecond. Explicit methods are suited for short duration problems, for example high loading velocity or highly nonlinear problems that require small time-steps for accuracy reasons.

1.8 Materials calibration flow chart



2. Calibration of steels

This chapter concern a procedure suitable for a large range of steels, this model needs data from tensile tests that are available for free from a database called Autosteel belonging to Steel Market Development Institute [32]. For clarity reasons, the procedure for the material calibration will be exposed referring to a sample material, for this aim a Dual Phase steel, DP600, has been chosen.

2.1 Hardening law calibration

When approaching to a material calibration for crash simulation purpose, the first step is the description of the plasticity of the material, that is demanded to the hardening law. As discussed in section 1.3, many equations have been developed to describe the ductility of a material. A very simple and common choice could be the Hollomon flow curve or power law (1.6), it has only two parameters and the exponent “ n ”, called hardening exponent, is equal to the strain at Ultimate Tensile Strength (UTS). This model can be used but it is not the most accurate, a better practise is to test various hardening laws with a best fit procedure and chose the one showing the best correlation with experimental data. The results of this step for DP600 are presented in Fig. 14.

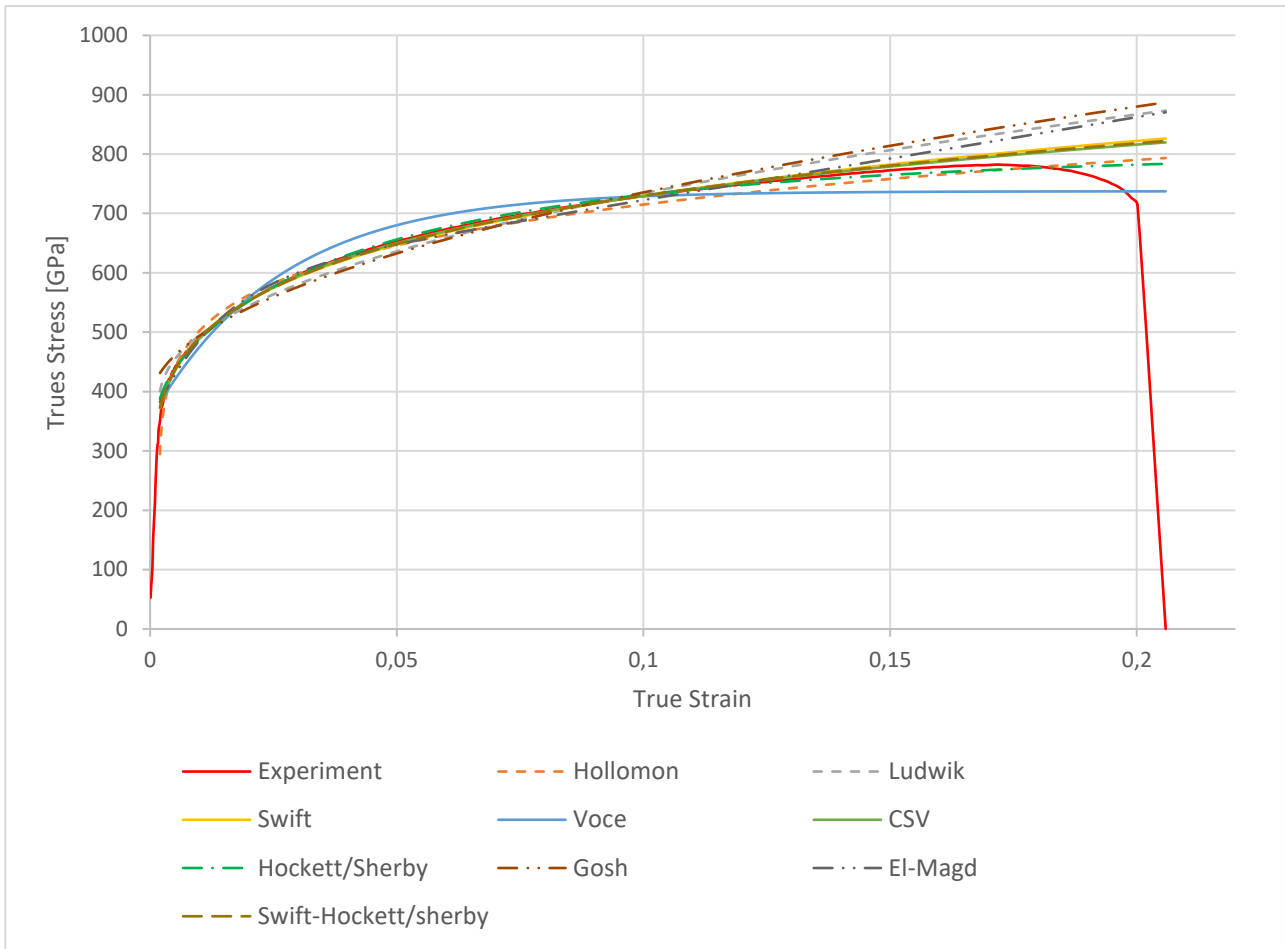


Figure 14: Quasistatic Models: DP600 Results

The first step of the fitting procedure consists in choosing a hardening law, Combined Swift-Voce (CSV) for instance:

$$\sigma(\bar{\epsilon}_p) = \alpha A(\bar{\epsilon}_p + \epsilon_0)^n + (1 - \alpha) \left[k_0 + Q \left(1 - \text{EXP}(-\beta \bar{\epsilon}_p) \right) \right] \quad (2.1)$$

Then all the parameters must be set for a first attempt of the fitting cycle. Parameters related to known physical characteristic can be fixed at the beginning of the process and left out of the optimization. Using the abscissa of the curve subjected to fitting, one can calculate the respective points of the first attempt curve. To improve the quality of the regression the least-squares method has been used. This method uses the residual of a model to a data point to evaluate its fit:

$$r_i = y_i - f(x_i) \quad (2.2)$$

The optimization proceeds iteratively trying to minimize the sum of the squared residuals with the model parameters as degrees of freedom.

$$S = \sum_{i=1}^n r_i^2 \quad (2.3)$$

The optimization has been performed using the solver implemented in Microsoft Excel®.

Correlation coefficient can be calculated to assess the quality of the fit and to compare different fitting hardening laws. Correlation coefficient is calculated between data and model points, it assumes a value between 0 and 1, where 1 indicate perfect correlation and 0 no correlation. The equation for correlation is:

$$Correl(X, Y) = \frac{\sum(x-\bar{x})(y-\bar{y})}{\sqrt{\sum(x-\bar{x})^2 \sum(y-\bar{y})^2}} \quad (2.4)$$

The Combined Swift-Voce (CSV) (2.1) model has the best correlation with the DP600 experimental flow curve, for different type of steel another model could fit the data better than the CSV or return comparable results with fewer parameters.

<i>Combined Swift-Voce</i>	<i>A</i>	ϵ_0	<i>n</i>	k_0	<i>Q</i>	β	α
$\alpha A(\bar{\epsilon}_p + \epsilon_0)^n + (1 - \alpha) [k_0 + Q(1 - \text{EXP}(-\beta \bar{\epsilon}_p))]$	1076,48	0,0018	0,16952	12,289	43,717	6,068	0,85836

Table 3: DP600 CSV Parameters

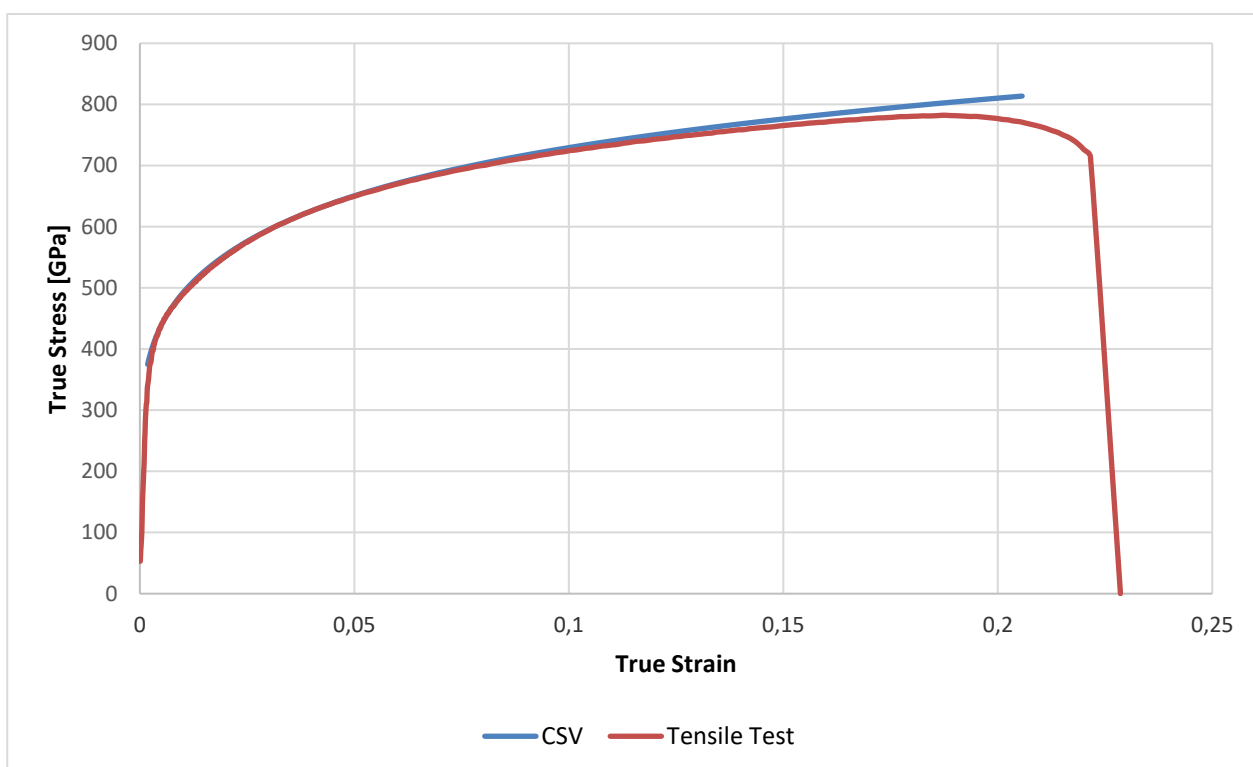


Figure 15: DP600 CSV Hardening Curve

The set of parameters obtained results in a flow curve that fits with experimental data of a single test on a single specimen and this can't represent the totality of the possible cases. Different specimens can show higher or lower yield strength or ultimate tensile strength, but the stress-strain shape of the curve can reasonably be considered to remain the same. Usually, materials are described

not with fixed values for their properties but with ranges between a maximum and a minimum tolerance. The flow curve ($\sigma[\varepsilon_p]$) can be scaled and shifted to meet these limit values, for this purpose two parameters, A and B, have been introduced with this form:

$$\sigma = A + B \sigma[\varepsilon_p] \quad (2.5)$$

Referring to VW Standard 50036 it's possible to use the followings values for UTS and YS maximum and minimum.

<i>Material</i>	<i>YS [GPa]</i>	<i>UTS [GPa]</i>
<i>CR330Y590T-DP</i>	330-430	590-700

Table 4: Mechanical Properties of Dual Phase Steel DP600

Parameters A and B are obtained, for each curve, with an optimization that minimize the squared residuals for YS and UTS respectively at $\varepsilon_p = 0$ and $\varepsilon_p = n$, the process is the same used previously. One can set A and B to reach the highest values for UTS and YS, that is the maximum tolerance condition. A more conservative approach could be to use the lowest values for mechanical properties available on regulations to modify the flow curve. Anyway, once these characteristics are chosen, the hardening curve can be easily modified. The following results represent the flow curve for DP600 with three different tolerances, maximum, minimum and medium. One can see that the

combined Swift-Voce curve interpolated with the tensile test data, is located approximately in correspondence of the medium tolerance curve Fig.16.

A max	B max	A min	B min	A med	B med
0,949067	74,08327	0,880476	-0,19421	0,914771	36,94453

Table 5: Parameters for hardening curves at maximum, minimum and medium tolerance

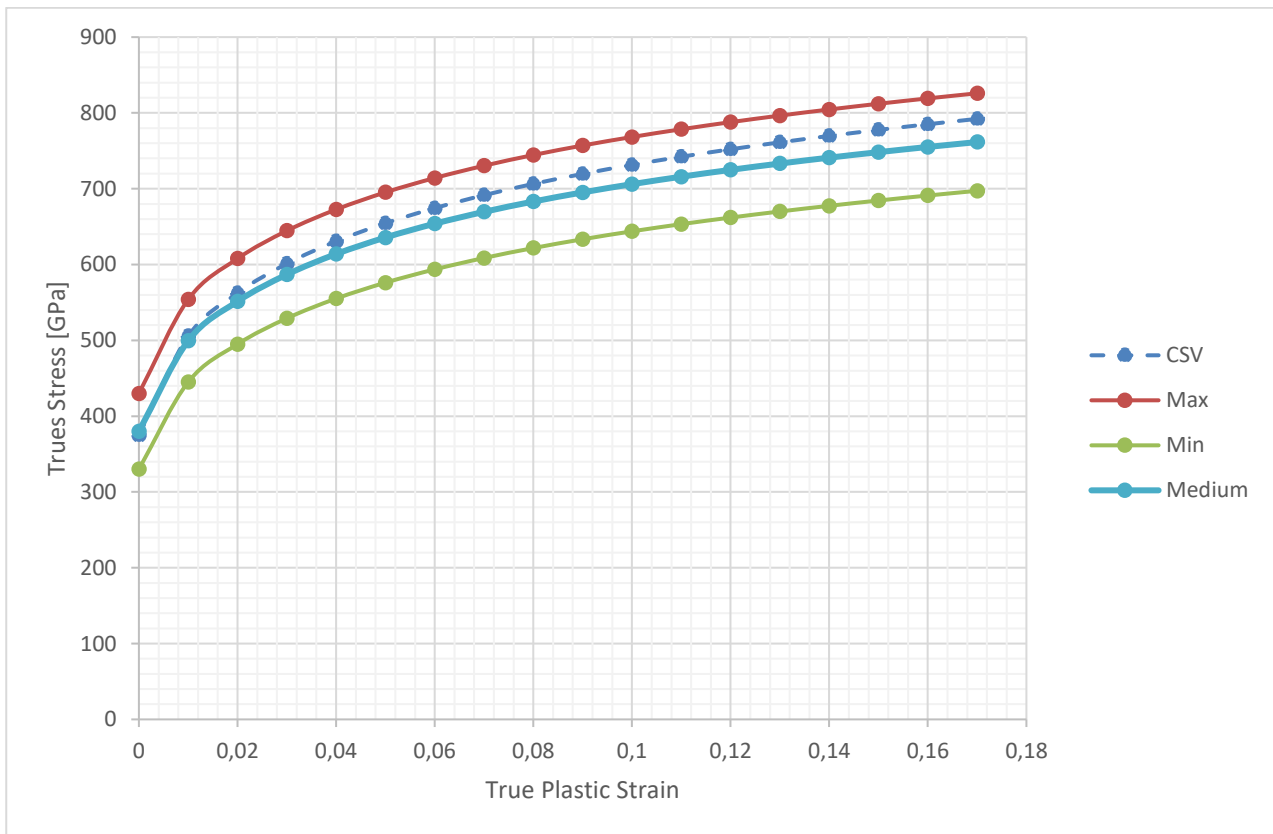


Figure 16: Scaled hardening curve for DP600 according to maximum, minimum and medium tolerance

2.2 Dynamic flow curve modelling

Dynamic flow curves are increasingly needed for automotive crash FEM-Simulations. New models have been implemented in commercial FEM simulation software and model parameters are required as input data for FEM simulations. Each flow curve should be extrapolated at high strain levels up to at least $\varepsilon = 1,0$. This can be done for each individual flow curve with an analytical model. Dynamic models are based on a quasistatic model extended to take into account strain rate effects.

The dynamic behaviour of materials is given with a set of strain rates mostly 1, 10, 100, $250s^{-1}$ according to a German dynamic testing guideline [33]. Additionally, higher strain rate from 500 up to $1000s^{-1}$ are sometimes required for automotive application.

The determination of the strain rate sensitivity is not standardised so far. Larour [34] in his thesis provided a reliable method for a quantitative experimental determination of the strain rate sensitivity. He plotted the flow stress out of each experimental dynamic flow curve he obtained from dynamic tests versus logarithmic strain rate for a specific true plastic strain value, Fig. 17.

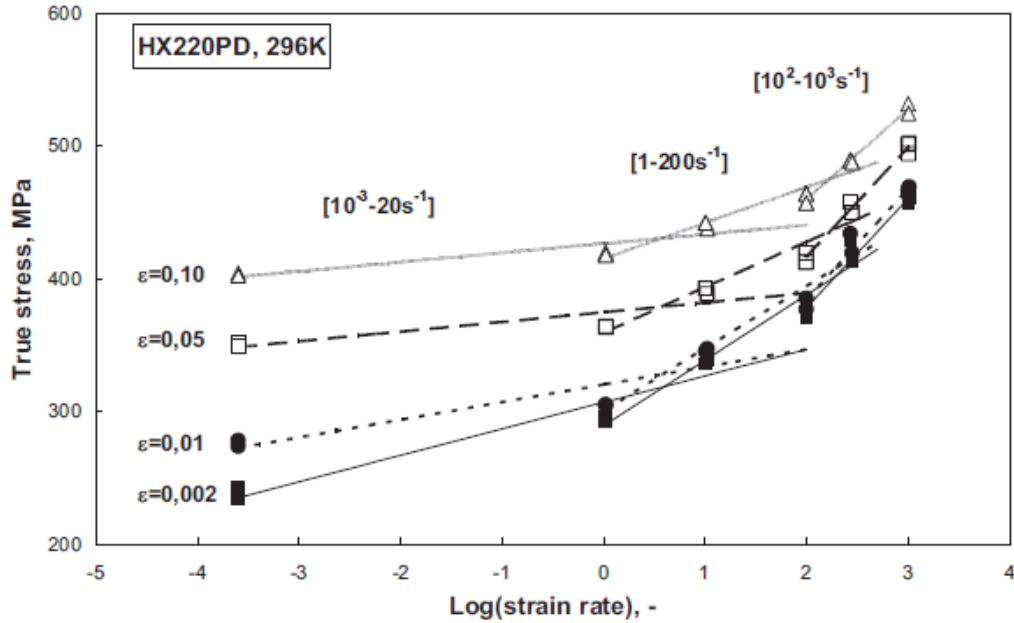


Figure 17: Low, intermediate and high strain rate sensitivity at increasing true plastic strain [34]

Usually the strain rate sensitivity increases with increasing strain rate, for this reason, it is important to specify the strain and strain rate level chosen when comparing strain rate sensitivity values. The average strain rate sensitivity is usually determined by a linear regression of the flow stress versus strain rate in a semi-log or log-log scale. A linear regression over a wide strain rate range causes a poor fitting correlation. However, if the strain rate range is split between different strain rate regions [4], for example a low strain rate ($[10^{-3} - 20 \text{ s}^{-1}]$), an intermediate strain rate ($[1-200 \text{ s}^{-1}]$) and a high strain rate region ($[10^2 - 10^3 \text{ s}^{-1}]$), then a linear fitting is suitable (Fig. 17). The average strain rate sensitivity is suitable for experimental comparisons and is mostly used in the literature, since determined in an objective manner.

Larour in his work [34] chose three true plastic strain levels, 0,002, 0,05 and 0,10 to analyse his experimental results. He outlined a power law fitting curve of the strain rate sensitivity m versus

the quasistatic yield strength with a relatively good correlation (Fig.18, 19). At any strain, the higher the yield strength, the lower the strain rate sensitivity. The strain rate sensitivity decreases with increasing plastic strain, whereas only some minor differences can be observed between 0,05 and 0,10 true plastic strain.

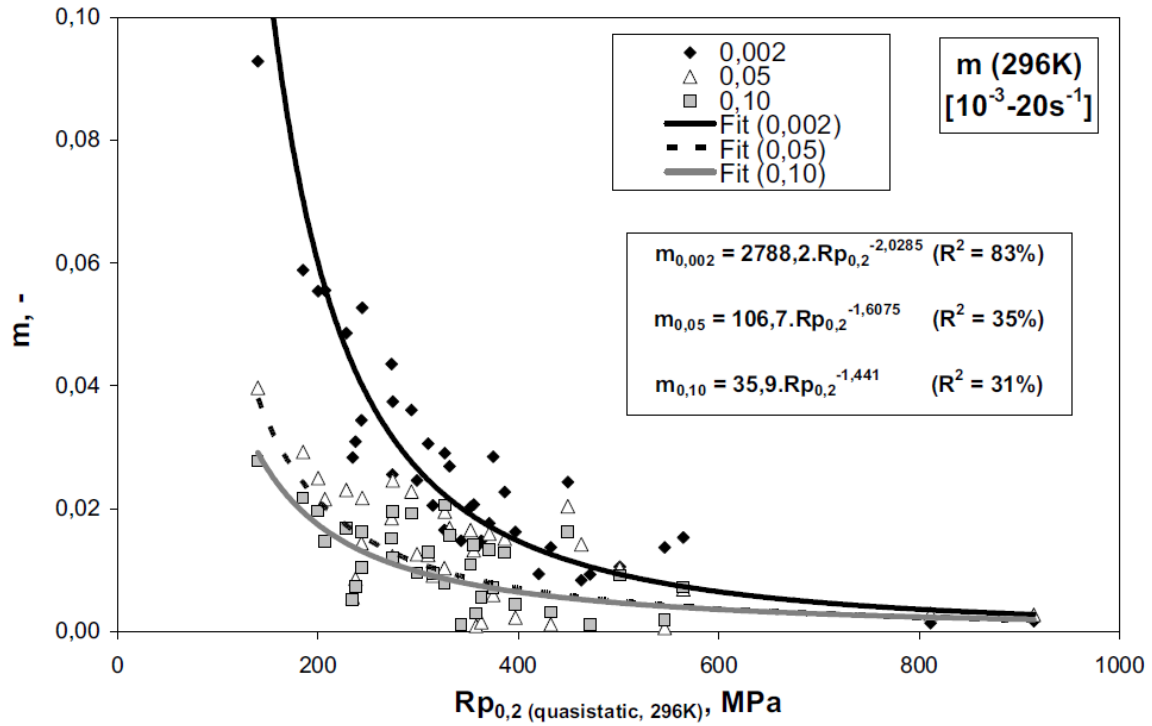


Figure 18: Low strain rate log. strain rate sensitivity m vs. quasistatic $R_{p0,2}$ -Power fitting of experimental data ([10⁻³-20s⁻¹], $\epsilon = 0,002/0,05/0,10$; 296K) [34]

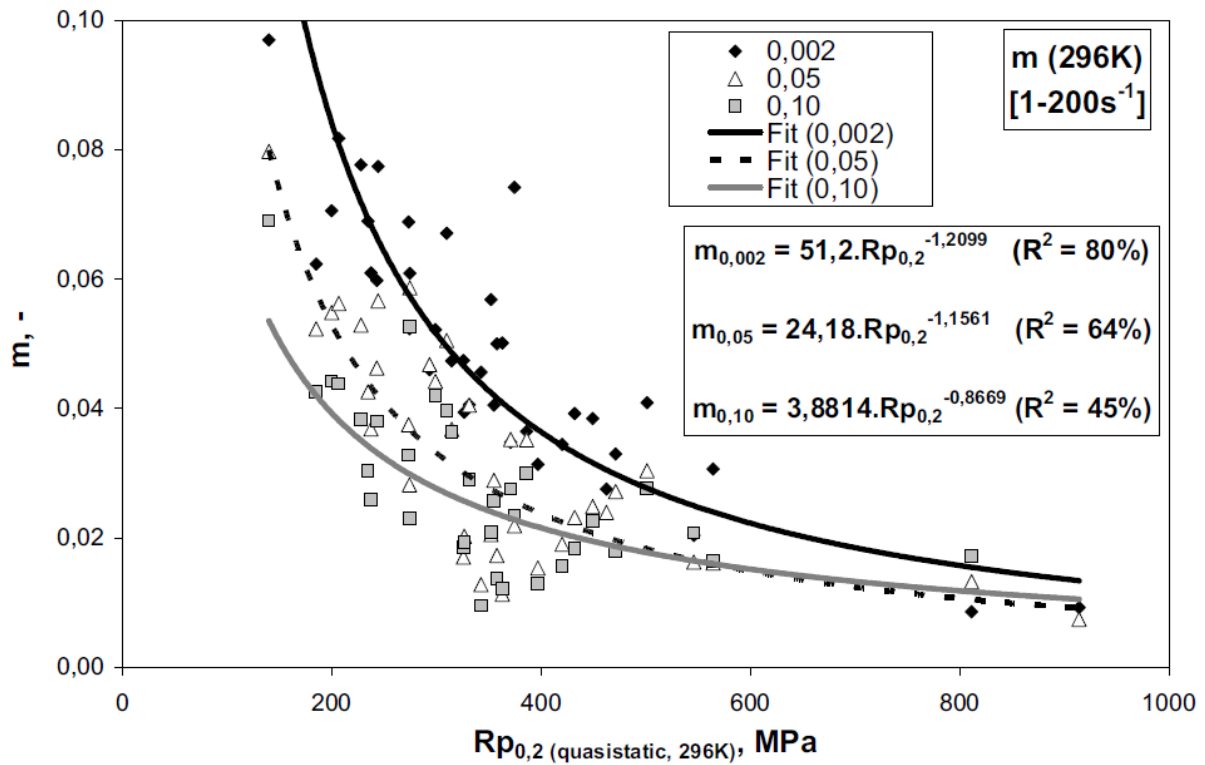


Figure 19: Intermediate strain rate log. strain rate sensitivity m vs. quasistatic $Rp_{0,2}$ -Power fitting of experimental data ($[10^{-3}-20s^{-1}]$, $\epsilon=0,002/0,05/0,10$; 296K) [34]

Larour did not provide any fit of experimental data for high strain rate ($[10^2 - 10^3 s^{-1}]$), anyway good results can be obtained using the same strain rate sensitivity used for intermediate ($[1-200 s^{-1}]$) strain rate as shown in Fig. 20. With the equations in Fig. 18 and 19, one can calculate the strain rate sensitivity m , then the true stress values for a strain respectively equals to $\epsilon = 0,002/0,05/0,10$ are calculated using (1.17). Dynamic flow curves can be interpolated with these points, assuming the strain rate curves will have the same shape of the quasistatic curves, the interpolation can be performed using (1.40) and the quasistatic hardening law. The dynamic flow curves calculated with this method for DP 600 have been compared with the experimental curves provided by the material database [32]. In Fig.14 it is possible to see that there is a good correlation between what has been measured on real tests and what has been obtained with an empirical model.

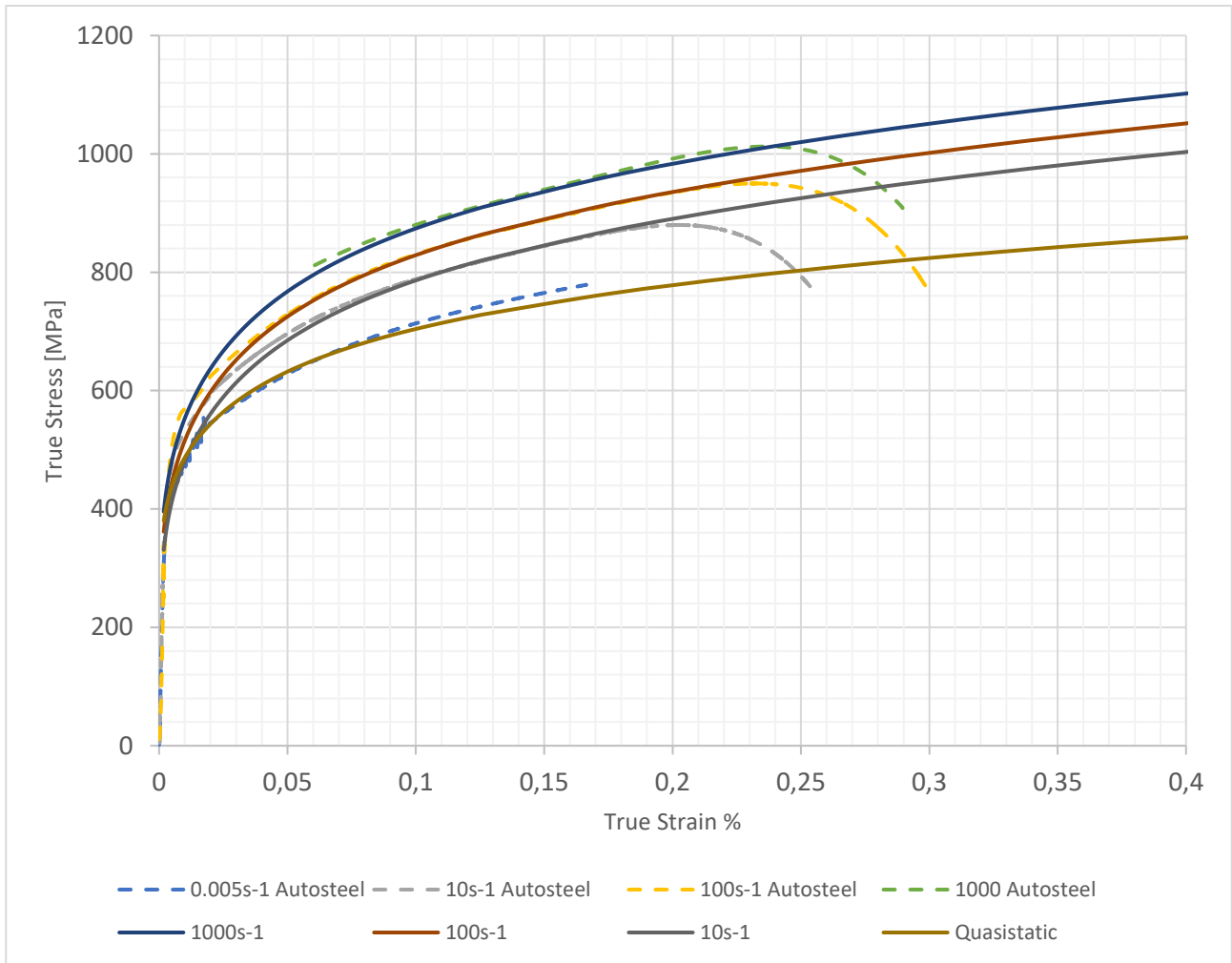
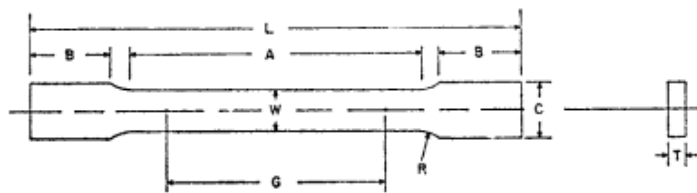


Figure 20: Strain Rate Curves, comparison between DP600 strain rate curves from Autosteel database and Larour's model results

2.3 Tensile Test Simulations

The results of the previous stages have been communicated to the solver PAMCRASH® through the material card MAT 1 for solid elements. It requires the shear modulus, the density, the bulk modulus of the material and the hardening curve. A finite elements simulation has been run in order to verify the quasistatic flow curve fitted with the tensile test data. Specimen dimensions were defining according to ASTM E8/E8M (Fig.21). To avoid problems mesh dependency related, a solid mesh has been used with a scaling dimension of the elements from 5 mm to 0,2 mm in the necking zone. Along the thickness there are five elements for a total thickness of 1 mm. Only a quarter of the specimen, with the proper boundary conditions, has been used in the simulation, that has been possible thanks to the symmetry of the load and of the geometry. This reduced considerably the length of the simulation.



	Dimensions		
	Standard Specimens		Subsize Specimen
	Plate-Type, 40 mm [1.500 in.] Wide	Sheet-Type, 12.5 mm [0.500 in.] Wide	6 mm [0.250 in.] Wide
	mm [in.]	mm [in.]	mm [in.]
G —Gauge length (Note 1 and Note 2)	200.0 ± 0.2 [8.00 ± 0.01]	50.0 ± 0.1 [2.000 ± 0.005]	25.0 ± 0.1 [1.000 ± 0.003]
W —Width (Note 3 and Note 4)	40.0 ± 2.0 [1.500 ± 0.125, -0.250]	12.5 ± 0.2 [0.500 ± 0.010]	6.0 ± 0.1 [0.250 ± 0.005]
T —Thickness (Note 5)		thickness of material	
R —Radius of fillet, min (Note 6)	25 [1]	12.5 [0.500]	6 [0.250]
L —Overall length, min (Note 2, Note 7, and Note 8)	450 [18]	200 [8]	100 [4]
A —Length of reduced section, min	225 [9]	57 [2.25]	32 [1.25]
B —Length of grip section, min (Note 9)	75 [3]	50 [2]	30 [1.25]
C —Width of grip section, approximate (Note 4 and Note 9)	50 [2]	20 [0.750]	10 [0.375]

Figure 21: Specimen Dimension according to ASTM E8/E8M

The bottom edge of the specimen was fixed then a displacement has been applied to the upper edge, the displacement law used is time linear. The result of the simulation can be summarized with a stress-strain chart, in Fig. 25. One can see that there is a good correlation between the FEM analysis and the real tests, this means that the hardening law obtained with the optimization can represent the real material with a good reliability. There are some discrepancies in the failure phase because none fracture mode was set for this simulation.

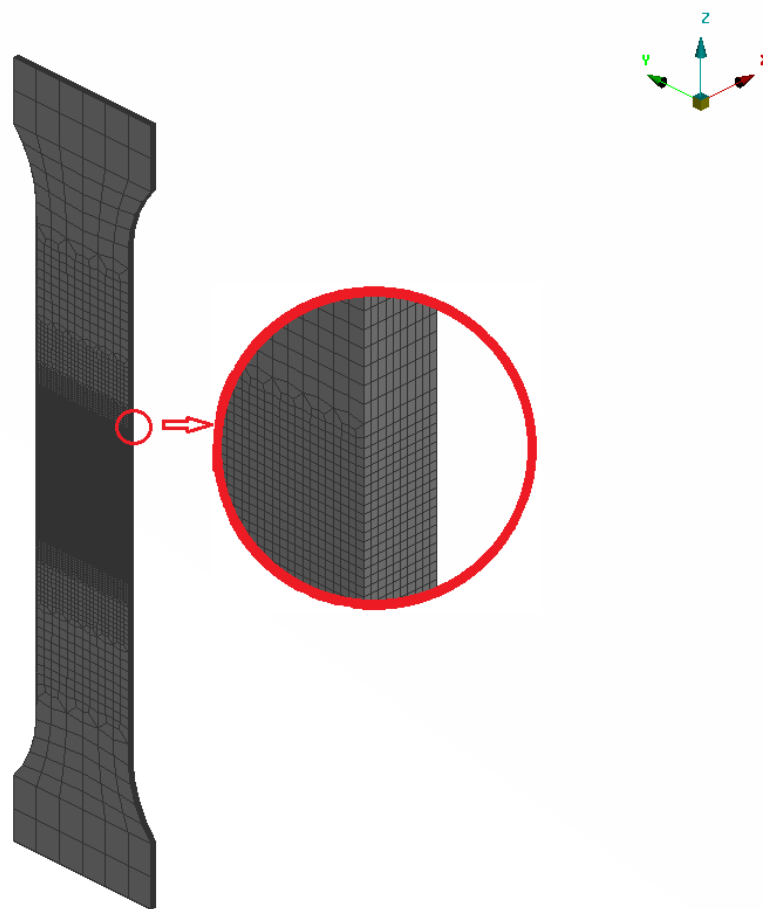


Figure 22: Specimen mesh

In Fig. 23 and in Fig. 24 it is possible to appreciate the diffused and the localized necking zones, small solid elements can faithfully capture this phenomenon. This capacity vanishes with bigger shell elements, this is why necking criteria are needed.

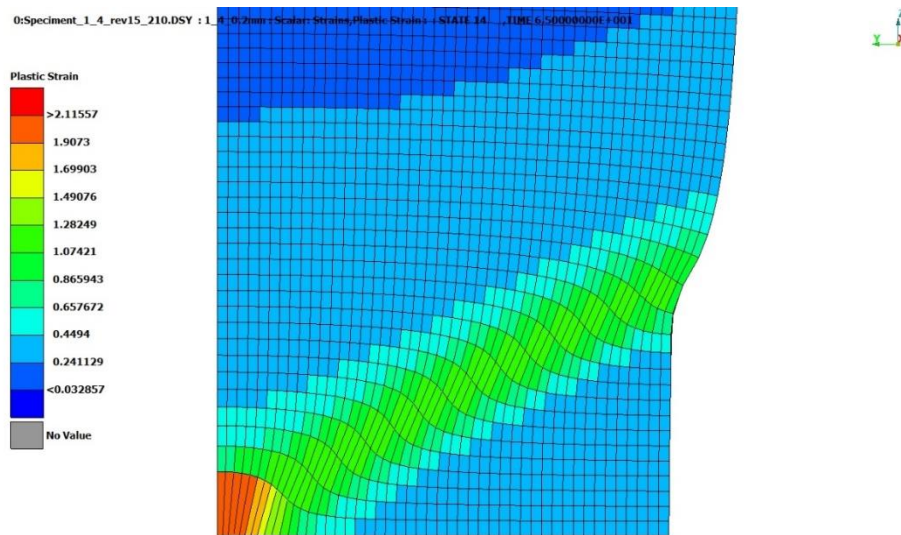


Figure 23: Localized and diffuse necking captured during the simulation

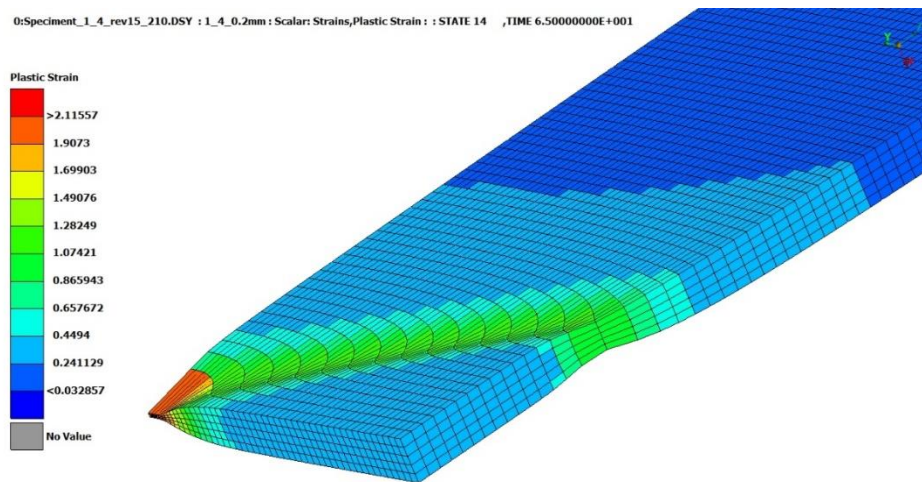


Figure 24: Reduced thickness in the localized necking zone

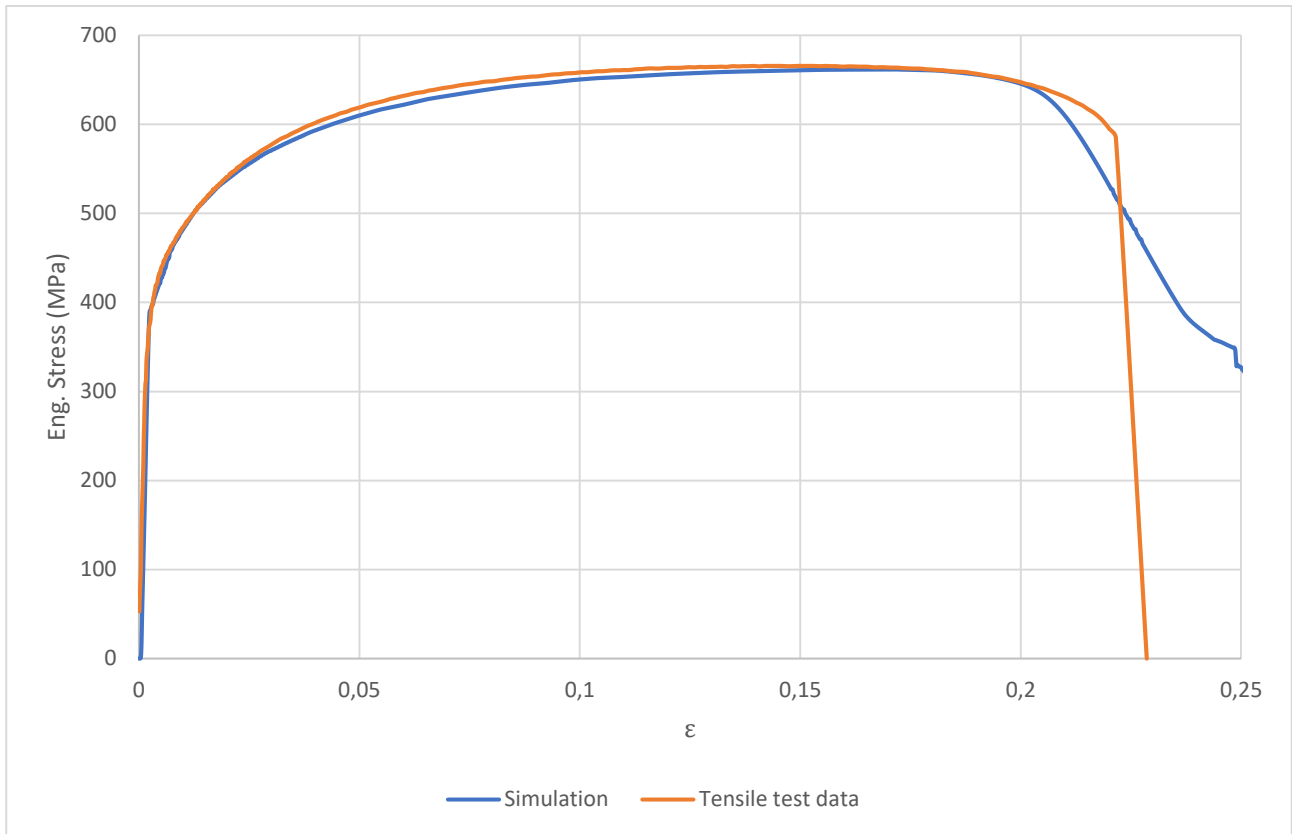


Figure 25: Simulation results vs Tensile test data from Autosteel

2.4 Axial crash simulations

With the tensile test simulation, the quasistatic flow curve has been verified. In this section the adaptability of the model and the reliability of the strain rate curves will be investigated. For this purpose, a crash box FE model has been used, the structure represented in Fig. 26 is a sheet metal box with a series of features for the trigger of the collapse, the impact structure is a 500 kg block with initial speed equals to 8.95 m/s. A MAT 105 material card has been applied to the coarse shell element mesh with a characteristic length of 5mm. That card requires Young's Modulus, Poisson's ratio, density, hardening law and strain rate curves of the material. One can add also a damage model and an element elimination criterion, for this purpose Hill-Stören-Rice model can be very suitable since

it returns good result with just one parameter “n” as discussed in section 1.5.2. “n” is the equivalent plastic strain at necking, and it is communicated to PAMCRASH® through the parameter REL_HSR. Equation (2.6) relates “n” to REL_HSR.

$$n = |\ln (REL_HSR)| \quad (2.6)$$

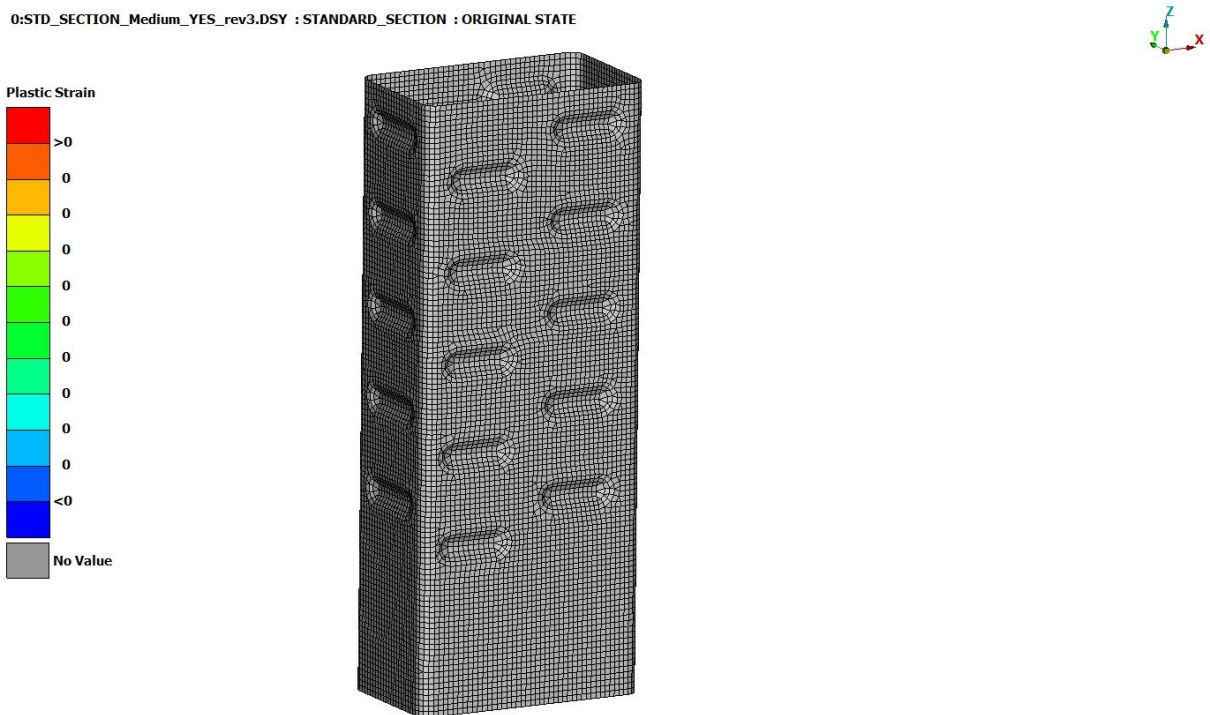


Figure 26: Sheet metal crash box FEM model

The aim is to verify that the performance of the calibrated material is comparable with the respective counterparts obtained with a model created by an original equipment manufacturer (OEM), called OEM material from hereinafter. First of all, the hardening curve has been translated and scaled

with (2.5) to achieve the same yield strength and ultimate tensile strength of the OEM material, then the strain rate curves have been calculated with the method explained in section 2.2.

A comparison of the respective geometry obtained after the crash could be a first qualitative method to study the performance of the calibrated material, anyway the final shape of the crashed box is strongly affected by the collapse sequence of the elements and little discrepancies in material description cause a very different geometry, as one can see in Fig. 27 and 28.

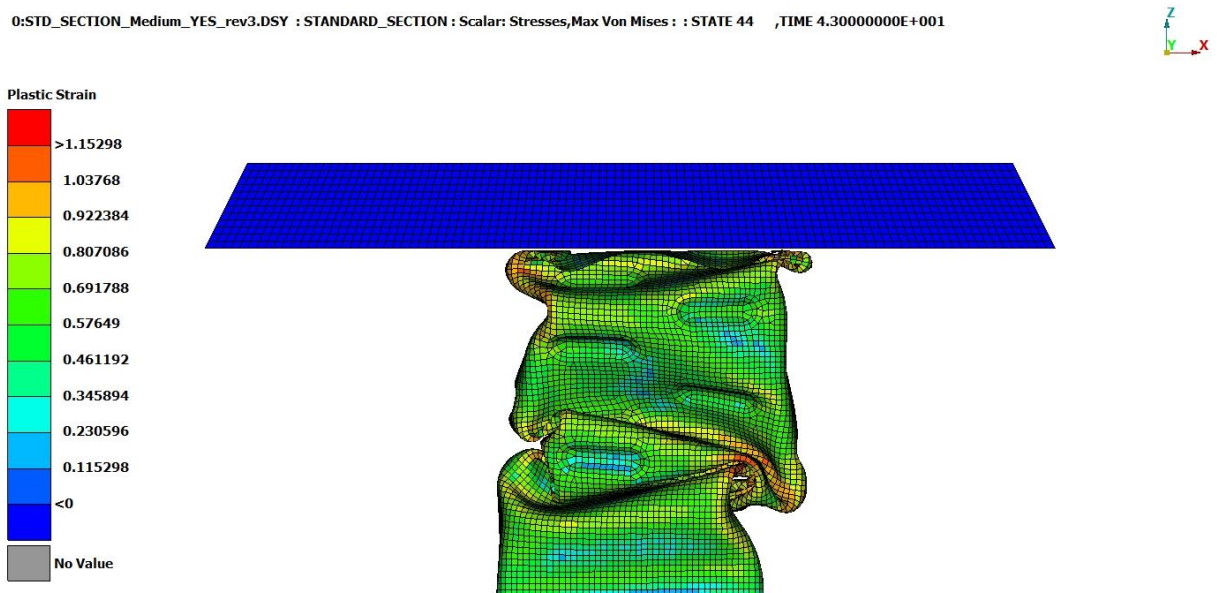


Figure 27: Collapsed crash box, calibrated DP 600

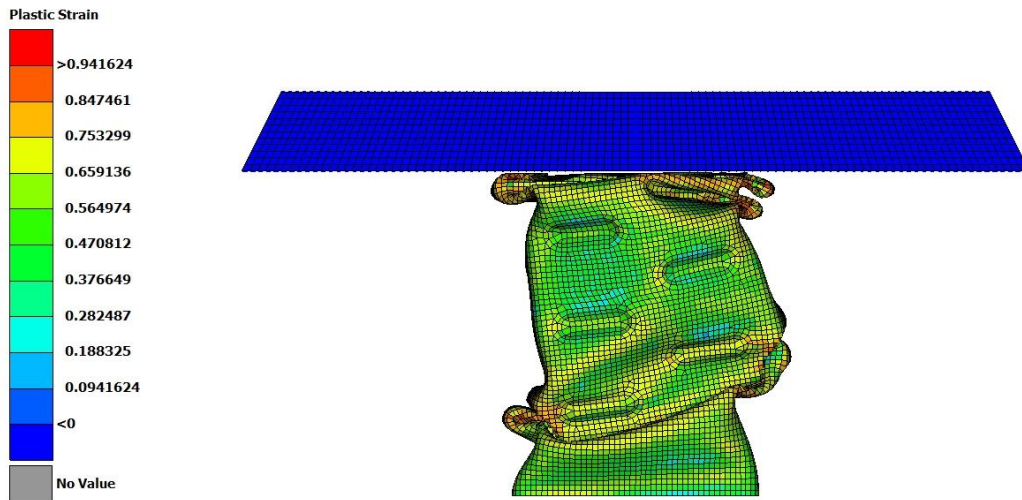


Figure 28: Collapsed crash box, OEM DP600

A more quantitative method is the comparison of the force-displacement charts (Fig. 29), the underlying area of the plot represent the energy absorbed during the crash. This is a very important parameter, the energy absorbed during a crash is an indication of the efficiency of the material during a crash event. A reliable estimation of the energy absorption of the materials is crucial to design safe structures. One can see that despite of the final shape, the energy absorbed by the two material is nearly the same, this means that calibrated DP600 performance is comparable with the OEM material one.

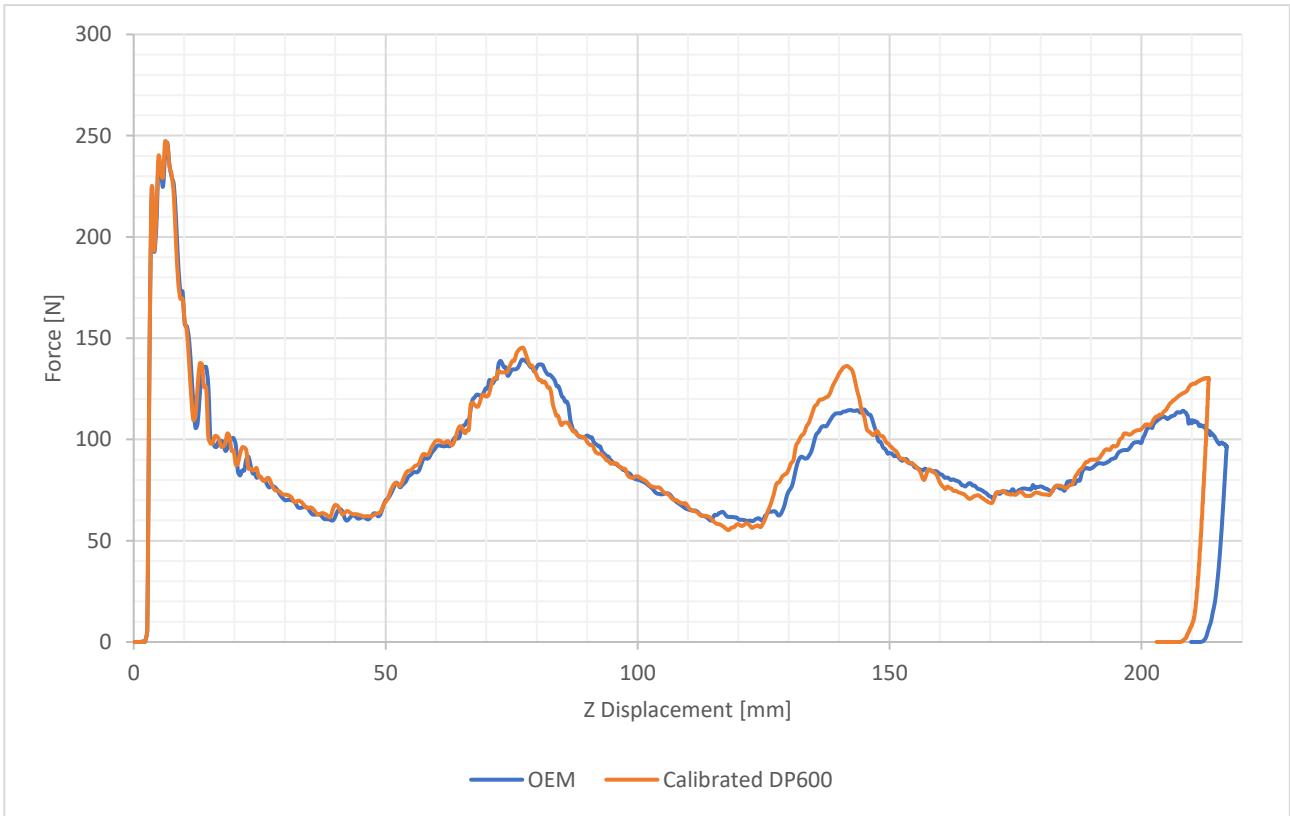


Figure 29: Force-Z displacement plot

3. Martensitic Steel Calibration

The increasing demand to reduce vehicle weight for improved fuel efficiency, while maintaining crash performance, has led to the application of new and innovative materials and manufacturing processes in the automotive industry. Hot stamping of boron steel is widely used to produce Ultra High Strength Steel (UHSS), this process allows steel to be formed in complex shapes with different quench conditions and a tensile strength up to 1500 MPa. These properties are the result of in-die quenching which causes a solid-state phase transition from austenite to martensite during the formation process. The hot stamping process is currently used to manufacture structural components such as bumper beams, door intrusion beams, A- and B-pillar, roof and side rails.

Although components with a fully martensitic microstructure are often desired due to their exceptional high strength and intrusion resistance, some structural components, such as a B-pillar, may benefit from regions of reduced strength and greater ductility for improved energy absorption and fracture resistance. This class of hot stamped parts are said to have “tailored properties” and various hot stamping processes exist which are capable of creating such a part.

This process utilizes a segmented hot stamping die with one segment that remained at room temperature while the other segment was heated to 400 °C. The as-quenched Vickers Hardness (HV) of the B-pillar region hot stamped within the heated die segment varies from 244 HV to 260 HV, while the average as-quenched Vickers hardness of the section hot stamped within the room temperature die segment is 475 HV. The lower hardness of the tailored region is due to sub-critical cooling rates (less than 30 °C/s) imposed on the blank during hot stamping, which allow some volume

fraction of bainite (and/or ferrite) to form as shown in the continuous cooling transformation (CCT) diagram in Fig. 20.

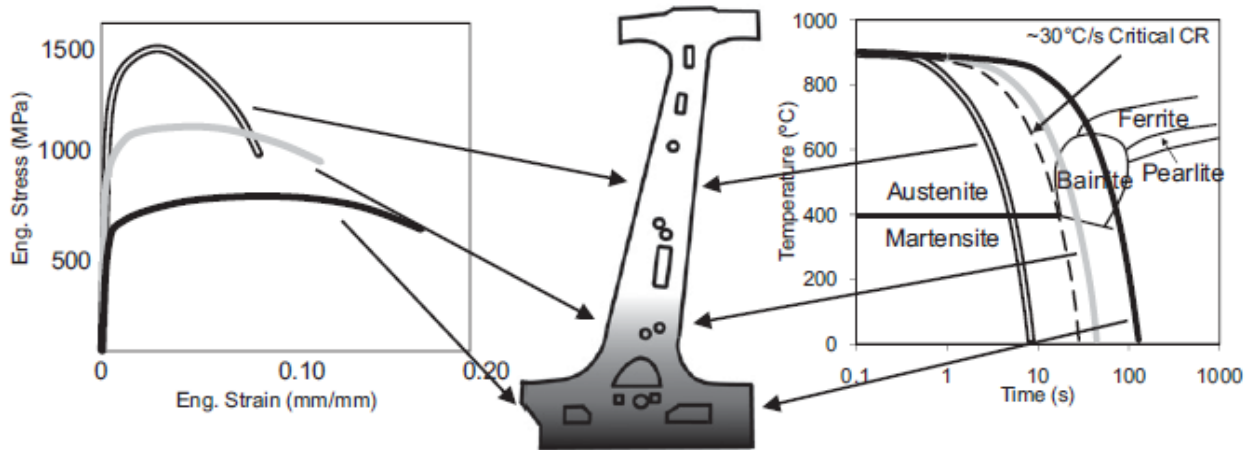


Figure 30: Schematic of a B-pillar with tailored properties shown with a USIBOR 1500P CCT diagram.

It is useful to have a model easily adaptable to different values of Vickers Hardness for martensitic steels with tailored properties. In a crash model each zone with a different HV must be described as a single material because the amount of martensite in the alloy change dramatically the properties of the steel.

3.1 Hardening law

There is not a database containing martensitic steel tensile test data that can be used as in the previous part of this work. Even if present, tests should cover a wide range of HV because the relation between steel properties and HV is not linear and it can't be easily deduced.

3.1.1 Tailored Crash Model

A. Bardelcik et al. [35] developed the Tailored Crash Model (TCM), which is a constitutive model depending on strain, strain rate, and HV. Boron steel sheet metal blanks were austenized and quenched at five different cooling rates, which resulted in as-quenched microstructures that ranged from bainitic to martensitic. Tensile specimens were machined from the quenched blanks and tested in tension at four strain rates tests, the true stress versus effective plastic strain curves were used to develop the TCM. The resulting model for the flow curve is a Voce constitutive model with a strain rate contribution, the expressions and the relative parameters are reported below:

$$\sigma = f(\varepsilon, \dot{\varepsilon}, HV) = \left[A(HV) + \left[(B(HV) - A(HV)) e^{\left(-\frac{\varepsilon}{C(HV)} \right)} \right] \right] [1 + \dot{\varepsilon}]^{D(HV)} \quad (3.1)$$

$$A(HV) = A_2 HV^2 + A_1 HV + A_0 \quad (3.2)$$

$$B(HV) = B_1 HV + B_0 \quad (3.3)$$

$$C(HV)_{266 < HV < 375} = C_3 HV^3 + C_2 HV^2 + C_1 HV + C_0 \quad (3.4)$$

$$C(HV)_{HV > 375} = C_0^* \quad (3.5)$$

$$D(HV) = D_0 \quad (3.6)$$

$A(HV)$	-	A_2 $= 5.318 \times 10^{-3}$	$A_1 = -0.7902$	$A_0 = 699.49$
$B(HV)$	-	-	$B_1 = 2.499$	$B_0 = -71.24$
$C(HV)_{266 < HV < 375}$	C_3 $= -7.747 \times 10^{-9}$	C_2 $= 9.222 \times 10^{-6}$	C_1 $= -3.652$ $\times 10^{-3}$	$C_0 = 0.4484$
$C(HV)_{HV > 375}$	-	-	-	$C_0^* = 0.0072$
$D(HV)$	-	-	-	$D_0 = 0.018$

Table 6: The constant parameters for equations (3.2)-(3.6) [35]

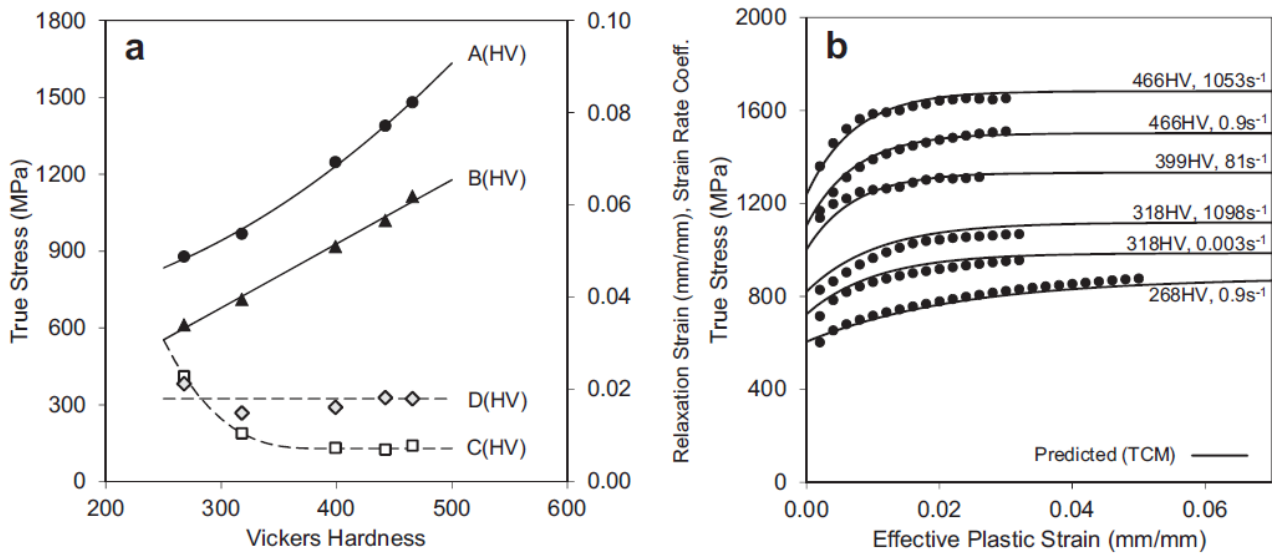


Figure 31: (a) Voce material parameters plotted as a function of the Vickers hardness and (b) The measured (symbols) and TCM predicted (curves) flow stress curves for a variety of as-quenched Vickers hardness and strain rate values [35]

As an additional step is possible to find the Voce material parameters as function of the Vickers hardness for the classical formulation:

$$\sigma_v[\bar{\epsilon}_p] = k_0 + Q(1 - e^{-\beta\bar{\epsilon}_p}) \quad (3.7)$$

For this purpose, quasistatic curves have been calculated for boron steels in a range from 200 HV to 480 HV with TCM model, then interpolated with (3.7) with an optimization process that returns the fitting parameters. This HV range has been chosen because it covers almost all the possible microstructures, from fully bainitic to fully martensitic. Parameters for equation (3.7) are presented as function of the Vickers Hardness, Fig. 32.

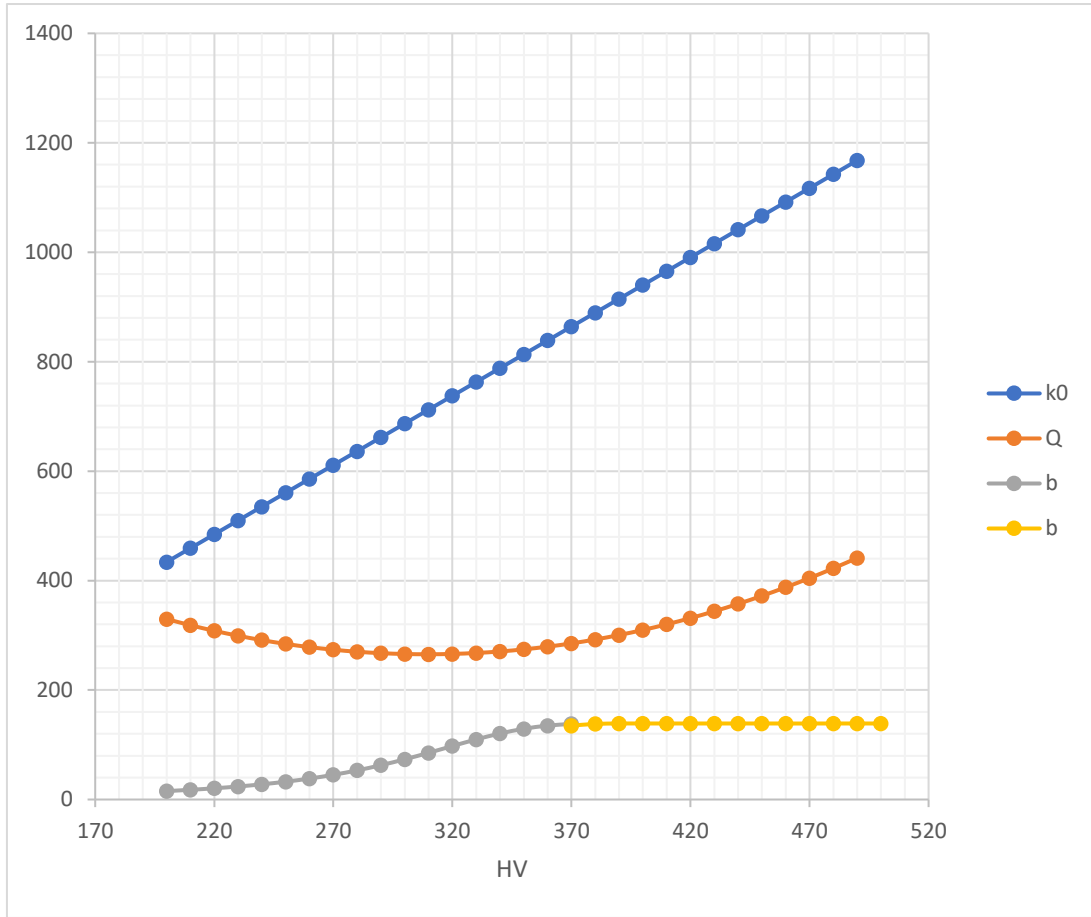


Figure 32: Voce law parameters as a function of Vickers hardness

$$k_0(HV) = k_{01}HV + k_{00} \quad (3.8)$$

$$\beta_{HV < 370}(HV) = \beta_3 HV^3 + \beta_2 HV^2 + \beta_1 HV + \beta_0 \quad (3.9)$$

$$\beta_{HV > 370}(HV) = \beta_1^* HV + \beta_0^* \quad (3.10)$$

$$Q(HV) = Q_2 HV^2 + Q_1 HV + Q_0 \quad (3.11)$$

$k_0(HV)$	-	-	-	$k_{0_1} = 2,5304$	k_{0_0} $= -72,133$
$\beta_{HV<370}(HV)$	β_4 $= -5,6794$ $\times 10^{-8}$	β_3 $= 5,0105$ $\times 10^{-5}$	β_2 $= -1,2362$ $\times 10^{-2}$	β_1 $= 0,9795$ $\times 10^{-4}$	$\beta_0 = 0,9998$
$\beta_{HV>370}(HV)$	-	-	-	$\beta_1^* = 0,0027$	$\beta_0^* = 137,66$
$Q(HV)$	-	-	$Q_2 = 0,0054$	Q_1 $= -3,3305$	$Q_0 = 780,41$

Table 7: Constant parameters for equations (3.8) -(3.11)

These parameters result in a model equivalent to the TCM, the expression of the Voce formulation has been changed only for coherence purpose. From hereinafter the strain rate contribution will be neglected to simplify the exposition of the model which remains strain rate sensitive.

3.1.2 Model refinement

In crash simulations the post necking region of flow curve is very important for a reliable result, K. Pack and S. J. Marcadet in their work [36] used a combined Swift-Voce hardening law to interpolate tensile tests data for a fully martensitic boron steel using the following parameters:

<i>Combined Swift-Voce</i>	<i>A</i>	<i>ε₀</i>	<i>n</i>	<i>k₀</i>	<i>Q</i>	<i>β</i>	<i>α</i>
$\sigma = \alpha A(\bar{\varepsilon}_p + \varepsilon_0)^n$ $+ (1 - \alpha) \left[k_0 \right.$ $\left. + Q \left(1 - EXP(-\beta \bar{\varepsilon}_p) \right) \right]$	2458	3,696	0,1170	921,9	662,6	208,3	0,3
		$\times 10^{-5}$					

Table 8: Plasticity model parameters for pure isotropic hardening [36]

A fully martensitic boron steel has a Vickers hardness approximately equals to 480 HV, plotting the curves with the combined Swift-Voce parameters and with TCM model parameters (Fig.33) differences in the post-necking region are considerable. The saturation of the Voce hardening law is not suitable with the actual response of the material at high deformation which are frequent in crash events. The tailored crash model has to be modified in order to achieve a more representative post-necking region. This improvement is the main upgrade for the Tailored Crash Model developed in this thesis, this resulted in a new model, the Enhanced Tailored Crash Model (eTCM).

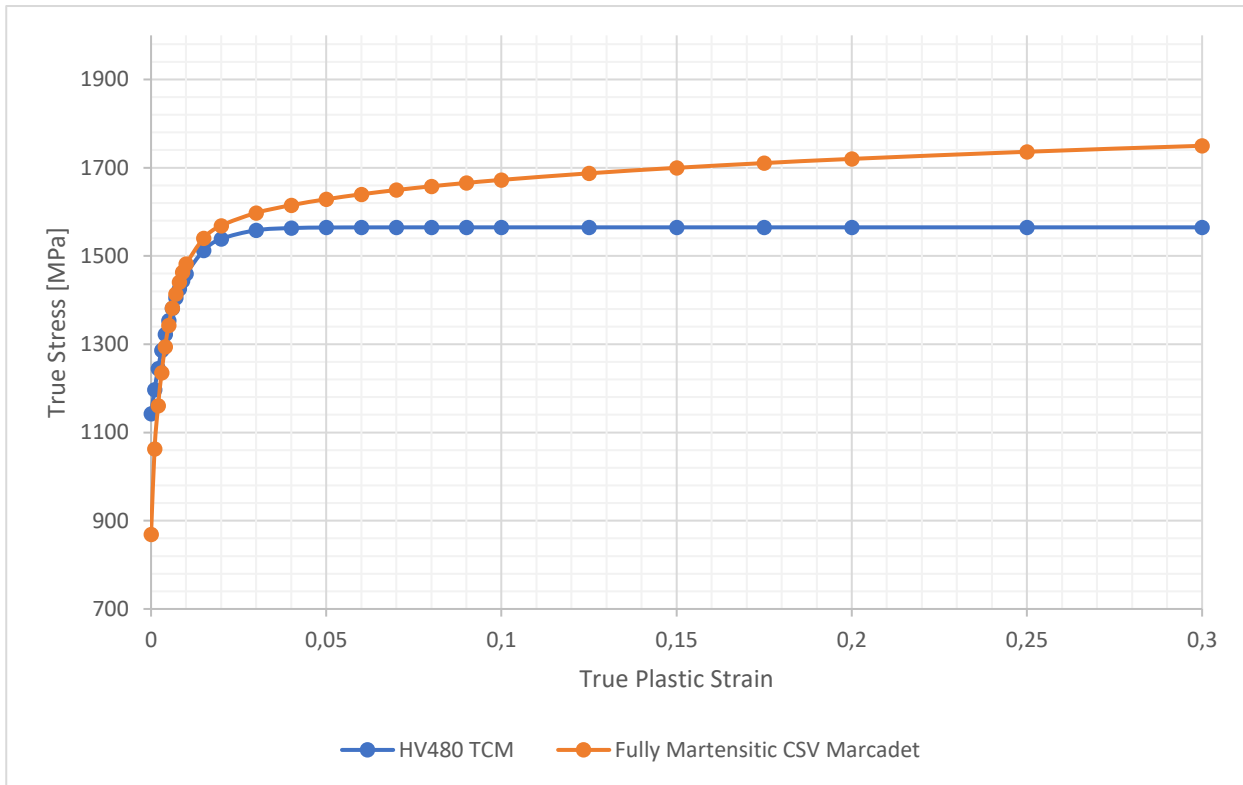


Figure 33: Plot of the hardening law for a fully martensitic boron steel calculated with CSV parameters (orange) and with TCM model parameters (blue)

Another important defect of Tailored Crash Model is the poor prediction of the localized necking and the diffuse necking. The diffuse necking stage starts at the beginning of the area reduction when the engineering stress reach a maximum, the strain rate field can be represented as a superposition of two crossing bands, the strain rate map present an hourglass shape and the two bands evolution are superposed, the two bands evolve at the same rate. The localized necking stage strain field can still be represented as the superposition of two crossing bands, but one of the bands starts to evolve faster than the other, while the other slows down and stops. [37]

In an analytical point of view diffuse necking is defined by the Considère criterion [38]. Consider a part of a tensile test specimen loaded with a tension force F and momentary cross-section area A , the momentary yield stress will be $\sigma = F/A$. Suppose that in that part a small section exists that has been strained additionally with a small strain $d\varepsilon \ll 1$, with resulting cross-section area A' and a stress σ' . Assuming the volume to remain constant the cross-section area A' of that part has reduced: $A' = A/(1 + d\varepsilon) \approx A(1 - d\varepsilon)$. The tension force in that section has to be equal to F , so that for the actual stress in that part $\sigma' A' = F = \sigma A$, consequently:

$$\sigma' = \sigma(1 + d\varepsilon) \quad (3.12)$$

The question is now if that section has actually become stronger or weaker. If the section has become stronger, meaning that a force larger than F is required to elongate it more, it will not deform any further, but another part of the specimen will start to deform instead; the deformation is stable and no necking will occur. This depends on the change in yield stress, the stress required to deform that part any further. This new yield stress can be expressed as:

$$\sigma_{yield,new} = \sigma + d\sigma = \sigma + \frac{d\sigma}{d\varepsilon} d\varepsilon = \sigma \left(1 + \frac{1}{\sigma} \frac{d\sigma}{d\varepsilon} d\varepsilon \right) \quad (3.13)$$

One can now state that no instability will arise, and necking will not occur, if the new yield stress of the section expressed by (3.13) has become larger than the actual acting stress expressed by (3.12), this finally yields:

$$\frac{1}{\sigma} \frac{d\sigma}{d\varepsilon} > 1, \text{ or: } \frac{d\sigma}{d\varepsilon} > \sigma \quad (3.14)$$

So the diffuse necking occurs when:

$$\frac{d\sigma}{d\varepsilon} = \sigma \quad (3.15)$$

The Local necking is defined by Hill's local necking criterion [38], a local neck means that there is no elongation along the neck, only across the neck. In that case we can ignore any changes in width of the specimen and apply the same analysis on a piece of unit width, so $A = 1, t = t$. This yield:

$$dF = 0 = d(\sigma_1 t) = d\sigma_1 t + \sigma_1 dt \quad (3.16)$$

$$\frac{d\sigma_1}{\sigma_1} = -\frac{dt}{t} = -d\varepsilon_3 \quad (3.17)$$

Or:

$$\frac{d\sigma_1}{d\varepsilon_3} = -\sigma_1 \quad (3.18)$$

This is known as Hill's local necking criterion. In a more general situation we have defined the strain rate state by a constant β defined as: $\varepsilon_2 = \beta\varepsilon_1$ and consequently: $\varepsilon_3 = -(1 + \beta)\varepsilon_1$ as $\varepsilon_1 + \varepsilon_2 + \varepsilon_3 = 0$. We can rewrite (3.18) as:

$$\frac{d\sigma_1}{d\varepsilon_1} = (1 + \beta)\sigma_1 \quad (3.19)$$

In the tensile test, $\beta = -\frac{1}{2}$, and the criterion for local necking occurs when [20]:

$$\frac{d\sigma}{d\varepsilon} = \frac{\sigma}{2} \quad (3.20)$$

Diffuse and localized necking point computed for the two models are quite different (Table 9), this can cause big discrepancies in simulations involving the post-necking region of the material. The TCM model is useful because of its relationship with Vickers hardness, but it needs to be improved with a contribution of the Swift law to obtain a combined Swift-Voce model which will have plastic region coherent to what observed by K. Pack and S. J. Marcadet.

	ε_D	ε_L
Marcadet CSV	0,0374	0,0772
TCM	0,0261	0,0311

Table 9: ε_D and ε_L computed for CSV ad TCM model

3.1.3 Enhanced Tailored Crash Model

This section concerns the development of a new model for the calibration of press-hardened boron steels, which is an upgrade of the Tailored Crash Model introduced by A. Bardelcik. The procedure is similar to the one used in the chapter 2, the first step was an interpolation to find the missing parameters of the Combined Swift-Voce constitutive equation, then the post-necking region was obtained by extrapolation. In the chapter 2 experimental data were used for interpolation, for boron steels there are no such data and some assumptions are needed to find the Swift law (3.21) parameters for the combined Swift-Voce hardening law.

The first assumption is that flow curves calculated with the Tailored Crash Model are not too different from real curves at least up to necking as shown in Fig. 31b. The second assumption is that the difference between diffuse necking point computed with (3.15) using the TCM model as hardening curves and the real diffuse necking point is small. With these assumptions is possible to consider curves obtained with the TCM model almost equals to real tensile test curves up to necking and interpolate a Swift law with their points. Applying this procedure for different values of Vickers hardness is possible to obtain Swift law parameters as function of HV.

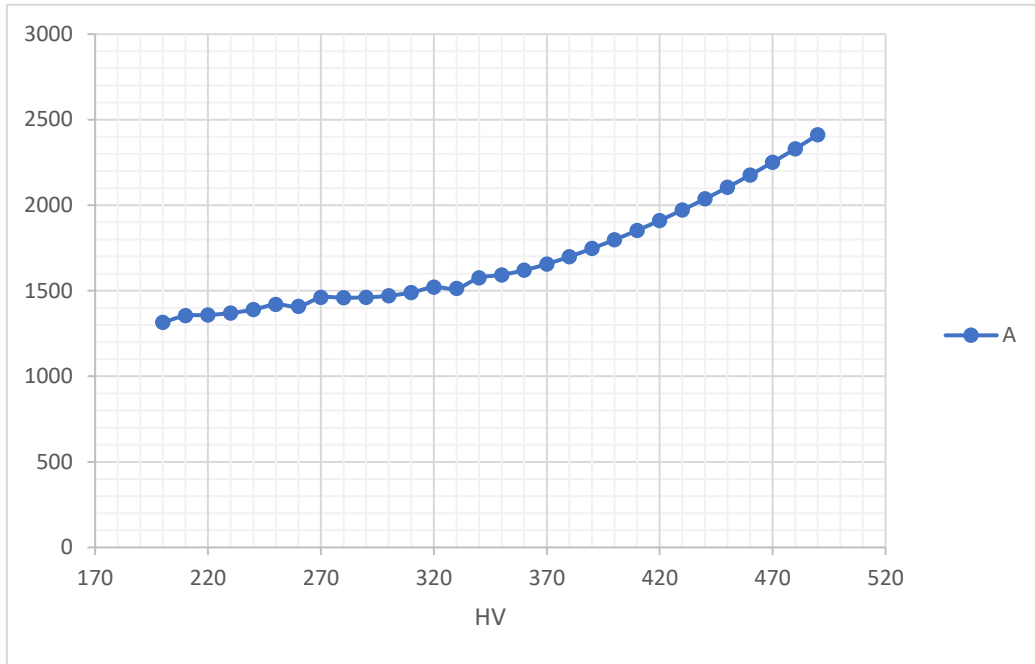


Figure 34: "A" as function of HV

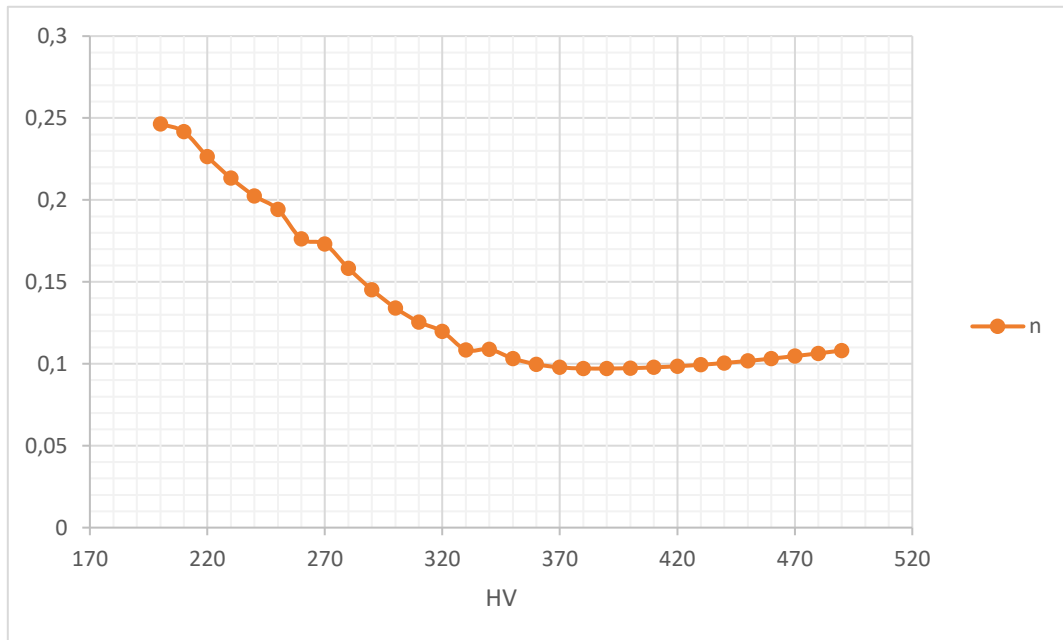


Figure 35: "n" as function of HV

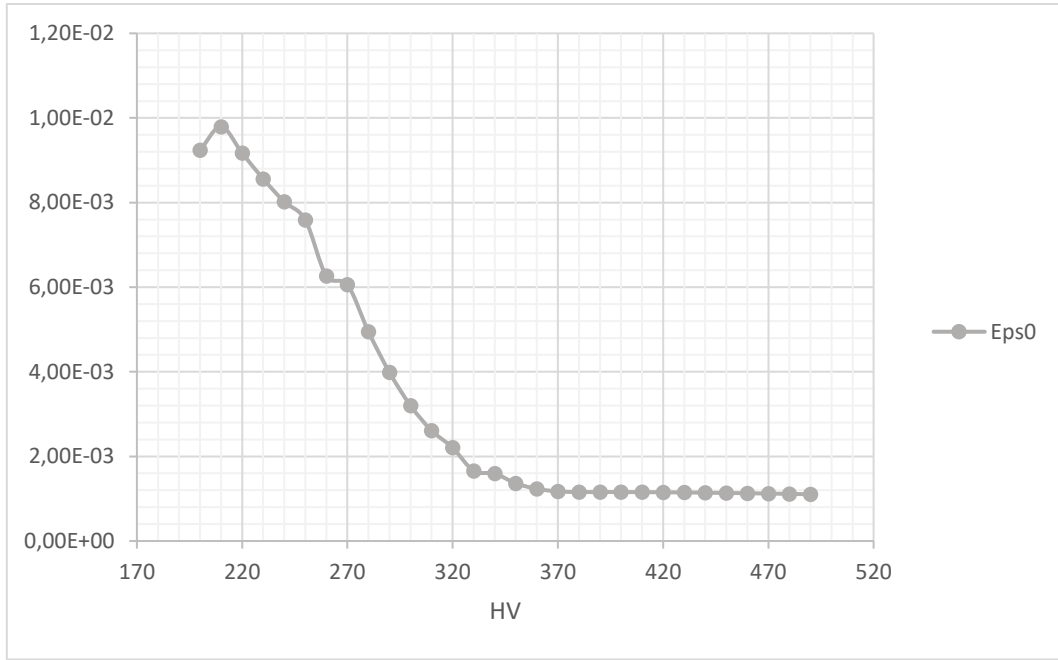


Figure 36: "Eps0" as function of HV

$$\sigma_s[\bar{\varepsilon}_p] = A(\bar{\varepsilon}_p + \varepsilon_0)^n \quad (3.21)$$

$$A(HV) = A_2 HV^2 + A_1 HV + A_0 \quad (3.22)$$

$$\varepsilon_{0HV < 370} = \varepsilon_{02} HV^2 + \varepsilon_{01} HV + \varepsilon_{00} \quad (3.23)$$

$$\varepsilon_{0HV > 370} = \varepsilon_{01}^* HV + \varepsilon_{00}^* \quad (3.24)$$

$$n = n_2 HV^2 + n_1 HV + n_0 \quad (3.25)$$

$A(HV)$	$A_2 = 1.4091 \times 10^{-2}$	$A_1 = -6.2544$	$A_0 = 2066.1$
$\varepsilon_{0_{HV < 370}}(HV)$	$\varepsilon_{0_2} = 1.7434 \times 10^{-7}$	$\varepsilon_{0_1} = -1.5682 \times 10^{-4}$	$\varepsilon_{0_0} = 3.5022 \times 10^{-2}$
$\varepsilon_{0_{HV > 370}}(HV)$	-	$\varepsilon_{0_1}^* = -4.8716 \times 10^{-7}$	$\varepsilon_{0_0}^* = 1.3515 \cdot 10^{-3}$
$n(HV)$	$n_2 = 3.5672 \cdot 10^{-6}$	$n_1 = -2.9656 \times 10^{-3}$	$n_0 = 0.7083$

Table 10: Constant parameters for equations (3.22)-(3.25)

These parameters can be used in the CSV constitutive equation (3.26) to complete the TCM model, the weighting parameter “ α ”, can be fixed equals to 0.3 for coherence with K. Pack and S. J. Marcadet calibration [36] , this means that the Swift law contribution will be the 30% in the final hardening law, obviously this is an assumption, is likely that α won't change too much with HV, anyway this can be a starting point for future optimizations of the model to achieve an higher accuracy.

$$\sigma[\bar{\varepsilon}_p] = \alpha \cdot \sigma_s[\bar{\varepsilon}_p] + (1 - \alpha) \cdot \sigma_v[\bar{\varepsilon}_p] \quad (3.26)$$

As shown in Fig.36, the Enhanced Tailored Crash Model give a full martensitic steel flow curve (HV 480) very similar to the one obtained by K. Pack and S. J. Marcadet. It is possible to verify the accuracy of the model computing the diffuse necking point and the localized necking point.

	ϵ_D	ϵ_L
Marcadet CSV	0,0374	0,0772
Modified TCM	0,0375	0,0682

Table 11: Diffuse and localized necking plastic strain comparison

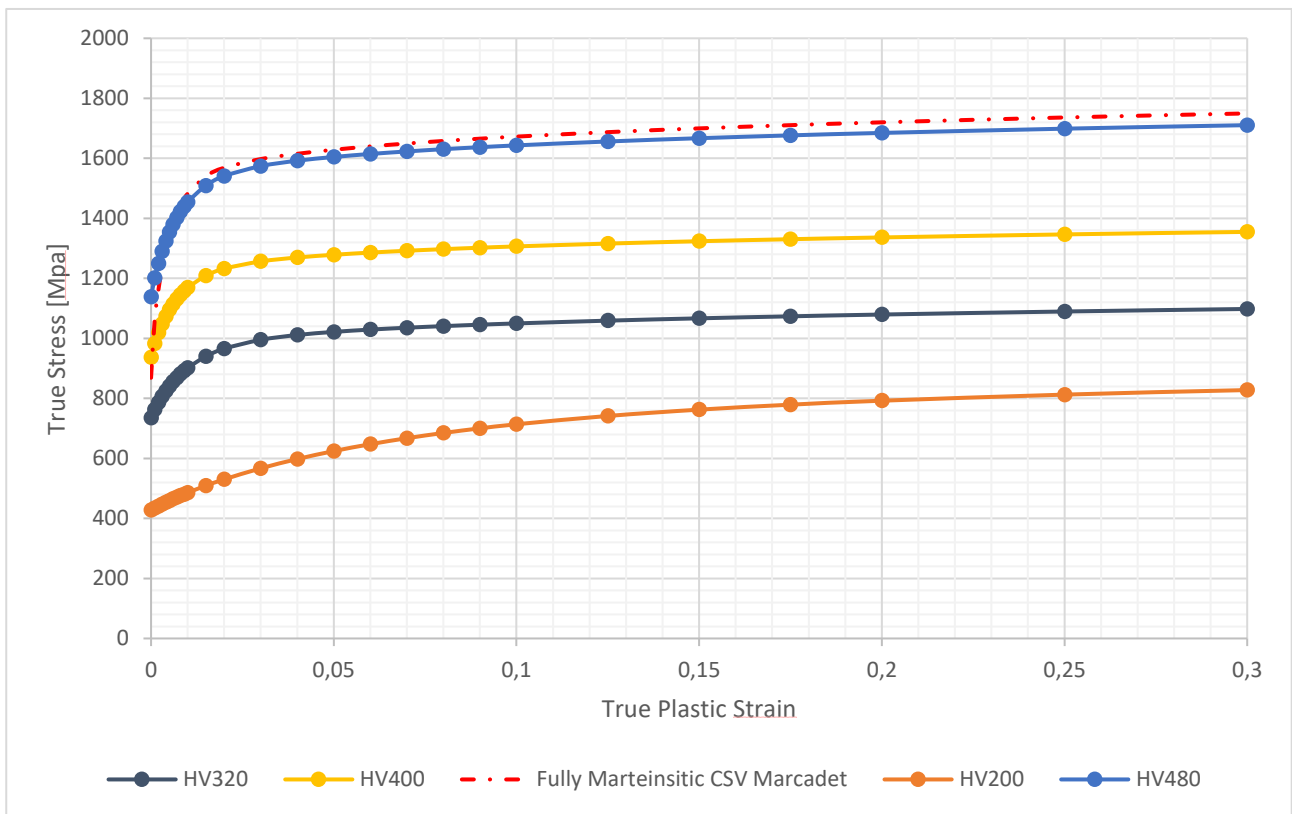


Figure 37: Combined Swift-Voce hardening model for HV 480, 400, 320, 200

3.2 Diffuse and Localized Necking laws

As discussed in a section 3.1.2, Hill's criterion and Considere's criterion can be used to determine diffuse and localized necking strain. With equation (3.15) and (3.20) these characteristic points have been calculated for flow curves between HV 200 and HV 480 spaced by 10 units; then interpolated with polynomial laws as function of Vickers hardness.

This step is not strictly necessary for the model, but it is convenient because it's possible to use the following laws to obtain ε_D and ε_L without using (5.15) and (5.20); in other words with these equations, for a given HV value, is possible to have the flow curve and ε_D and ε_L . In the following sections, similar relations will be calculated also for fracture criterion; the purpose is to build a tool for martensitic steels which shows all the information needed by changing the HV input value.

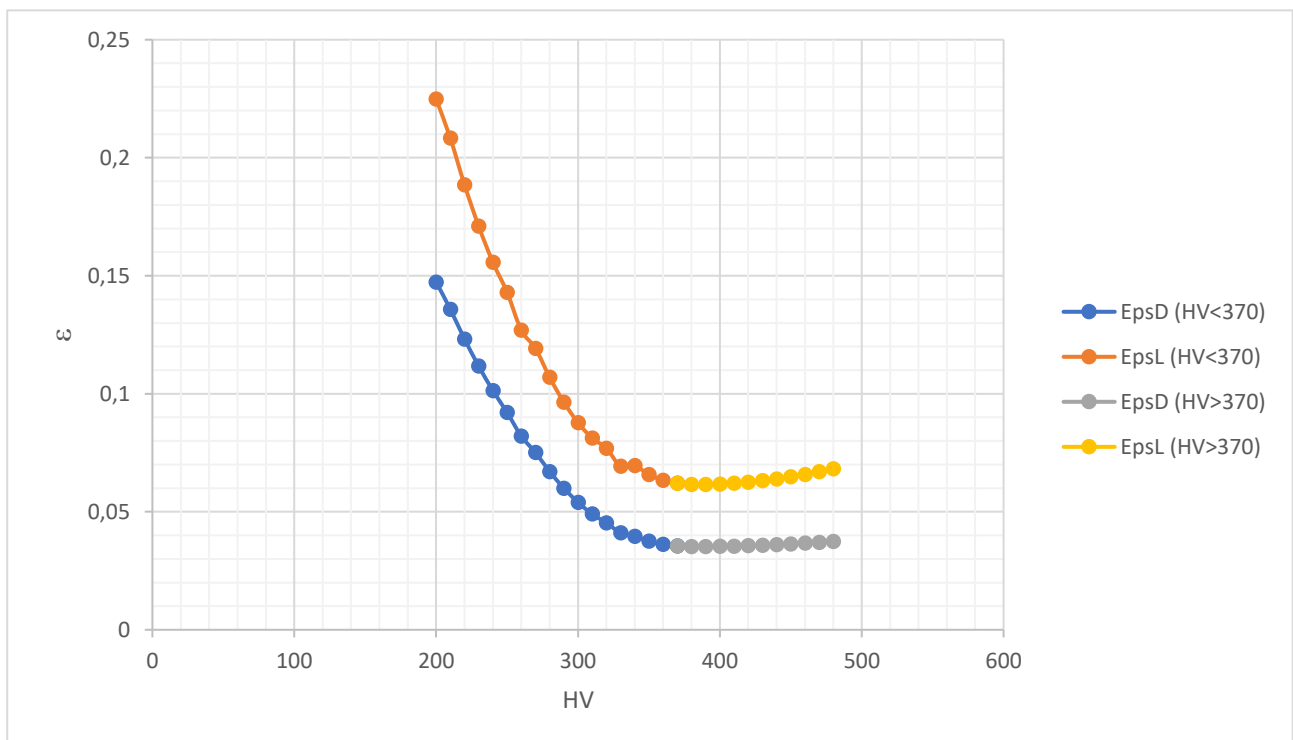


Figure 38: ε_D and ε_L as function of HV

$$\varepsilon_{L_{HV<370}}(HV) = \varepsilon_{L_1}HV^3 + \varepsilon_{L_2}HV^2 + \varepsilon_{L_3}HV + \varepsilon_{L_4} \quad (3.27)$$

$$\varepsilon_{L_{HV>370}}(HV) = \varepsilon_{L_5}HV^2 + \varepsilon_{L_6}HV + \varepsilon_{L_7} \quad (3.28)$$

$$\varepsilon_{D_{HV<370}}(HV) = \varepsilon_{D_1}HV^3 + \varepsilon_{D_2}HV^2 + \varepsilon_{D_3}HV + \varepsilon_{D_4} \quad (3.29)$$

$$\varepsilon_{D_{HV>370}}(HV) = \varepsilon_{D_5}HV^2 + \varepsilon_{D_6}HV + \varepsilon_{D_7} \quad (3.30)$$

$\varepsilon_{L_{HV<370}}(HV)$	$\varepsilon_{L_1} = -3,0811 \times 10^{-9}$	$\varepsilon_{L_2} = 8,5545 \times 10^{-6}$	$\varepsilon_{L_3} = -5,0628 \times 10^{-3}$	$\varepsilon_{L_4} = 9,2104 \times 10^{-1}$
$\varepsilon_{L_{HV>370}}(HV)$	$\varepsilon_{L_5} = 7,4513 \times 10^{-7}$	$\varepsilon_{L_6} = -5,7497 \times 10^{-4}$	$\varepsilon_{L_7} = 1,7261 \times 10^{-1}$	
$\varepsilon_{D_{HV<370}}(HV)$	$\varepsilon_{D_1} = 1,2270 \times 10^{-9}$	$\varepsilon_{D_2} = 2,8328 \times 10^{-6}$	$\varepsilon_{D_3} = -2,5931 \times 10^{-3}$	$\varepsilon_{D_4} = 5,4293 \times 10^{-1}$
$\varepsilon_{D_{HV>370}}(HV)$	$\varepsilon_{D_5} = 2,5379 \times 10^{-7}$	$\varepsilon_{D_6} = -1,9671 \times 10^{-4}$	$\varepsilon_{D_7} = 7,3470 \times 10^{-2}$	

Table 12: ε_D and ε_L parameters for equations (3.27) -(3.30)

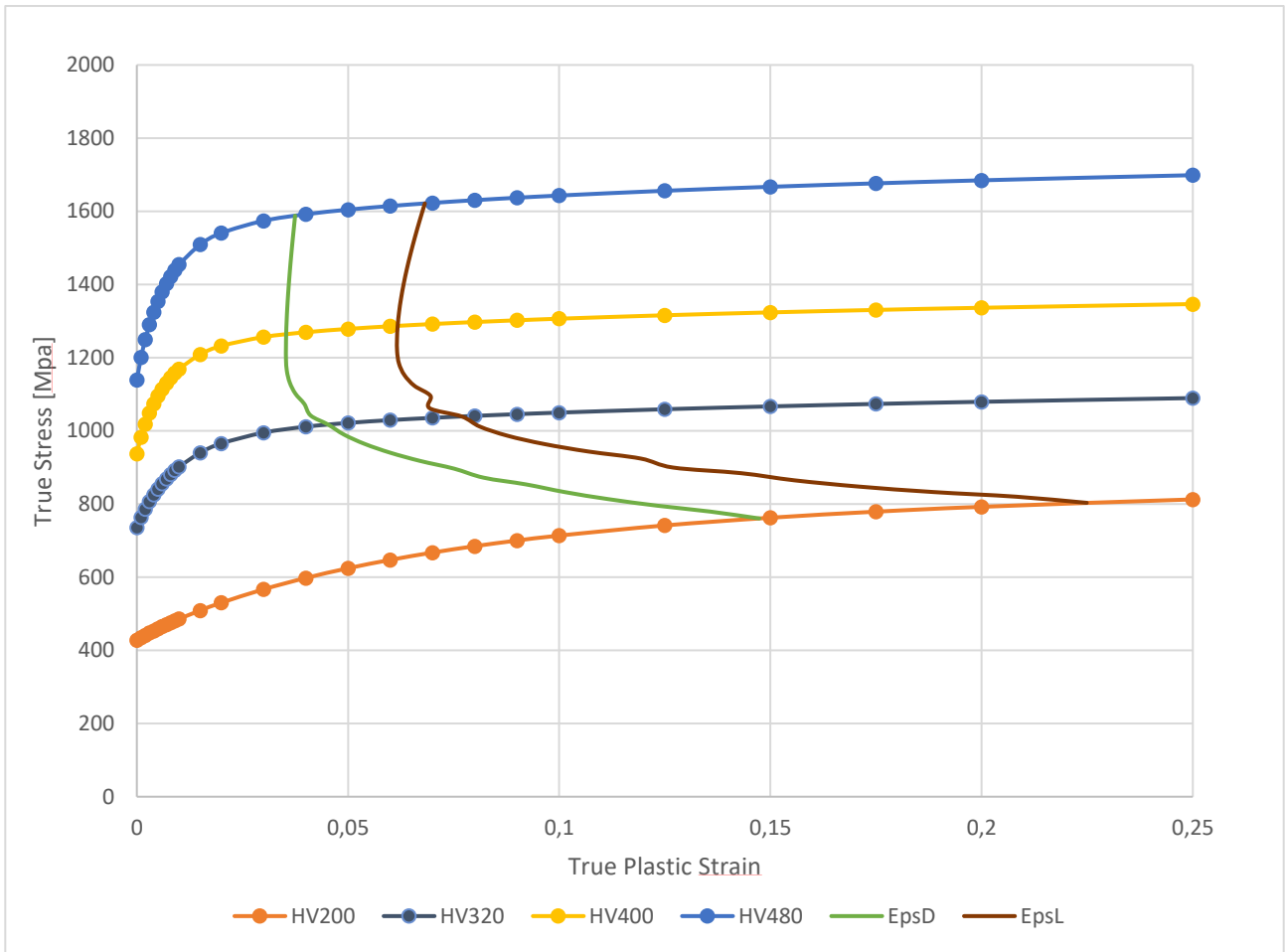


Figure 39: EpsD and EpsL position for different HV in the True Plastic Strain-True Stress plane

3.3 Modified Mohr-Coulomb for Martensitic Steels

As discussed in section 1.6.1, Modified Mohr-Coulomb model (mMC) can be used as fracture criterion to predict fractures in non-plane stress condition. The complete equation for the equivalent failure plastic strain $\bar{\epsilon}_f$ is:

$$\bar{\epsilon}_f(\eta, \bar{\theta}) = \left\{ \frac{k}{c_2} \left[c_3 + (c_4 - c_3) \frac{\sqrt{3}}{2 - \sqrt{3}} \left(\sec\left(\frac{\pi}{6} \bar{\theta}\right) - 1 \right) \right] \left[\sqrt{\frac{1 + c_1^2}{3}} \cos\left(\frac{\pi}{6} \bar{\theta}\right) + c_1 \left(\eta + \frac{1}{3} \sin\left(\frac{\pi}{6} \bar{\theta}\right) \right) \right] \right\} \quad (3.31)$$

- η is the stress triaxiality
- $\bar{\theta}$ is the normalized lode angle parameter
- k, n are material parameters from strain hardening
- c_1, c_2, c_3, c_4 are material parameters from fracture experiment

η and $\bar{\theta}$ are independent parameters, k and n came from the modified TCM model while c_1, c_2, c_3, c_4 must be determined with tests on materials. c_4 usually is approximately equals to 1, it modifies the curve only around $\eta = 0.67$ and in this zone the HSR criterium for fracture is more important as discussed in the following sections. For this reason, c_4 has been fixed equals to 1.

Lukas ten Kortenaar in his thesis [39] characterized the failure behaviour of hot stamped USIBOR®1500-AS steel sheet with tailored properties. Failure strain has been characterized as a function of stress state investigating a range of material quench conditions. Six different material quench conditions were considered, ranging from fully martensitic (485 HV) to a mixed ferrite-bainite microstructure (185 HV). Miniature shear, butterfly, hole expansion, hole tensile and hemispherical dome tests were developed for fracture characterization of sheet metal, considering fracture strain to be a function of stress state and assuming the material to be isotropic and von Mises yielding, the equivalent strain at fracture and stress triaxiality of each experiment was determined.

For the purpose of this work, only tests concerning fully bainitic, fully martensitic and intermediate quench have been considered. The fully bainitic microstructure was produced by austenizing blanks in a furnace to 930 °C, holding at this temperature for 6.5 minutes, and then removing it from the furnace, allowing it to cool in still air, with a resulting microhardness of 232 HV. Fully martensitic blanks followed the same austenization process, however the blanks were transferred to still oil in order to quench them, they showed a microhardness of 486 HV. The intermediate microstructure has been produced with a forced air quench calibrated to have a microhardness of 386 HV.

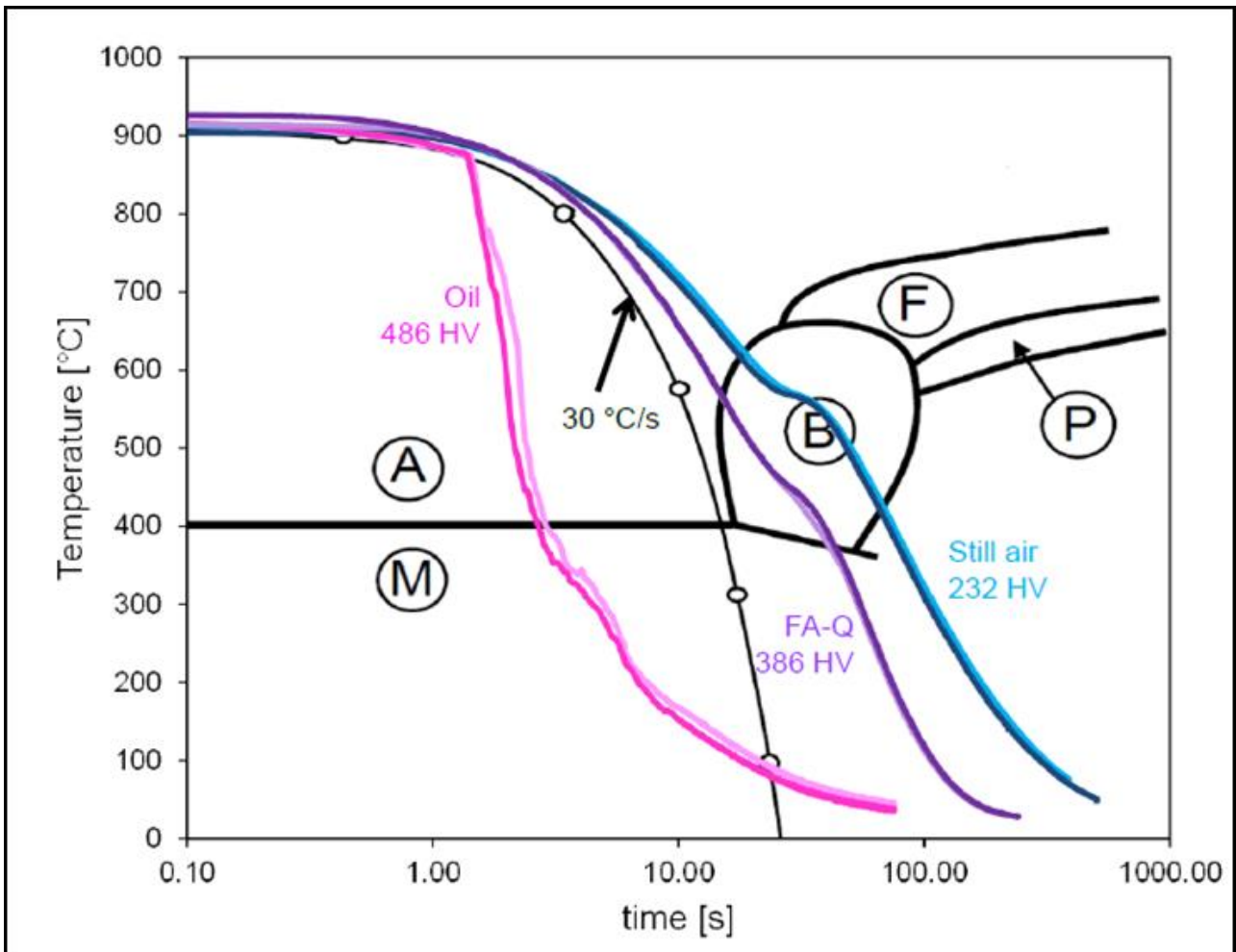


Figure 40: CCT for USIBOR® 1500-AS. Three quench conditions overlaid on the CCT correspond to the fully martensitic, intermediate forced air quench, and fully bainitic, denoted by magenta, purple, and blue. The critical cooling rate of 30 °C/s to obtain a fully martensitic microstructure is also shown. [39]

The results of the measurement campaign carry out by Lukas ten Kortenaar used in this work are presented in the following tables:

<i>HV232</i>	<i>Averaged Triaxiality</i>	<i>Equivalent Failure Plastic Strain</i>
<i>Butterfly Tensile Test 0°</i>	0,005	0,9
<i>Butterfly Tensile Test 10°</i>	0,064	0,77
<i>Butterfly Tensile Test 30°</i>	0,187	0,74
<i>Uniaxial Tensile Test</i>	0,37	0,81
<i>4a Notched Tensile Test</i>	0,46	0,46
<i>1a Notched Tensile Test</i>	0,58	0,52
<i>Equi-biaxial Dome Test</i>	0,67	0,76

Table 13: Test results for HV 232 equivalent failure plastic strain versus averaged triaxiality

<i>HV386</i>	<i>Averaged Triaxiality</i>	<i>Equivalent Failure Plastic Strain</i>
<i>Butterfly Tensile Test 0°</i>	0,013	0,68
<i>Butterfly Tensile Test 10°</i>	0,059	0,64
<i>Butterfly Tensile Test 30°</i>	0,176	0,46

<i>Uniaxial Tensile Test</i>	0,4	0,61
<i>4a Notched Tensile Test</i>	0,51	0,48
<i>1a Notched Tensile Test</i>	0,6	0,42
<i>Equi-biaxial Dome Test</i>	0,65	0,3

Table 14: Tests results for HV 386, equivalent failure plastic strain versus averaged triaxiality [39]

<i>HV485</i>	<i>Averaged Triaxiality</i>	<i>Equivalent Failure Plastic Strain</i>
<i>Butterfly Tensile Test 0°</i>	0,028	0,54
<i>Butterfly Tensile Test 10°</i>	0,04	0,52
<i>Butterfly Tensile Test 30°</i>	0,12	0,46
<i>Uniaxial Tensile Test</i>	0,41	0,72
<i>4a Notched Tensile Test</i>	0,54	0,4
<i>1a Notched Tensile Test</i>	0,59	0,35
<i>Equi-biaxial Dome Test</i>	0,67	0,35

Table 15: Tests results for HV 485, equivalent failure plastic strain versus averaged triaxiality [37]

These data represent specific points of the mMC curve in the plane triaxiality-equivalent failure plastic strain. Parameters c_1, c_2, c_3 of equation (3.31) can be found with an optimization process minimizing the least squared error between the result of (3.31) and the known data points of the tables. The parameters obtained for the three HV values are presented in the following table.

	c_1	c_2	c_3
HV 232	0,1510	0,7571	0,9898
HV 386	0,0761	0,8962	0,9148
HV 485	0,0918	1,1742	0,9049

Table 16: mMC material parameters for HV 232, HV 386 and HV 485

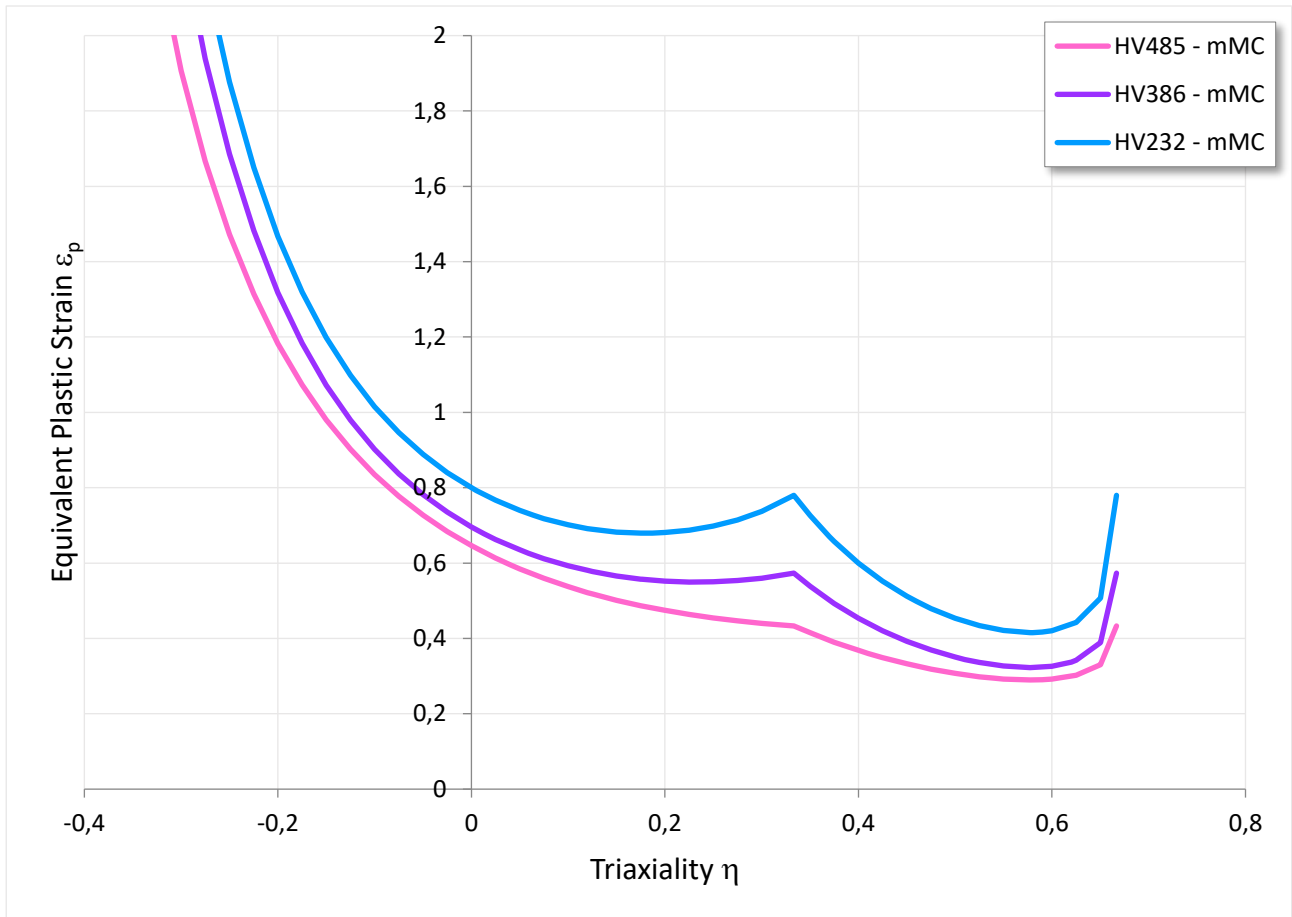


Figure 41: mMC Ductile Failure for HV 232, HV 386, HV 485

The points in Table 16 can be plotted as function of Vickers microhardness and interpolated with a polynomial function, in this way is possible to find a relation between mMC parameters and the microstructure of the steel and obtain the mMC curve for any given HV value.

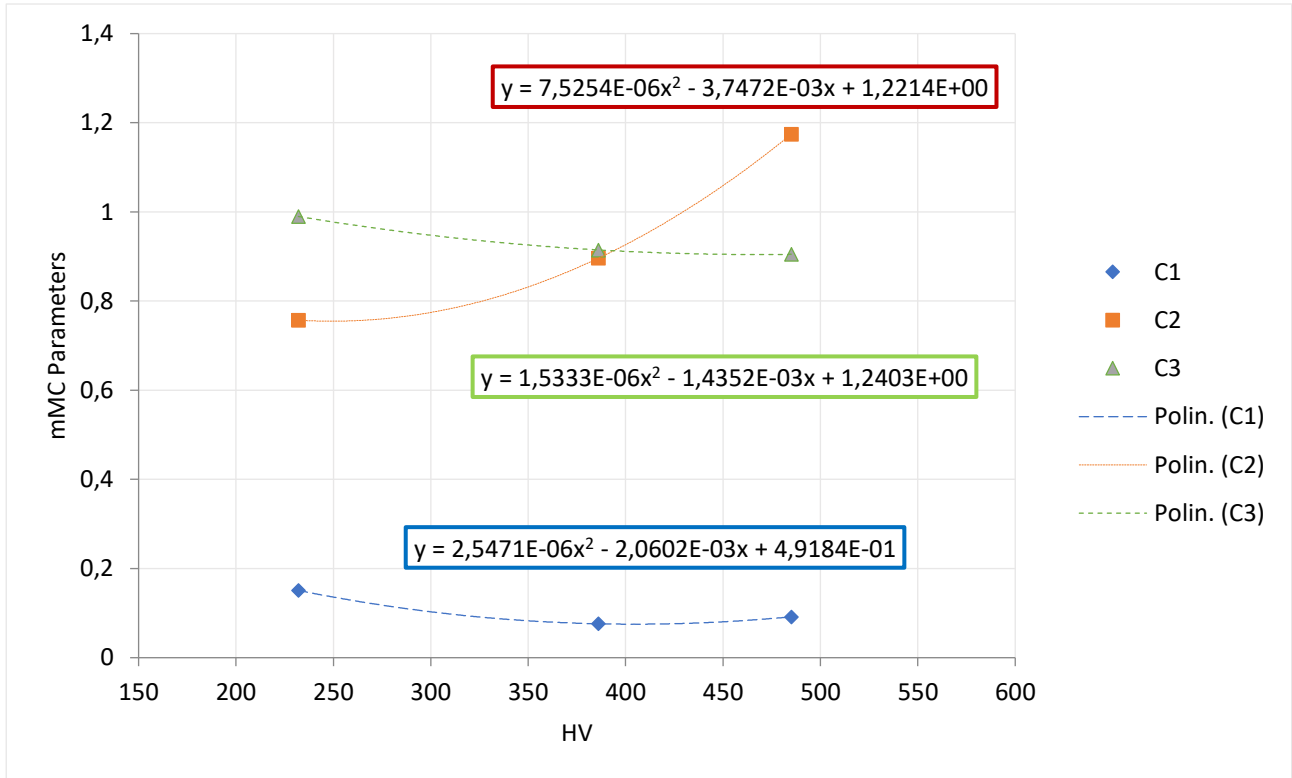


Figure 42: mMC Parameters versus Vickers Hardness

3.3.1 Enhanced Hill-Stören-Rice model parameter

The Enhanced Hill-Stören-Rice model (eHSR) is a modified version of the original HSR model discussed in section 1.5.2. It contains an additional parameter introduced to obtain the coincidence of eHSR and mMC when triaxiality is equals to 2/3. The equibiaxial tension stress state does not present necking before fracture so the two curves must coincide.

$$\varepsilon_{1n} = \begin{cases} \frac{n}{(1 + \alpha)}, & -1 < \alpha \leq 0 \\ \frac{3c\alpha^2 + n(2 + \alpha)^2}{2(2 + \alpha)(1 + \alpha + \alpha^2)}, & 0 < \alpha < 1 \end{cases} \quad (3.32)$$

$$\varepsilon_{1n} = \begin{cases} \frac{n}{(1 + \alpha)}, & -1 < \alpha \leq 0 \\ \frac{3c\alpha^2 + n(2 + \alpha)^2}{2(2 + \alpha)(1 + \alpha + \alpha^2)}, & 0 < \alpha < 1 \end{cases} \quad (3.33)$$

The original ε_{1n} - α FLD space obtained with 3.32 and 3.33 can be transformed into the space of equivalent plastic strain ratio over plastic strain ratio with:

$$\bar{\varepsilon}_n = \frac{2\sqrt{1+\alpha+\alpha^2}}{\sqrt{3}} \varepsilon_{1n} \quad (3.34)$$

α is related to triaxiality by:

$$\eta = \frac{1+\alpha}{\sqrt{3}\sqrt{1+\alpha+\alpha^2}} \quad (3.35)$$

To obtain the parameter an optimization process has been followed; when triaxiality “ η ” is equal to 2/3, equibiaxial tension stress state, the mMC plot and the eHSR plot must have the same value for equivalent plastic strain at failure, so the parameter has been found imposing the eHSR model to have the same result of mMC for each of the three different steels mentioned in the previous section. As additional step the three parameters have been plotted as function of Vickers hardness and interpolated with a linear relation to adapt eHSR model to any given HV value. The results of the optimization and the relation between c and HV are reported in the chart below.

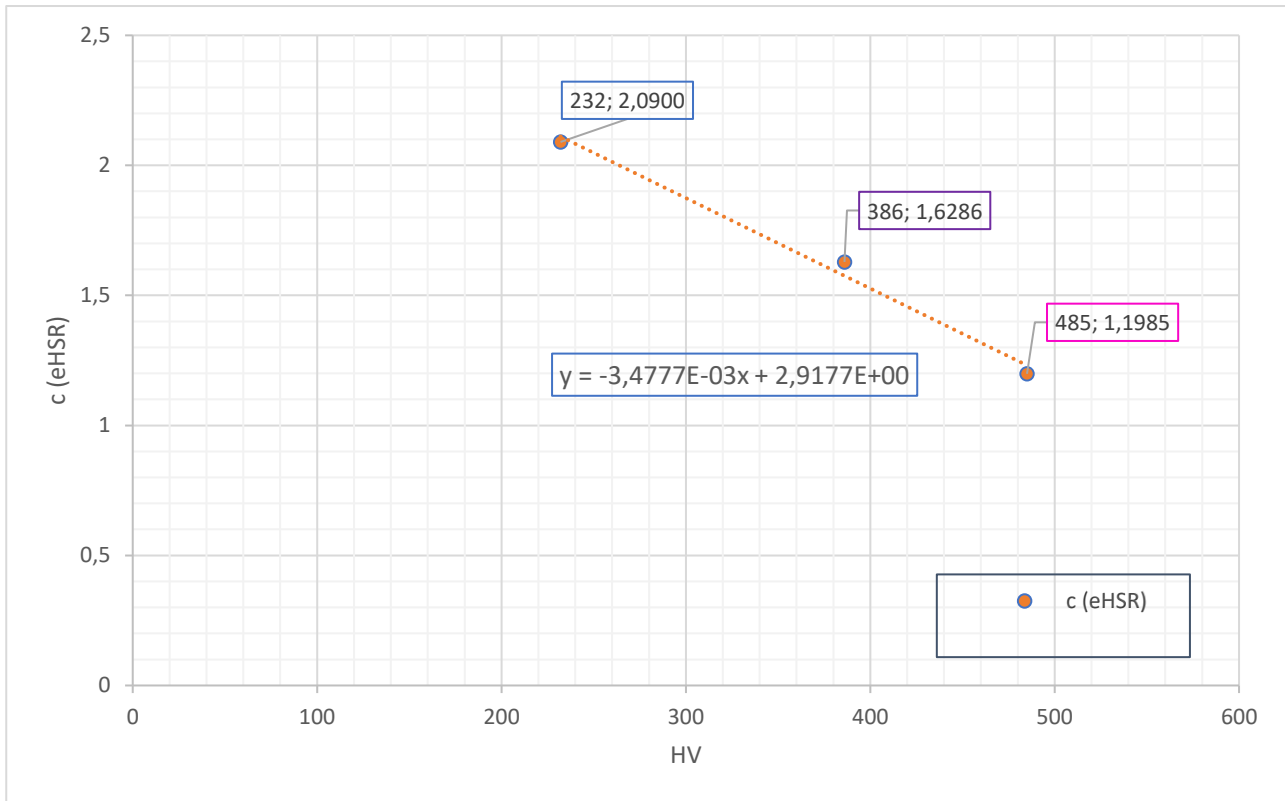


Figure 43: c (eHSR) as function of HV

eHSR and mMC curves are required as input when using material card MAT 127 for shell properties in PAMCRASH®. Basically, the software monitors the stress state of each elements through the triassiality and when the equivalent plastic strain reaches one of the two curves, the element fails. If the stress state is affected by necking it can't be predicted by mMC for a coarse mesh because the model is mesh dependent, so the element will fail when it reaches the equivalent plastic strain predicted by eHSR. On the opposite side pure shear is out of the domain of eHSR model and the relative element failure can be predicted by mMC since pure shear is not characterized by necking.

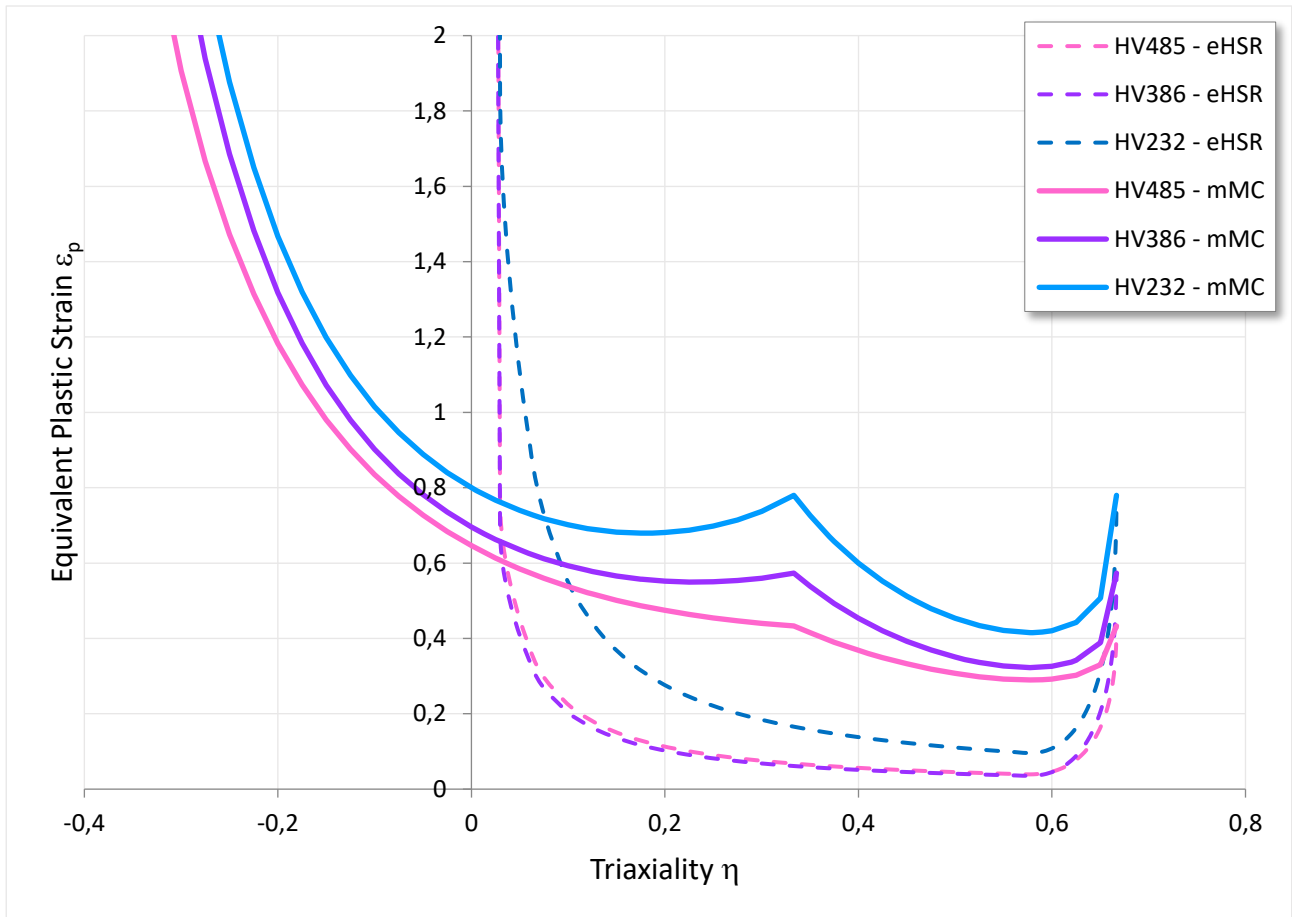


Figure 44: eHSR Instability and mMC Ductile Failure plot for HV 232, HV 386 and HV 458

4. Enhanced Tailored Crash Model Validation

This chapter is dedicated to the simulation performed in order to validate the enhanced Tailored Crash Model (eTCM). Materials characterized with the eTCM has been compared with the respective counterparts obtained with a model created by an original equipment manufacturer (OEM) based on the work of Eller and Greve [40] used in the automotive industry, this model will be called OEM model from hereinafter. The first simulation is a quasi-static four-point bending test on a hat section beam, the second is a side crash and the third a frontal crash. A coarse shell elements mesh has been applied to each finite element model. Some details of the simulations are omitted for confidentiality reasons.

4.1 Hat Test

The hat test is a four-point bending test with a hat section beam 700mm long and 200mm wide (Fig. 43). The test is quasistatic, and the displacement of the bender is time linear. The comparison between the two model, eTCM and the OEM, is outlined comparing the respective plot contact force vs displacement which is a measure of the energy absorbed by the structure. A good correlation between the two models is characterized by similar levels of contact force and displacement. The test has been performed for four type of quench hardened steel with Vickers Hardness respectively HV190, HV320, HV400, HV480. Each steel has been tested using the eTCM and the OEM model.

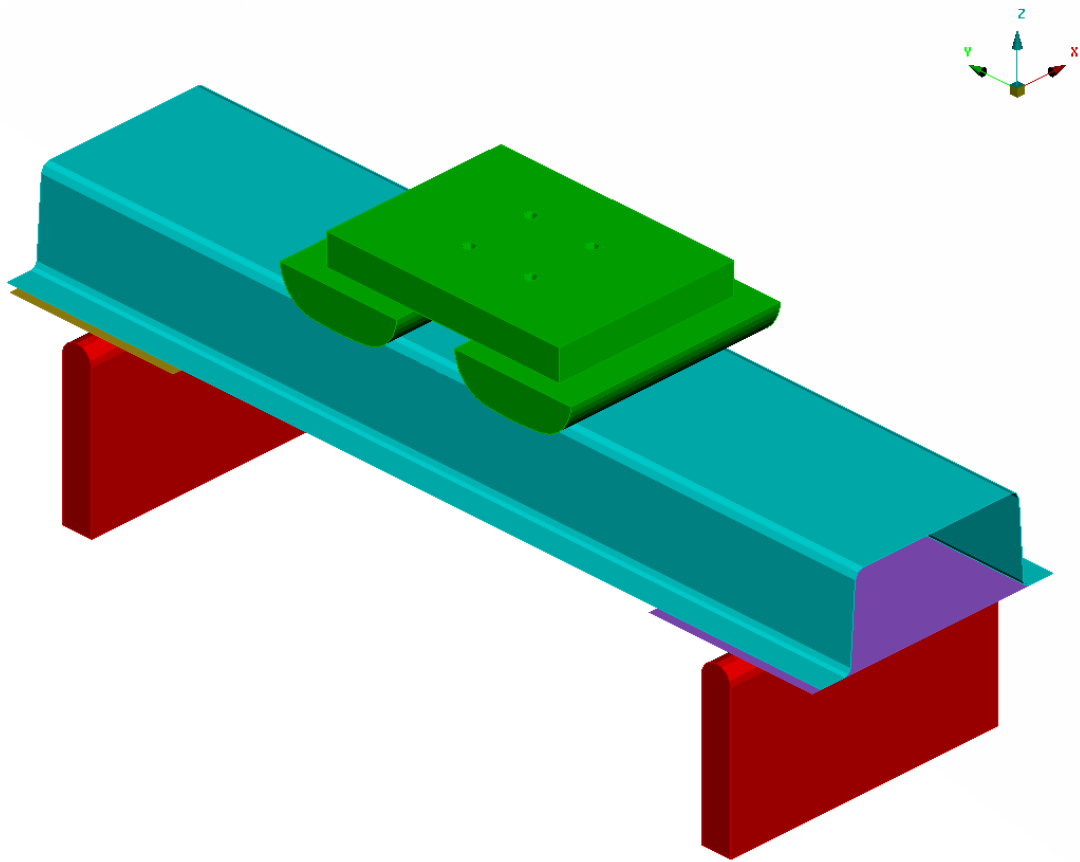


Figure 45: Hat test configuration

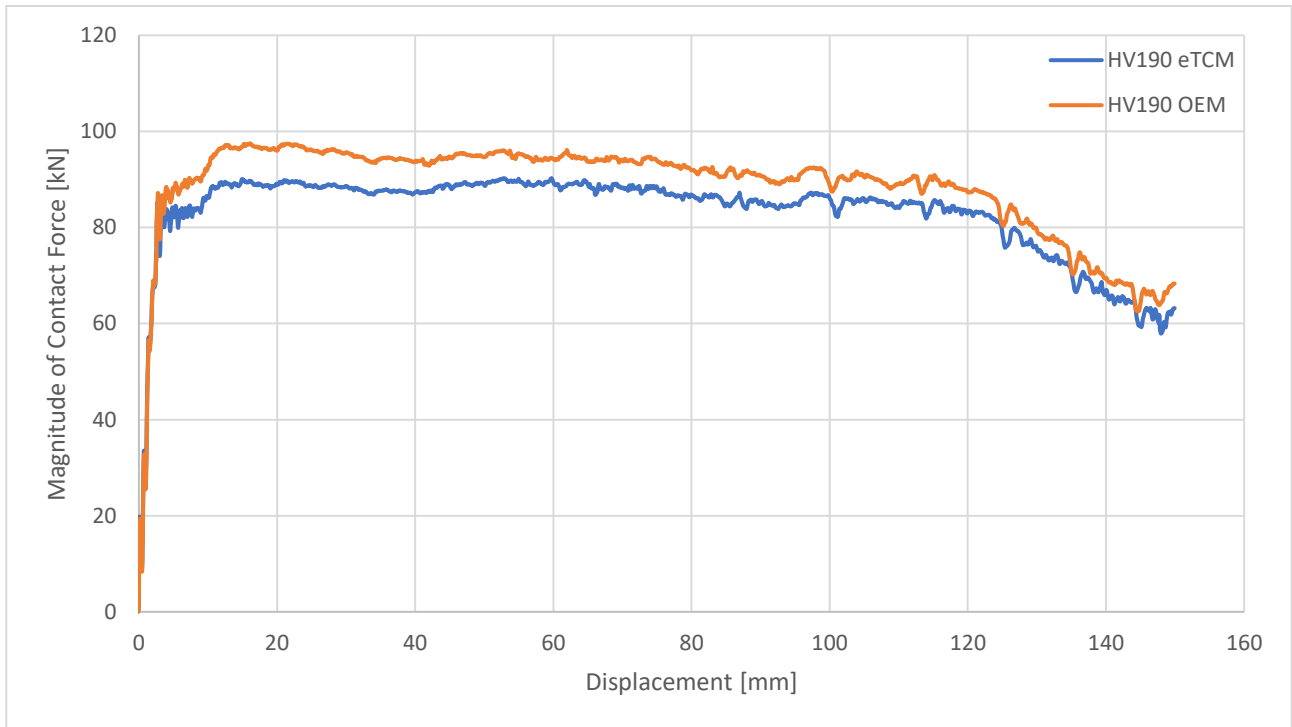


Figure 46: Contact Force vs Time for HV190 OEM and eTCM steel

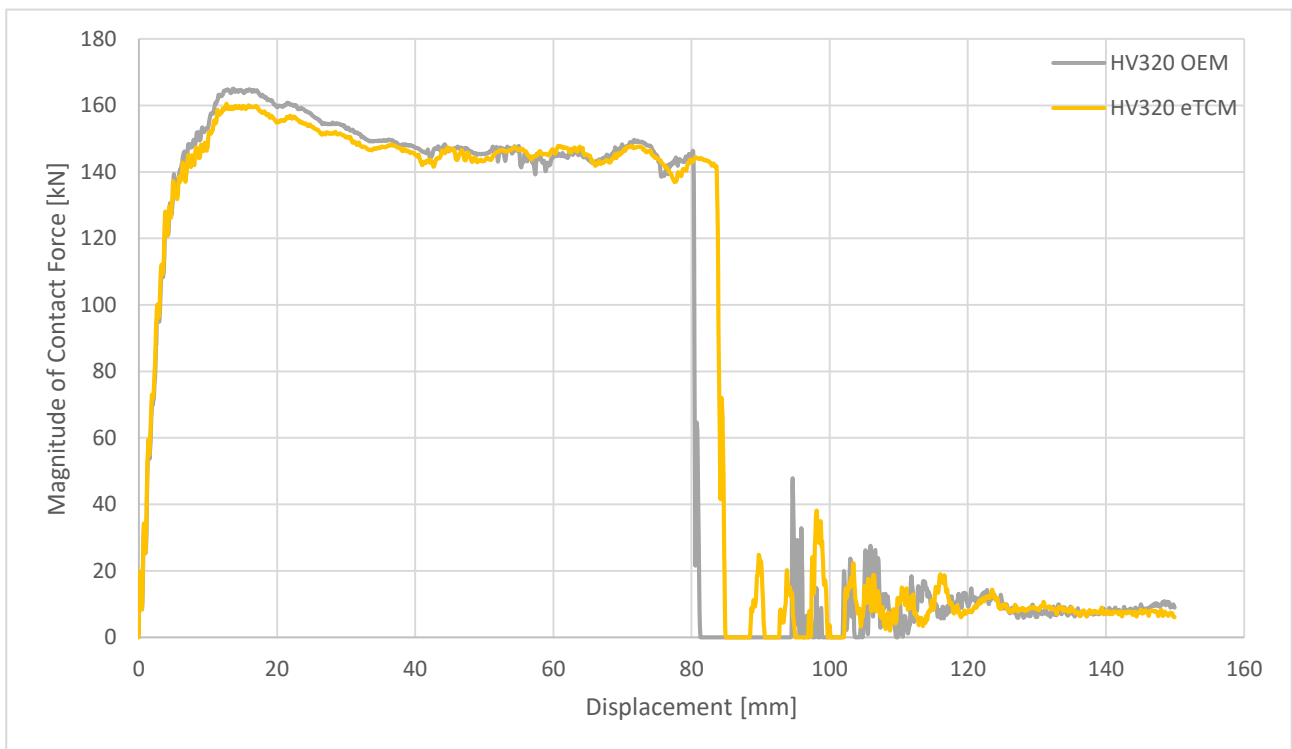


Figure 47: Contact Force vs Time for HV320 OEM and eTCM steel

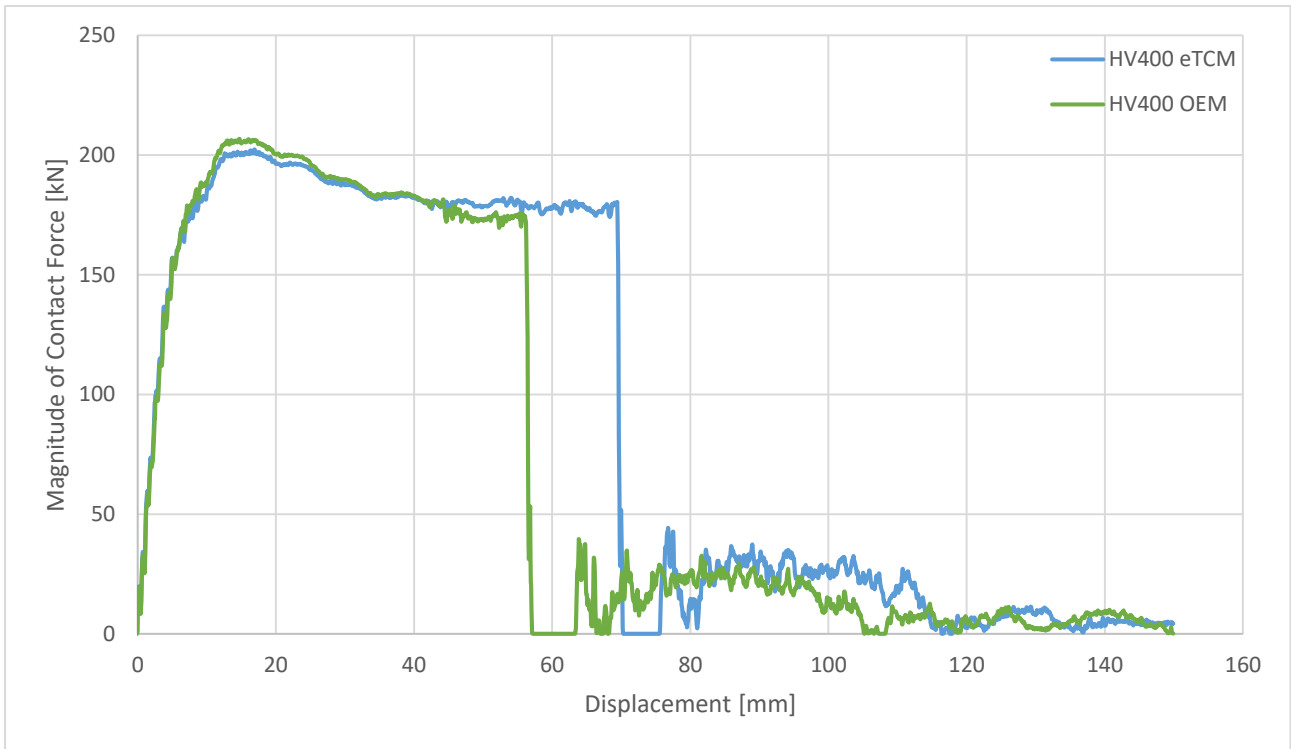


Figure 48: Contact Force vs Time for HV400 OEM and eTCM steel

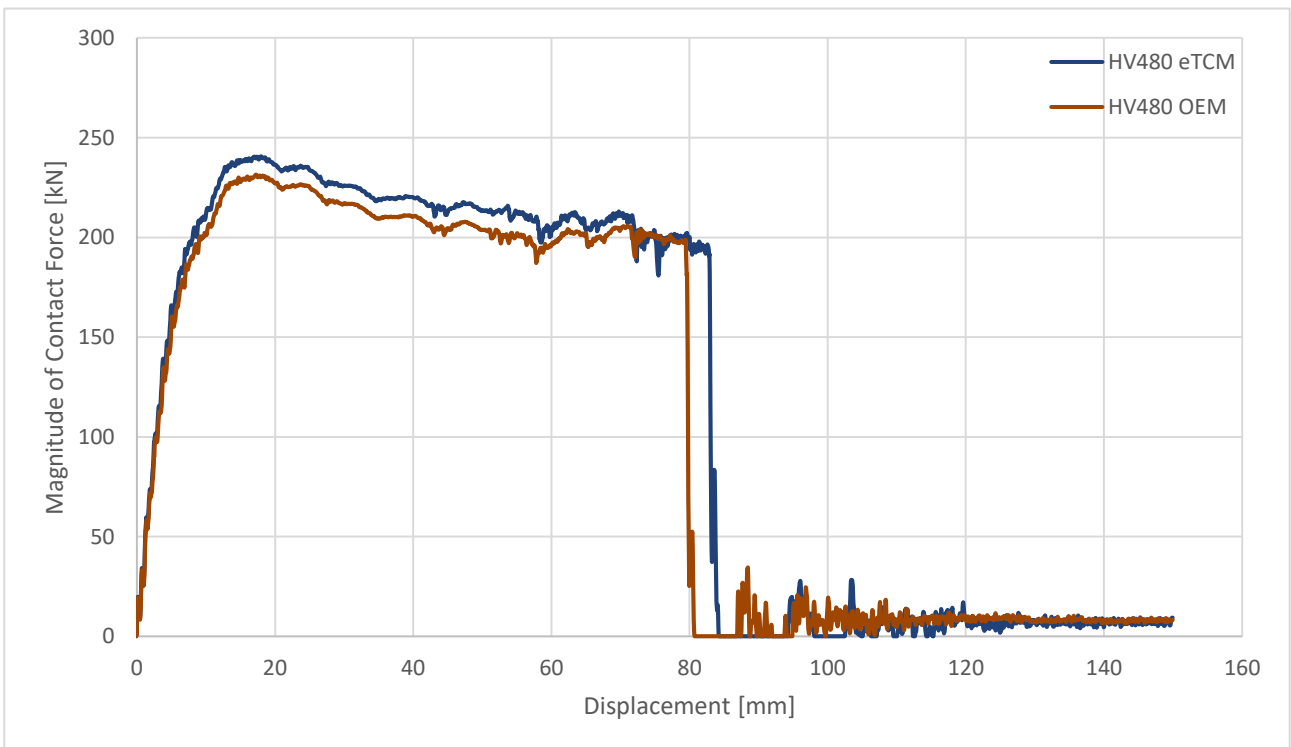


Figure 49: Contact Force vs Time for HV480 OEM and eTCM steel

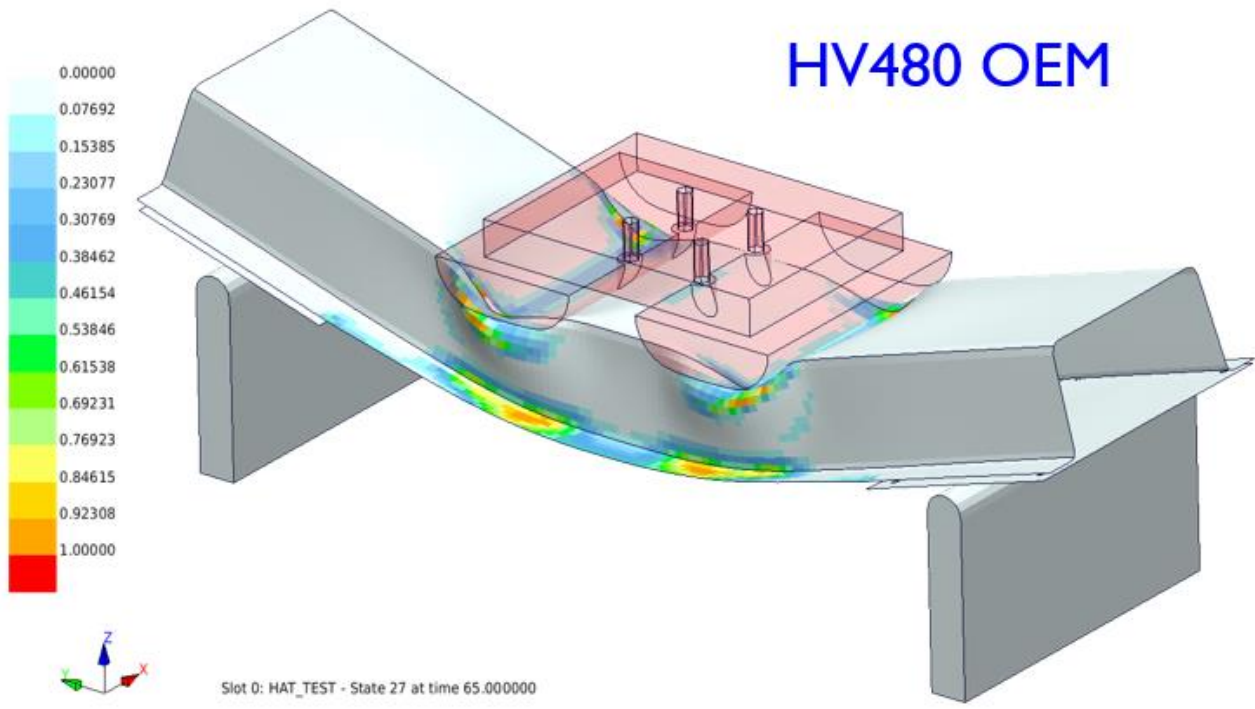
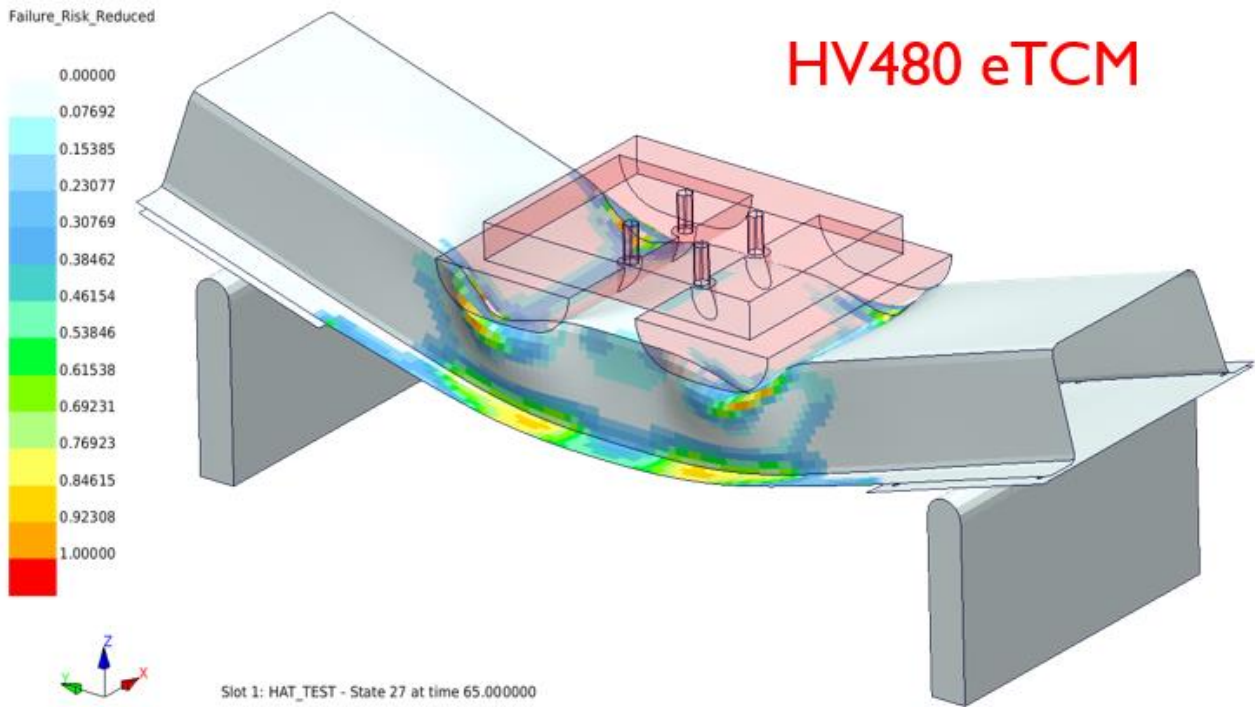


Figure 50: Failure Reduced Risk contour for HV480 eTCM and OEM

Each test showed a very good correlation with the OEM materials (Fig. 45, 46, 47, 48). HV400 steel characterized with the eTCM appears less conservative than the OEM one. Probably the weighting parameter α introduced in section 3.1.3 should not be fixed equals to 0.3 for each HV value but it has a dependency on HV. This dependency can be investigated through tensile tests of different quench level boron steel or best fitting of experimental data when available. Overall the result is representative and proof that eTCM can be used for crash simulations. In Fig. 49 the failure risk reduced calculated for both OEM and eTCM materials is displayed. This parameter indicate how far is the element from fracture, when it reaches “1” the element fails. As one can see the contour map for the different models is very similar and it highlight the same critical areas.

4.2 Side Crash

To assess the validity of the eTCM model a simulation of a side crash test has been performed. The results have been compared with a simulation ran with the OEM database. The reference regulation for the simulated side impact crash is the one released by the Insurance Institute for Highway Safety (IIHS) [41]. It is a regulation for non-mandatory ratings crash test known for having the most severe conditions among the ratings tests in the world.

Side impact crash tests consist of a stationary test vehicle struck on the driver side by a crash cart fitted with a deformable barrier element (Fig 51).

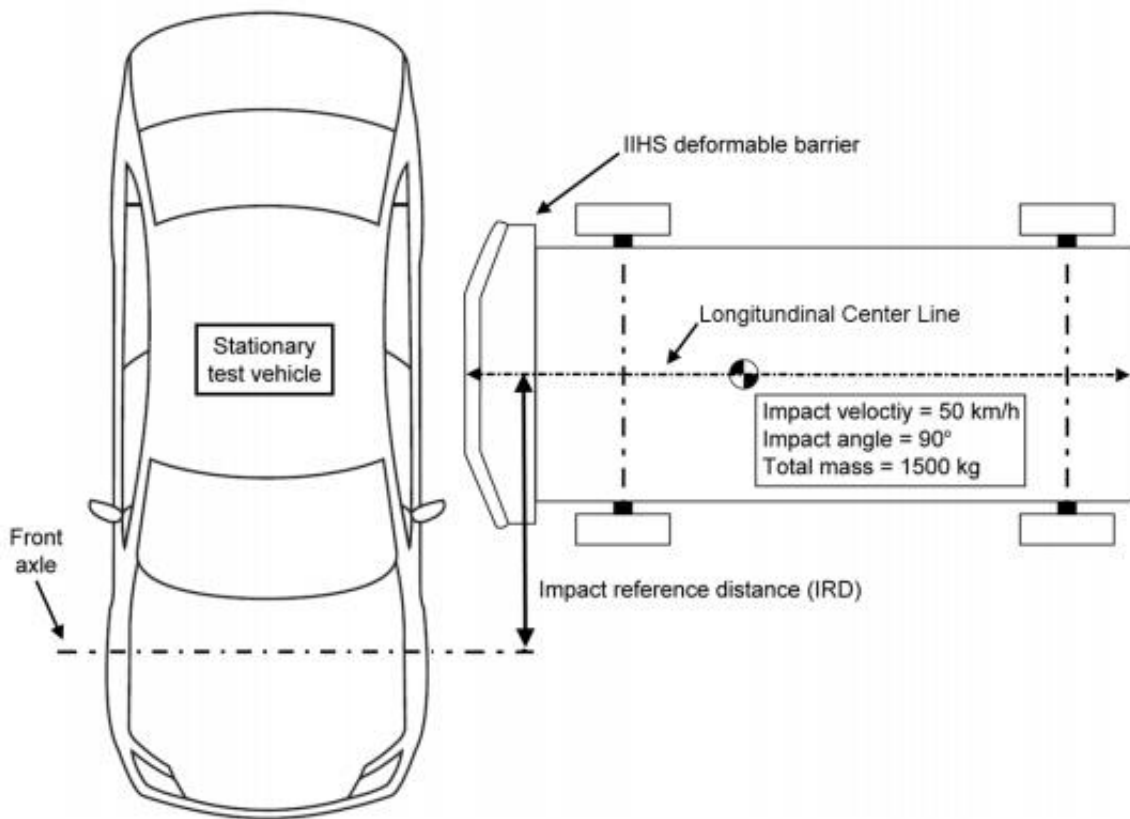


Figure 51: Moving deformable barrier alignment with test vehicle [41]

The 1,500 kg moving deformable barrier has an impact velocity of 50 km/h and strikes the vehicle on the driver side at 90-degree angle. Due to the high costs of these tests, a very accurate simulation campaign is recommended. This allow companies to predict the result of a crash test and to find the best design solutions to perform only one successful crash test.

The result of the simulations is very similar, and both the models highlighted the same critical areas of the body in white as shown in Fig. 52 and 53.

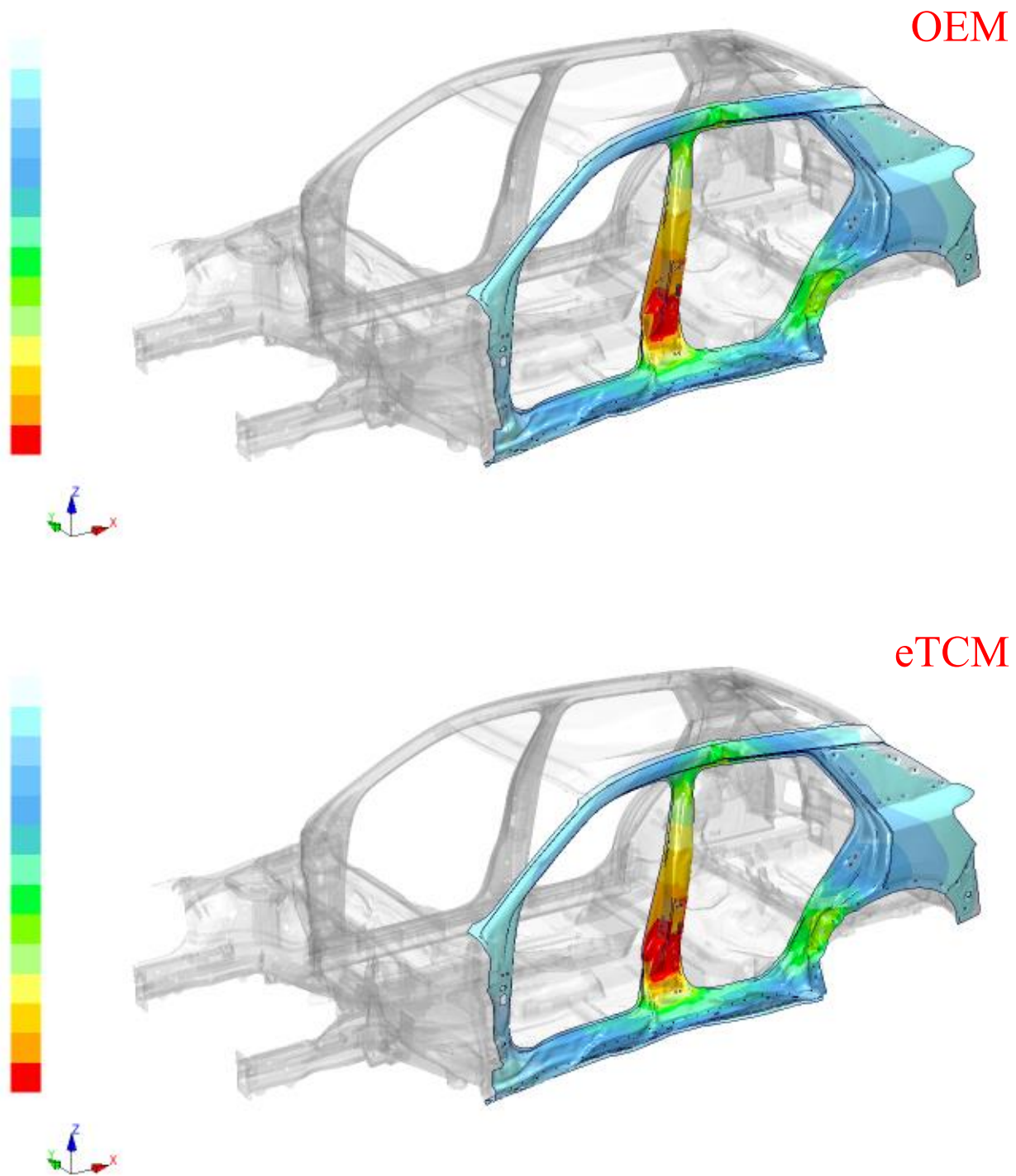
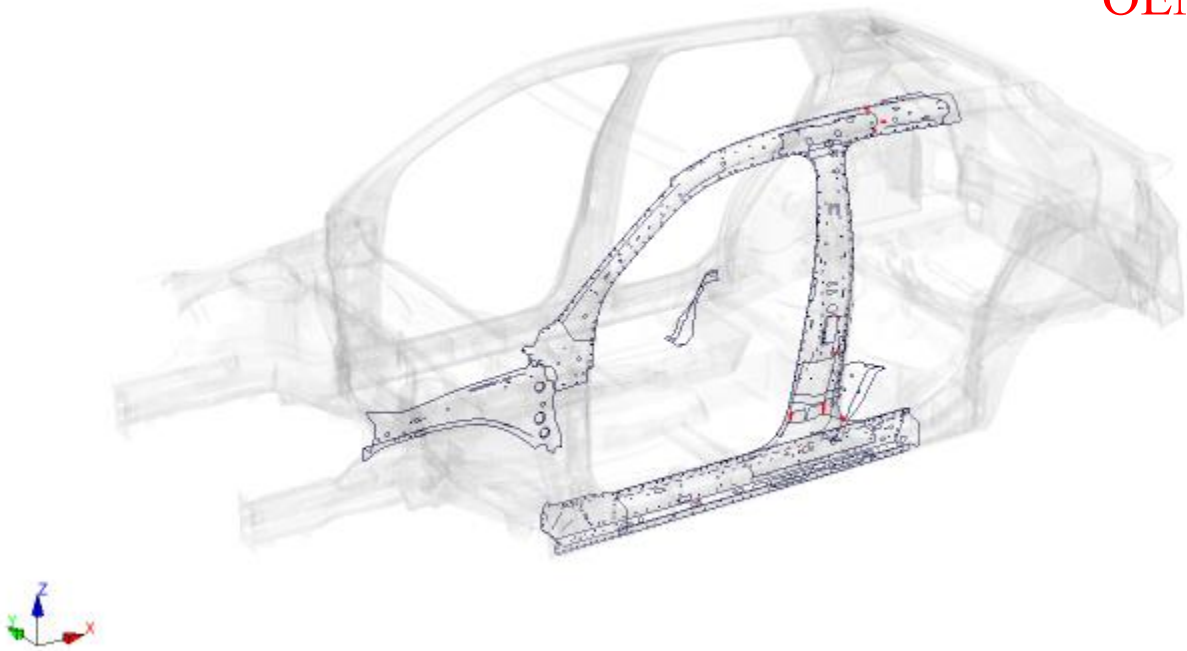


Figure 52: Static side intrusion after IIHS MDB Side Crash. eTCM vs OEM

OEM



eTCM

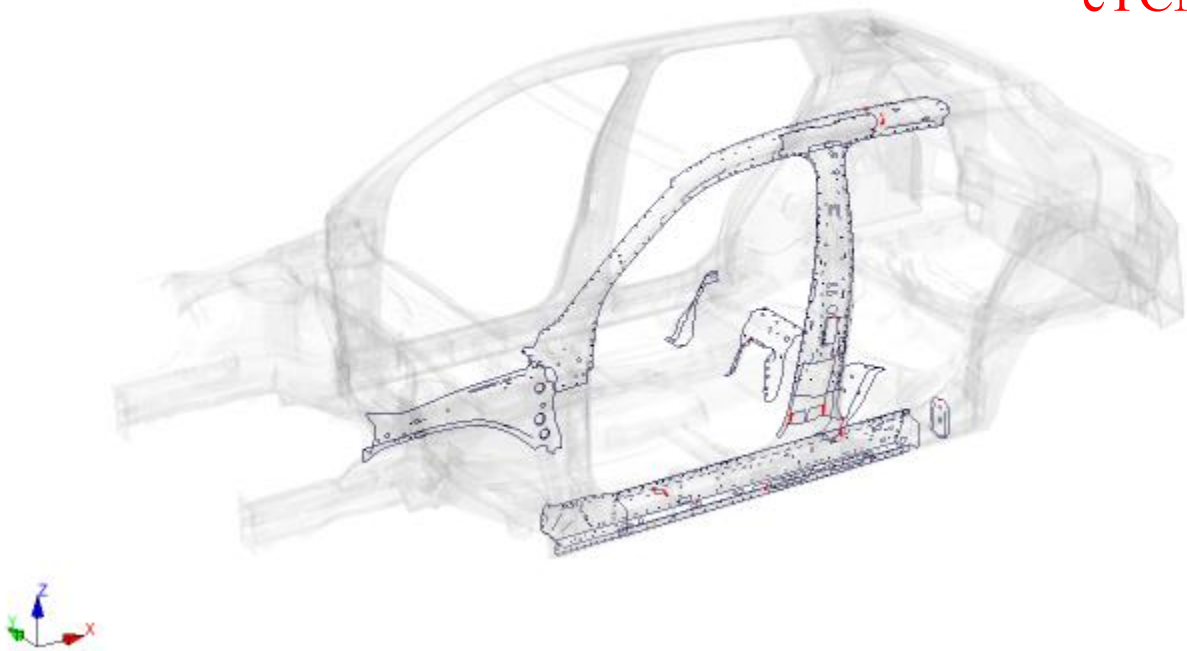


Figure 53: Failures in Body in White after IIHS MDB Side Crash. eTCM vs OEM

4.3 Front Crash

Another crash test simulation taken in account is the EuroNCAP ODB (Offset Deformable Barrier) equivalent to the IIHS moderate overlap frontal crash. The reference regulation is the one released by IIHS [42]. The offset barrier crash tests are conducted at 64.4 km/h and 40% overlap. The test vehicle is aligned with the deformable barrier such that the right edge of the barrier face is offset to the left of the vehicle centreline by 10% of the vehicle width (Fig. 54).

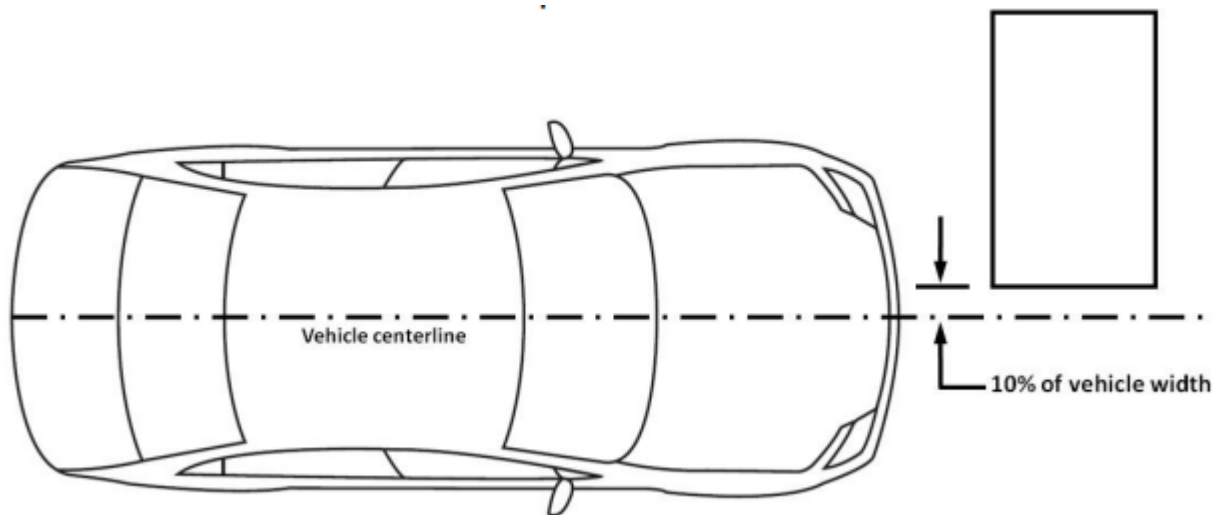
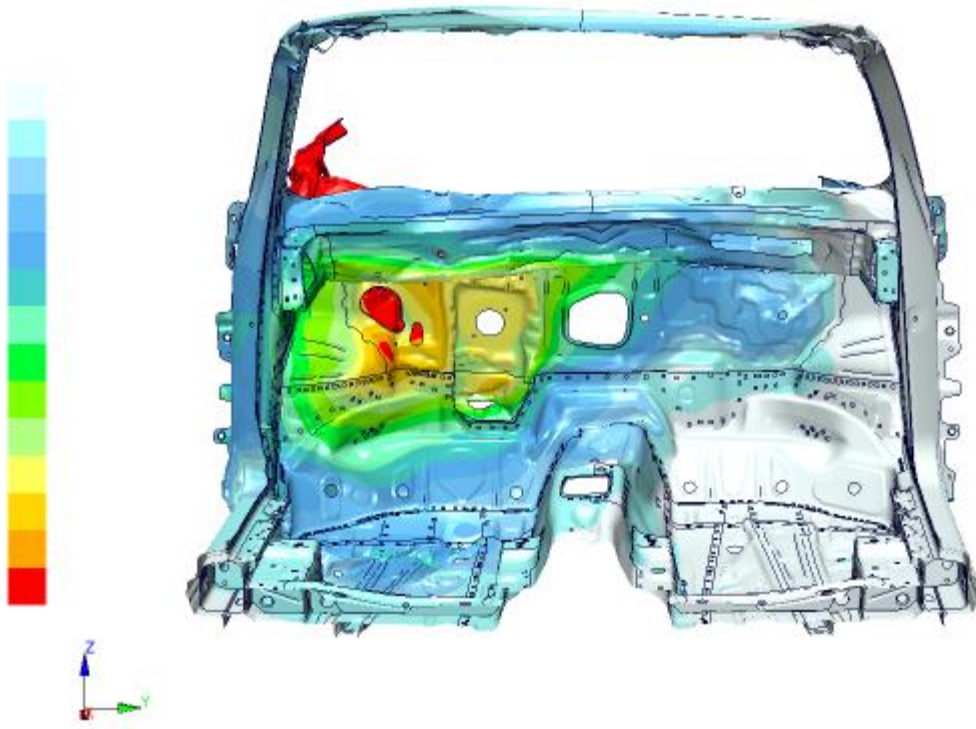


Figure 54: Vehicle overlap with deformable barrier [42]

The vehicle is accelerated by the propulsion system at an average of 0.3 g until it reaches the test speed and then is released from the propulsion system 25 cm before the barrier. The onboard braking system is activated 1.0 second after the vehicle is released from the propulsion system.

Also in this case the results of the simulations are very similar showing the same levels of intrusion and the same critical areas for failures (Fig. 55, 56).

OEM



eTCM

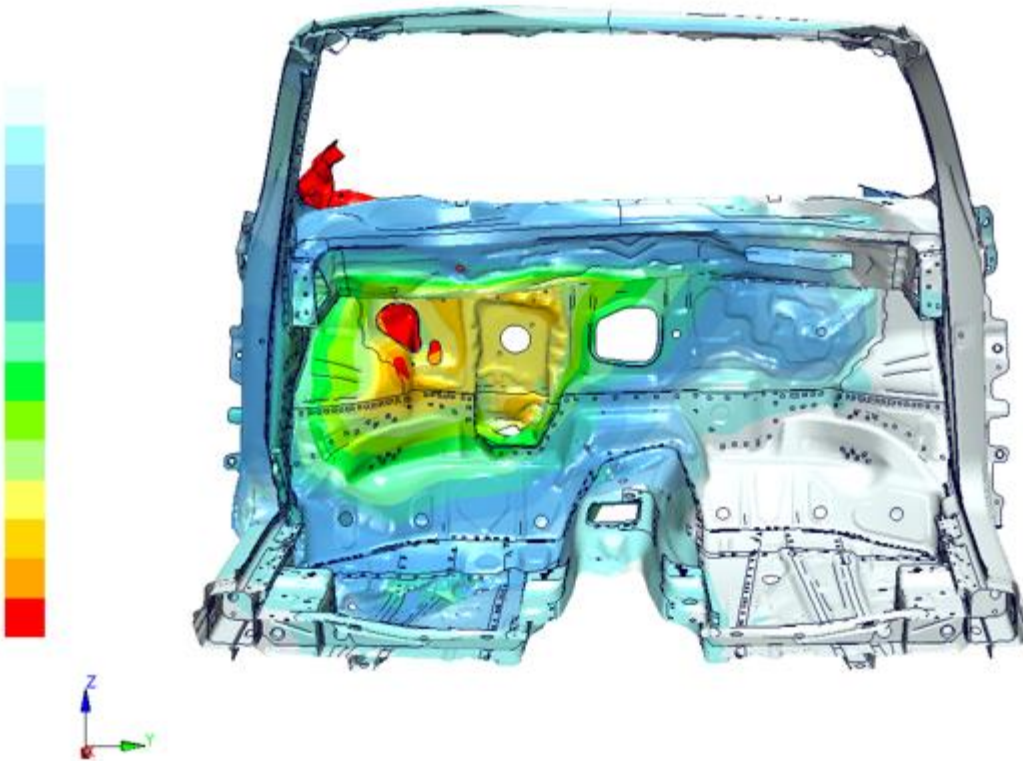
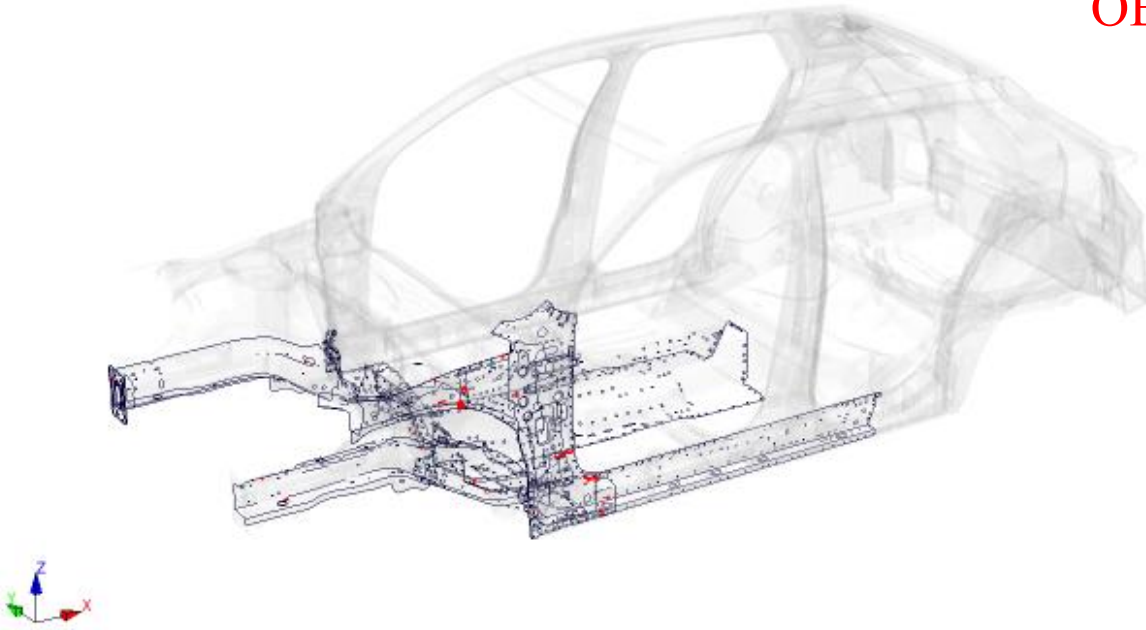


Figure 55: Static Intrusion after IIHS ODB Front Crash

OEM



eTCM

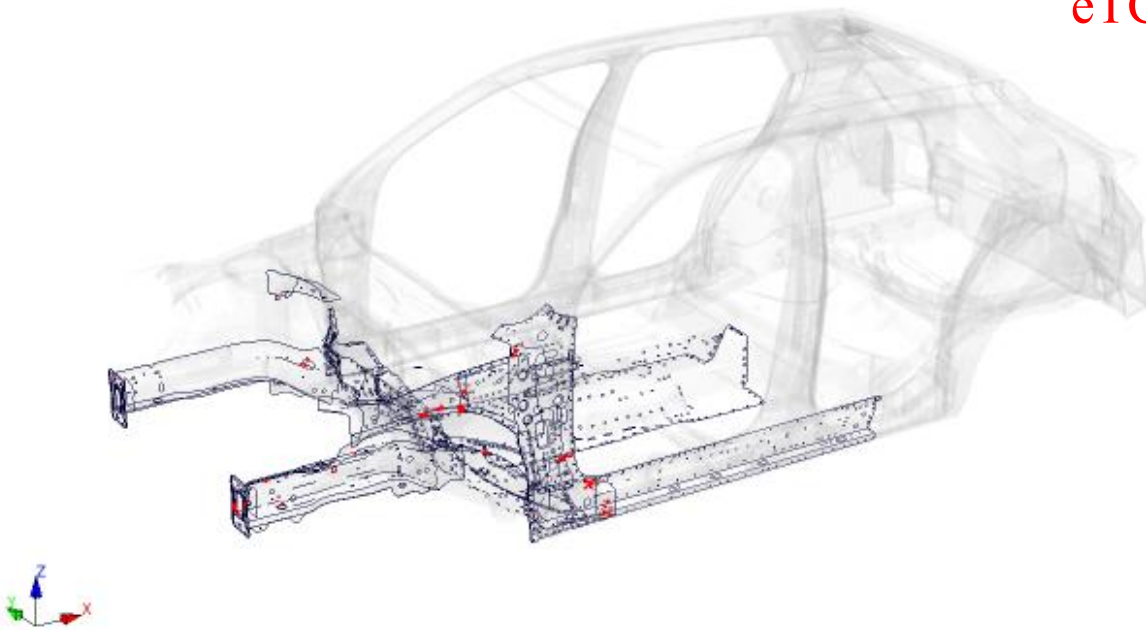


Figure 56: Failures in Body in White after IIHS ODB Front Crash

5. Conclusions

The models presented in this thesis successfully characterized the main classes of steel used in automotive industry. The first part of this work shown a versatile procedure to calibrate steels starting with a few experimental data, while the second part resulted in a new analytical model based on the Tailored Crash Model. Both models have been compared with a material database released by an OEM and used for crash simulations showing a comparable energy absorption. This means that the two strain-rate constitutive models can be directly applied to finite element simulations of component-level or full-vehicle impact models. These models can be a very cost-efficient support to design and development of vehicle crash structures since they provide a full characterization with no experimental tests needed.

The procedure developed for soft, HSLA, IF, BH and Dual Phase steels can be adapted to characterize also other types of steel and possibly any other metal with the enough data.

The enhanced Tailored Crash Model has been implemented in a Excel tool which can be used to obtain all the curves needed for a crash simulation only by choosing the desired Vickers Hardness. This has been possible thanks to the extrapolation of every parameter of the model with respect to Vickers Hardness values. Finite elements simulations showed a good correlation with the comparison model, but it presents some discrepancies around HV 400, this is caused by the weighting parameter fixed equal to 0.3 for every HV values. Probably also the extrapolation of the Swift hardening curve with the TCM model instead of real tensile test data played a role in the difference between the eTCM model and a material database based on experimental data. A further

improvement of the eTCM model could be achieved with a testing campaign to obtain a more accurate dependency of the parameters involved.

References

- [1] “International Organization of Motor Vehicle Manufacturers,” [Online]. Available: <http://www.oica.net>.
- [2] J. Hollomon, “Tensile deformations,” *Trans. Metall. Soc. AIME* 162, pp. 268-290, 1945.
- [3] P. Ludwik, *Elemente der technologischen Mechanik.*, Springer Verlag Berlin, 1909.
- [4] M. Swift, “Plastic instability under plane stress,” *J. Mech. Phys. Solid*, no. 1, pp. 1-18, 1952.
- [5] E. Voce, “The relationship between stress and strain for homogeneous deformation.,” *J. Int. Metals.*, no. 74, pp. 537-562, 1948.
- [6] J. Hockett and O. Sherby, “Large strain deformation of polycrystalline metals at low homologous temperatures.,” *J. Mech. Phys. Solid*, vol. 23, no. 2, pp. 113-120, 1975.
- [7] A. Gosh, “Tensile instability and necking in materials with strain hardening and strain-rate hardening.,” *Acta Met*, no. 25, pp. 1413-1424, 1977.
- [8] L. Kessler and J. Gerlach, “The impact of materials testing strategies on the determination and calibration of different FEM material models.,” in *IDDRG*, 2006.
- [9] L. Kaps, H. Lipowsky, M. Meywerk, H. Werner and S.-P. Scholz, “Auswerteverfahren zur Weiterverarbeitung von Versuchsdaten.,” VDEH working group intern communication, 1999.

- [10] G. Totten, L. Xie and K. Futanani, Modeling and simulation for material selection and, Marce Dekker, 2004.
- [11] C. Thome, G. Canova, U. Kocks, Christodoulou, N. and J. Jonas, "The relation between .macroscopic and microscopic strain hardening in FCC polycrystals.," *Acta Metall*, no. 32, pp. 1637-1653, 1984.
- [12] C. F. Lin and W. -S. Lee, "Comparative study of the impact response and microstructure of 304L stainless steel with and without pre-strain," *Metall. Mater. Trans. A*, no. 33A, pp. 2801-2810, 2002.
- [13] M. Yoshizawa and H. Ohsawa, "Evaluation of strain rate sensitivity in superplastic compressive deformation," *J. Mater. Process. Technol.*, no. 69, pp. 206-214, 1997.
- [14] M. F. Shi and D. J. Meuleman, "On certain aspects of strain rate sensitivity of sheet metals," *J. Mater. Eng. Perform*, no. 4-3, pp. 321-333, 1995.
- [15] I. Shindler, E. Hadasik and R. Kawalla, "Strain rate sensitivity in hot forming of steel- influence of microstructure, temperature and chemical composition," *Steel Res. Int*, no. 74-10, pp. 617-623, 2003.
- [16] W. F. Hosford, "Effect of Strain-Rate Exponents on Neck Shape.," *IDDRG*, pp. 95-99, 2000.
- [17] D. W. Wilson, "Strain rate sensitivity and effects of strain rate in sheet forming," *Met. Technol*, pp. 282-292, 1980.

- [18] A. K. Ghosh, "The influence of strain hardening and strain rate sensitivity of sheet metals.," *J. Eng. Mater. Technol.*, pp. 264-274, 1977.
- [19] S. P. Keeler and W. A. Backofen, "Plastic instability and fracture in sheet stretched over rigid punches," *ASM Trans. Quart.*, no. 56, pp. 25-48, 1964.
- [20] J. Hu, Z. Marciniak and J. Duncan, *Mechanics of Sheet Metal Forming*, Butterworth-Heinemann, 2002.
- [21] S. Storen and J. R. Rice, "Localized Necking in thin Sheets," *J. Mech. Phys. Solids*, vol. 23, pp. 421-441, 1975.
- [22] C. A. Coulomb, "Essai sur une application des regles de maximis et minimis quelques problemes de statique, relatifs a l'architecture.," in *Memoires de Mathematique de l'Academie Royale de Science*, Paris, 1776.
- [23] O. Mohr, *Abhandlungen aus dem Gebiete der Technischen*, Berlin: Ernst, 1914.
- [24] Y. Bai and T. Wierzbicki, "Application of extended Mohr-Coulomb criterion to ductile fracture," *International Journal of Fracture*, vol. 1, no. 161, pp. 1-20, 2010.
- [25] Y. Bao, Prediction of ductile crack formation in uncracked bodies, PhD thesis: Massachusetts Institute of Technology, 2003.
- [26] Y. Bao and T. Wierzbicki, "On the cut-off value of negative triaxiality for fracture," *Eng. Fract. Mech.*, no. 72, pp. 1049-1069, 2004.

- [27] T. Wierzbicki, Y. Bao, Y.-W. Lee and Y. Bai, "Calibration and evaluation of seven fracture models," *Int. J. Mech. Sci.*, no. 47, pp. 719-743, 2005b.
- [28] I. Barsoum and J. Faleskog, "Rupture mechanisms in combined tension and shear experiments," *Int. J. Solids. Struct.*, no. 44, pp. 1768-1786, 2007.
- [29] Y. Korkolis and S. Kiriakides, "Inflation and burst of anisotropic aluminum tubes for hydroforming applications," *Int. J. Plast.*, no. 24(3), pp. 509-543, 2008.
- [30] Y. Bai and T. Wierzbicki, "A new model of metal plasticity and fracture with pressure and lode dependence.," *Int J Plast*, vol. 24, no. 6, pp. 1071-1096, 2008.
- [31] T. Wierzbicki and L. Xue, *On the effect of the third invariant of stress deviator on ductile fracture*, Massachusetts Institute of Technology, Cambridge, MA: Impact and Crashworthiness Laboratory, 2005b.
- [32] "Autosteel," [Online]. Available: <https://www.autosteel.org/>.
- [33] "SEP1240: Testing and documentation guideline for the experimental determination of mechanical properties of steel sheets for CAE-calculations," VDEh Germany, 2006.
- [34] P. Larour, Strain rate sensitivity of automotive sheet steels: influence of plastic strain, strain rate, temperature, microstructure, bake hardening and pre-strain, Von der Fakultät für Georessourcen und Materialtechnik der Rheinisch -Westfälischen Technischen Hochschule Aachen, 2010.

- [35] A. Bardelcik, M. J. Worswick, S. Winkler and M. A. Wells, “A Strain Rate Sensitive Constitutive Model for Quenched Boron Steel with Tailored Properties,” *International Journal of Impact Engineering*, no. 50, pp. 49-61, 2012.
- [36] K. Pack and S. J. Marcadet, “Numerical failure analysis of three-point bending on martensitic hat assembly using advanced plasticity and fracture models for complex loading,” *International Journal of Solids and Structures*, no. 85-86, pp. 144-159, 2016.
- [37] C. Bao, L. Le Joncour and M. Francois, “A Closer Look at the Diffuse and Localised Necking of a Metallic Thin Sheet: Evolution of the Two Bands Pattern,” *Strain*, no. 52, pp. 244-260, 2016.
- [38] W. C. Emmens, *Formability*, SpringerBriefs in Applied Sciences and Technology, 2011.
- [39] L. ten Kortenaar, *Failure Characterization of Hot Formed Boron Steels with Tailored Mechanical Properties*, Waterloo, Ontario, Canada: University of Waterloo, 2016.
- [40] E. K. Tom, L. Greve, M. T. Andres, M. Medricky, A. Hatscher, T. Meinders and T. van den Boogaard, “Constitutive Modeling of Quench-Hardenable Boron Steel With Tailored Properties,” in *Forming Technology Forum*, Munchen, 2013.
- [41] Insurance Institute for Highway Safety, “Side Impact Protocol (Ver. X),” 2017.
- [42] Insurance Institute for Highway Safety, “Moderate Overlap Test Protocol (Ver. XVIII),” 2017.

[43] P. Surajit, G. Manikandan and K. V. Rahul, "Prediction of entire forming limit diagram from simple tensile material properties," *The Journal of Strain Analysis for Engineering Design*, pp. 386-394, 1 August 2013.

[44] A. Piskun, *Karosseriebautage*, Hamburg, 2017.

[45] W. Lohmar and A. Marangon, *Die Entwicklung der Karosserie des Audi Q2 – eine deutsch-italienische Geschichte. In: Piskun A. (eds) Karosseriebautage Hamburg 2017. Proceedings.*, 2017.